POLITECNICO
MILANO 1863

SCUOLA DI INGEGNERIA INDUSTRIALE
E DELL'INFORMAZIONE

Development of MELCOR v2.2 Input for the simulation of QUENCH-06 experiment

TESI DI LAUREA MAGISTRALE IN
NUCLEAR ENGINEERING - INGEGNERIA NUCLEARE

Author: **Matteo Garbarini**

Student ID: 945724
Advisor: Lelio Luzzi
Co-advisor: Fulvio Mascari, Fabrizio Gabrielli
Academic Year: 2021-22

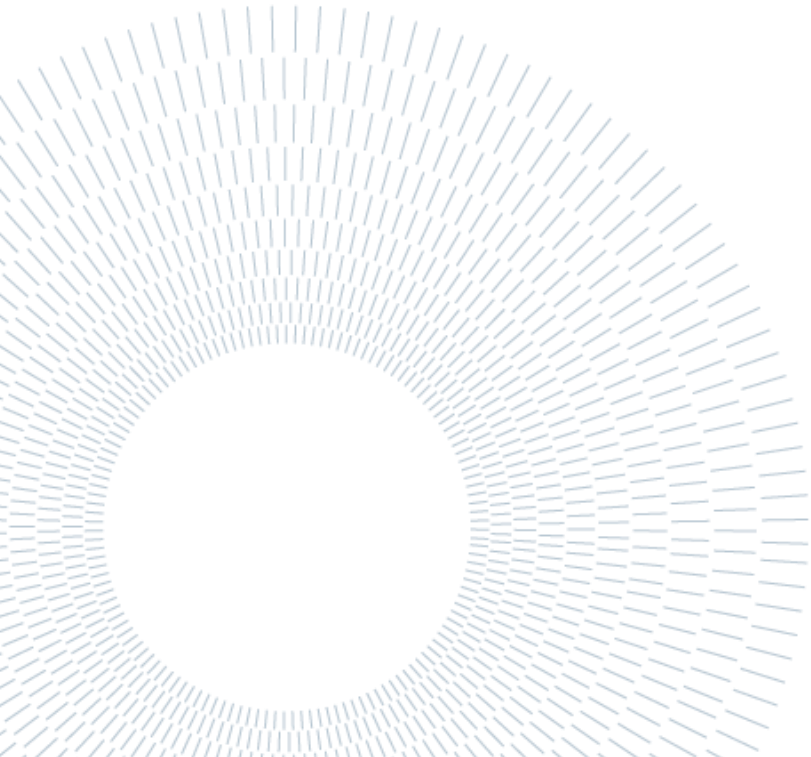

Abstract

Purpose of the current work is the development of the MELCOR v2.2 input of the QUENCH-06 test facility for the validation of Core Heat up and Degradation embedded models. Having as reference the past QUENCH analyses available on public technical literature and experimental data deployed by KIT, the author develops from scratch the input deck adopting several correlations and up-to-date features such to make it potentially the state of art MELCOR tool for the description of any QUENCH series experiment. Characteristics of QUENCH-06 MELCOR Input is a nodalization that allows for a fine representation of test active region, a precise definition of boundary conditions and ultimately a detailed thermal insulation system. The accuracy of the final configuration is qualitative and quantitative assessed by comparing some predicted Figures of Merit (such as hydrogen generation, maximum cladding temperature and corrosion profiles), selected on engineering judgement and on physical importance, against experimental measurements. In addition, application of the input is stretched to include in the calculations a sensitivity analysis to test the behavior of several Zircaloy-Steam oxidation correlations.

The results of *Reference* input is a good overall representation of the test phenomenologies. Until fast water preinjection, i.e., preoxidation phase and power ramping, predicted hydrogen production is well estimated, as the bundle temperatures and the corrosion profiles. However, current efforts are still not able to reduce an overestimated radial temperature gradient. Nonetheless, Fast Fourier Based Transform Method (FFTBM) analysis estimates a good accuracy of the input result at these stages. Between the two injections, the sudden partial re-evaporation of liquid water is hardly detected by the simulation, and therefore further studies are needed to address such phenomenon.

As concern the outcome of the sensitivity analysis, coupling *Cathcart-Pawel formulation* in low temperature regime and *Volchek* correlation when surface temperature becomes higher than 1900 K delivers results even more closer to the experimental trends than the reference calculation, and hence it is suggested to future users to adopt this description in oncoming simulations.

Key-words: deterministic, validation, MELCOR, hydrogen, zircaloy, oxidation.

Abstract in italiano

L'obiettivo del seguente lavoro di tesi è la creazione di un input dell'impianto QUENCH-06 per il codice MELCOR v2.2, nell'ottica di validarne i modelli di Riscaldamento del Nocciolo e della Degradazione. Partendo dalla raccolta dei dati sperimentali forniti dal KIT, e analizzando i precedenti lavori svolti su QUENCH-06, l'input viene sviluppato ex novo, adottando modelli, correlazioni e funzionalità aggiornate tali da renderlo potenzialmente il riferimento da adottare nel codice MELCOR per la simulazione di un qualsiasi esperimento della serie QUENCH. Le caratteristiche dell'input sono una nodalizzazione che permette una fine descrizione della regione attiva del test, un preciso settaggio delle condizioni al contorno e infine un dettagliato sistema di isolamento termico. L'accuratezza del modello viene valutata sia qualitativamente che quantitativamente attraverso il confronto di alcune Figure di Merito (quali produzione di idrogeno, massima temperatura di guaina, profilo di corrosione), selezionate sulla base di giudizio ingegneristico e importanza fisica, rispetto ai dati sperimentali. In aggiunta, l'applicazione dell'input viene estesa al fine di stabilire una analisi di sensitività atta a testare il comportamento dello strumento rispetto ad alcune correlazioni di ossidazione Zircaloy-Acqua.

Il modello *Reference* fornisce dei risultati che ben rappresentano le fenomenologie che si verificano in QUENCH-06. Nella fase di preossidazione e di riscaldamento, cioè fino all'iniezione veloce, la produzione cumulata di idrogeno, le temperature superficiali delle strutture e i profili di corrosione sono predetti in linea con le misure sperimentali. Sfortunatamente, le modifiche fin qui introdotte non sono riuscite a risolvere la sovrastima del gradiente di temperatura radiale. Ciononostante, l'analisi FFBTM della accuratezza quantitativa delle previsioni indica un buon risultato fino a questo stadio. Nella fase tra le due iniezioni, il modello non riesce a descrivere la veloce ri-evaporazione parziale dell'acqua, fenomeno per il quale sono previsti studi futuri al fine di riadattare e migliorare l'input.

L'analisi di sensitività invece sottolinea come l'adozione delle correlazioni di ossidazione di *Cathcart-Pawel* nel regime di bassa temperatura, e della *Volchek* per temperature superficiali maggiori di 1900 K producano risultati ancora più accurati

della formulazione di default, e pertanto ne è suggerita l'adozione ai futuri utilizzatori dell'input.

Parole chiave: deterministico, validazione, MELCOR, idrogeno, zircaloy, ossidazione.

Contents

1 Introduction

This thesis project is aimed to developing a QUENCH-06 computational input deck to be submitted to MELCOR v2.2 code as user independent validation exercise in the framework of Core Heat up and Degradation model qualification.

QUENCH are a series of test devoted to investigating the hydrogen generation in an uncovered Light Water Reactor (LWR) like core by zircaloy oxidation reaction. QUENCH-06 experiment has been adopted as OECD International Standard Problem No. 45 [1] for blind and open qualification of severe accident numerical tools.

Selected code for the validation campaign is MELCOR (*Methods for Estimation of Leakages and Consequences of Releases*). It is a computer code developed by Sandia National Laboratories for U.S. Nuclear Regulatory Commission that models the progression of severe accidents in LWR plants. MELCOR is capable of covering a broad spectrum of phenomena at different scales adopting a unified structure, composed of several packages devoted to the simulation of specific phenomenology.

The current work is organized at follows. Chapter 2 describes in detail the concept of nuclear safety and its implementation into Nuclear Power Plants (NPPs). In addition, it embodies an overview of the different plant states and accidental scenarios, with particular focus on Severe Accidents for framing the application domain of codes like MELCOR. It also contains description of such deterministic tools and the principles of code validation exploiting datasets from multiple test facilities. Chapter 3 presents QUENCH-06 goal, geometry, procedure, and experimental results. Main phenomenologies and physical aspects occurring during the test are specifically illustrated by means of Figures of Merit to establish basis for the comparison against code output. Chapter 4 delivers a comprehensive overview of the main MELCOR packages, with the relative calculation framework, and of the models of key importance for the design of QUENCH-06 input. QUENCH-06 Input is presented in Chapter 5 through a serial description of packages and parameters. Besides, additional input decks are established to perform a sensitivity analysis against several Zircaloy-Steam oxidation correlations. Results and remarks of the

principal simulation and of the sensitivity analysis are postponed in Chapter 6. Chapter 7 contains conclusions and hints for the future development of the current work.

Flowchart of thesis subject and structure is proposed in Figure 1.1.

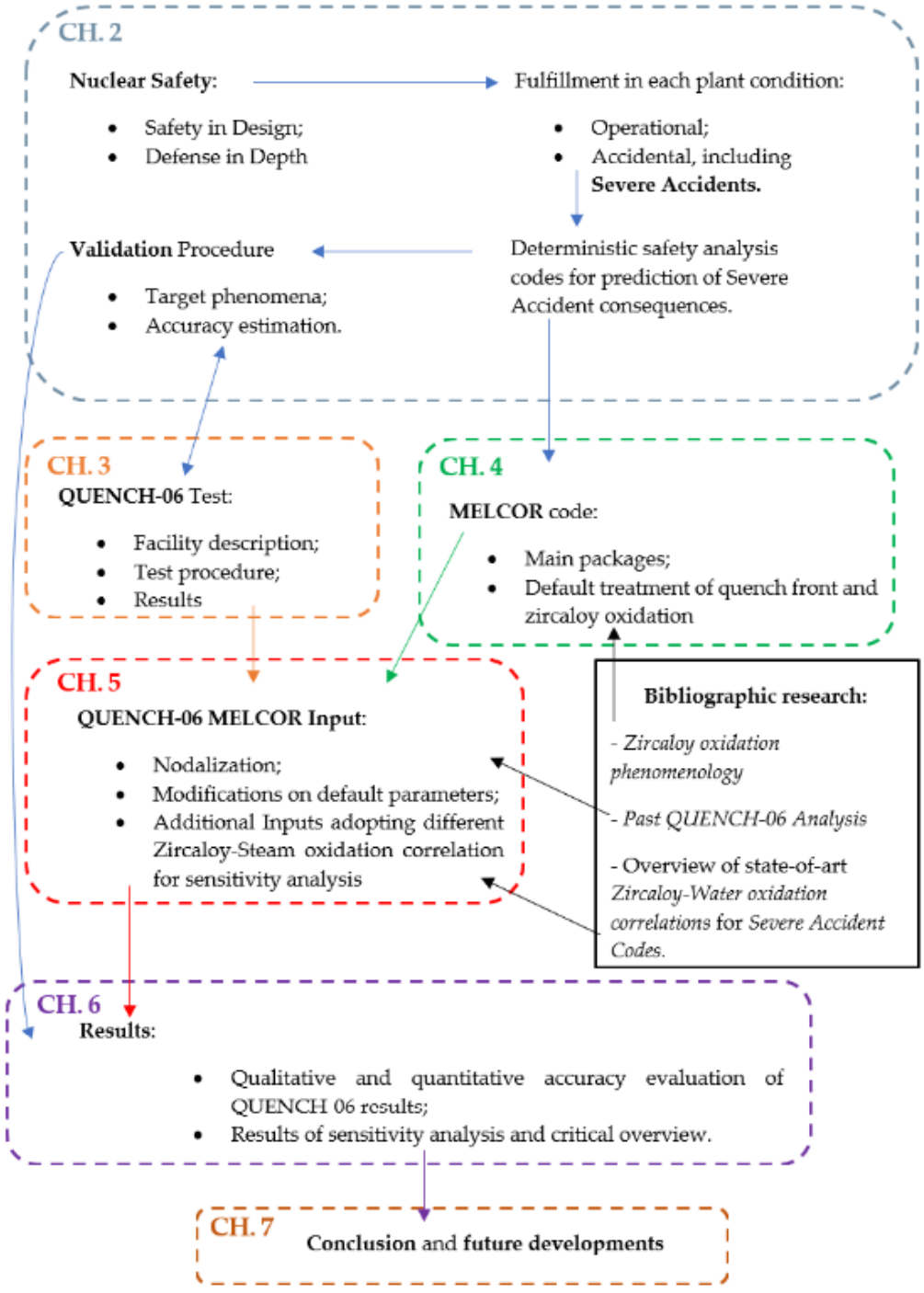

Figure 1.1: Thesis flow chart

Among the participants to the blind and open phase of the OECD International Standard Problem No. 45, several groups have adopted MELCOR code to build the computational input of QUENCH-06 facility. Nevertheless, the only detailed documentation accessible in the technical literature up to author knowledge about nodalization schemes is related to the work of Stanojevic and Leskovar [2] performed on MELCOR v1.8.5. Having as a reference the approach of Stanojevic et al., the author has developed from scratch the input deck , placing the focus on the active region of the facility, through the modification of boundary conditions, and the implementation of additional features and models available in MELCOR v2.2.

.

2 Nuclear Safety, Severe Accidents, Deterministic Analysis and Code Validation

From the dawn of nuclear energy industry, great efforts from analysts and organizations have been made to ensure that any deviation from operational states in nuclear facilities never results in significant enhancements of radiological risk and out-of-bounds dose uptakes for workers and public.

However, harsh lessons as *Three Mile Island* [1979] and later *Fukushima Daichi* [2011] accidents forced international community to strengthen the concept of nuclear safety through a re-assessment of reactor design, prevention-mitigation strategies, management procedures for severe accidents and emergency response.

IAEA Safety Standard has been developed to establish an international supported basis for ensuring the highest level of safety for people and environment. Its hierchical structure is composed of three levels, each one characterized by increasing detail. **Safety Fundamentals** and **Principles** document [3] sets goal and principles of safe exercise for nuclear installations. *General Safety Objective* declares that:

> ***safety*** *goal must be the protection of people and environment from harmful effects of ionizing radiation, without limiting the operation of facilities or the conduct of activities that give rise to such hazards.*

Following this statement, Principles list embodied the main technical canons for a safe nuclear operation, such as:

- yielding substantial benefit to people;
- optimizing the protection strategies and implementing the As Low as Reasonably Achievable strategy (ALARA);
- protection for current and future generations;

- enduring system monitoring and accident prevention;
- implementing Defense in Depth;
- Establishing arrangements for emergency preparedness and response.

An integrated and consistent set of **Requirements** is derived from the principles to ensure the practical application of safety concepts. *General Requirements* provide to the licensee a broad list of basic obligations embracing all life stages of nuclear facility. Their implementation is described more in detail by means of *Specific Requirements*, that are expressed in "shall" terms, meaning the measures must be taken to restore the appropriate level of safety if the application is not in line with the requirements [4]. At the lowest level of IAEA Safety Standards, a collection of **Safety Guides**, posed in "should" terms, deliver recommendations on how to comply with requirements [4] through a comprehensive overview of best practice in design and management of nuclear installations.
IAEA Safety Standard overview is presented in Figure 2.1.

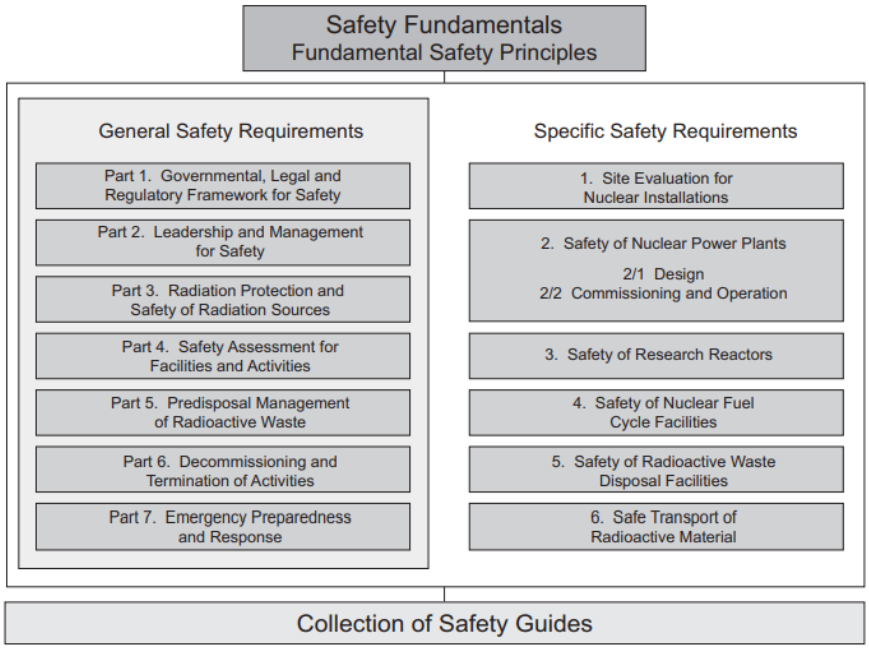

Figure 2.1: IAEA Safety Standard structure [4]

The adoption of IAEA Safety Standard does not concern exclusively reactors, but it covers, properly adjusted, research and medical centers, mining, milling and fuel reprocessing plants and waste disposals as well. As concerns NPP during exercise life, *Safety in Design* specific requirement and the principle of *Defense in Depth* are fundamental to guarantee that radiological risk is kept within limits (if its practical elimination is not feasible) regardless of the system state.

2.1. Safety in Design

The aim of implementing safety concepts [4] directly into the design is to create **intrinsic barriers against any possible failures through the improvement of single item's quality or the design of system made by multiple items**, and so delaying (or preventing) the need for turning on safety devoted features.

Once material and manufacturing processes are optimized, a hierarchical order of items in the nuclear island is needed to assign degrees of importance:

1. Items important to safety: Safety in Design is mandatory;
   1.1. Safety important items;
   1.2. Safety systems;
   1.3. Safety features for Design Extension Conditions;
2. Items not important to safety.

On this basis, several studies have to be performed to evaluate reliability, inter-dependencies and to calibrate parameters with design limits set by experience, engineering judgements and physical behavior. Moreover, verification procedures and highly specialized anti-aging maintenance actions should be carried on periodically of safety important components.

It is of the uttermost importance that a priori systematic approach is applied to label all Common Cause Failures (CCFs), Postulated Initiating Events (PIE) (event that leads to anticipated operational occurrences or accidental conditions) and external hazards that could trigger a potentially serious accidental state in the plant. Therefore, the design has to be robust also in prevention and easy to be rendered safe. Anyway, since it is not possible to exclude a priori the occurrence of such events that could deviate system operation, *reactor design is meant to withstand a wide category of plant state* [5], *while being constantly in line with Requirements*. Foreseen NPP states are shown in Table 2.1 [4]:

Normal Conditions		Accidental Conditions		
Normal Operation	Anticipated Operational Occurences	Design Basis Accidents	Design Extension Condition	
			Without core melting	With core melting

Table 2.1: Plant Envelope

2.1.1. Normal Operation (NO)

This category embodies phases as reactor start-up, first criticality approach and stationary power generation. Furthermore, any changes in power generation for load following, any shutdown (hot, cold, for refueling) and both condition-based and preventive maintenance are still considered as normal states.

NPP design is obviously required to safely perform during NOs, proving that:

- Any early release of radioactive material does not occur;
- No major unexpected fluctuation in reactivity takes place;
- Spent Nuclear Fuel (SNF) is handled as programmed.

2.1.2. Anticipated Operational Occurrences (AOO)

AOOs are more complex than the maneuvers carried out in NOs and are typically expected to arise once in a reactor lifetime. In view of appropriate design provisions, safety-important items should not be damaged by the consequences of this particular plant state. Examples of initiating events that could lead to AOOs are listed below in Table 2.2.

PIE	Examples
Increase, Decrease in Heat Removal	Valve malfunctioning, secondary pressure control malfunctioning, feedwater pump trip ...
Increase, Decrease in reactor coolant system flow rate or water inventory	malfunctioning in Chemical and Volume Control System (CVCS), Main Coolant Pump (MCP) trip, loss of off-site power
Reactivity and Power distribution anomalies	Boron dilution, wrong fuel assemblies shuffling ...
Release in radioactive material from subsystems	Minor leakages from radioactive waste wet storage, partial evaporation of SNF pool during wet storage …

Table 2.2: PIEs for AOOs [5]

Experts set as frequency of such states 10^{-2} events/year [5] .

2.1.3. Design Basis Accident (DBA)

DBAs class embraces all postulated accidental scenarios which consequences are considered for the design of safety features in order to respect design criteria using a conservative approach, assuring that the fraction of radiological inventory exiting the facility is within the prescribed limits. In Table 2.3 PIEs leading to DBAs ae depicted.

PIE	Examples
Increase, Decrease in Heat Removal	Steam line breaks, feedwater line breaks, MCP seizure …
Reactivity and Power distribution anomalies	Uncontrolled control rod withdrawal, control rod ejection ...
Increase in reactor coolant inventory	Inadvertent operation of emergency core cooling
Decrease in reactor coolant inventory	all Loss Of Coolant Accident (LOCA) spectrum, leaks of primary coolant into secondary loop
Release in radioactive material from subsystems	large breaks in SNF management systems, fuel overheating in transit or storage

Table 2.3: PIEs for DBA [5]

Frequency of occurrence of these scenarios is set very low, equal to 10^{-2} – 10^{-6} events/year [5].

Engineering good practice suggests adding a safety margin in design to render safety important items more robust and gain extra confidence in their resilience during DBAs.

However, it has been proposed to include in the design of the component new safety features and enhanced accident management procedures for those scenarios considered more severe than DBAs. Hence, the definition of Design Extension Condition was developed.

2.1.4. Design Extension Condition (DEC)

DEC states are beyond the DBA and they are considered in the design process of the plant in accordance with best estimate methodology. NPP in this condition is affected by multiple failures, either caused by equipment malfunctions or human errors, loss of redundancy of active Engineering Barriers System (EBS) and most likely grid connection. The release of radioactive material occurring during DECs must be kept within acceptable limits. Identification of PIEs that could bring system to DECs is of main importance, and it should be performed through best estimate analysis.

DECs are further sub-categorized in two sections, as shown in Table 2.4.

Accident	PIEs	Subtypes		Design Goal
DEC	Station Black-out (SBO), Anticipated Transient without SCRAM (ATWS), LOCAs without safety injections (high pressure or low pressure), multiple steam generators ruptures, loss of heat sink, extensive loss of cooling in fuel pools, loss of core cooling in Residual Heat Removal (RHR) mode, uncontrolled boron dilution	**DEC-A**	Core not degraded	**Prevention**
		DEC-B	core degradation	**Mitigation**

Table 2.4: DECs overview [5]

Given the frame severity, control of DECs is expected to be achieved primarily by features directly implemented in the design as supplementary upgrades [5], in order to succeed in accident prevention/mitigation without relying only on accident management measures. The main constrain set for these scenarios is **that containment must keep its integrity**, preventing radioactive release (or mitigating it following ALARA principle) and allowing for a prompt and time-limited action to bring back the plant in controlled state.

DEC-A and DEC-B may share the root causes, but they differ on how the entire system reacts and suppresses the evolutions of events. For instance, if no proper

mitigation strategies are performed, DEC-A evolves into DEC-B, that is characterized by serious phenomena (both involving in-vessel and ex-vessel regions) like hydrogen detonation, steam explosion or basement melt after core-concrete interaction.

DEC-A expected frequency is stated to be between 10^{-4} and 10^{-6} events per year [5]. Core melting is even more remote, with an expected occurrence rate lower than 10^{-6} y^{-1} [5].

A brief description of what could be the progression for a DEC scenario is given in Section 2.1.4.1.

2.1.4.1. DEC Phenomenology

DECs-B are also called **Severe Accidents** (SA) [6].

These scenarios are initiated **in-vessel** when the decrease of water level in the core region following the PIEs leaves the top part of fuel rods uncovered. Steam coming from the on-going evaporation of the underneath pool is not able to remove efficiently power from fuel elements, which start to overheat. When the surface temperature is sufficiently high, oxidation reaction on zircaloy is triggered, releasing additional energy, and causing the onset of hydrogen generation. Exothermal energy produced by sheaths, summed to the decay heat of fission products generates a temperature escalation which establishes positive feedback on oxidation reactions. The time scale of in-vessel phenomena is largely dependent on safety countermeasures, reactor design and on the kind of PIE itself. Once it is no more possible to rely on convention (forced or natural) or on some heat sink, low melting point structures in the core starts degrading, modifying core layout, and diverting flow motion. With the evolution of the accident, cladding and fuel pellets begin to melt, relocating in the lower head (*slumping*) and speeding up the hydrogen generation by offering higher available area to oxidants. Fission products stored in the fuel matrix are now carried by the steam across the primary circuit. The molten pool (fuel, cladding, supporting structures, plates, grids, barrel) fills the lower plenum, and start thinning the lower head. With the piercing of the lower head, Reactor Pressure Vessel (RPV) is failed. The progression in the **ex-vessel** region depends greatly on the state of the cavity and the containment. Corium may interact with a wet cavity (FCI, Fuel Coolant Interaction), causing a sudden evaporation, pressure build-up and the risk of steam explosion. Decay heat is considered to play a marginal role in evolution of the scenario outside RPV. If safety measures are not effective in stopping the transient (mainly through debris fragmentation in pool filling the cavity) molten material will start the ablation of the concrete (MCCI, Molten Core Concrete Interaction), whose kinetics may span from several hours up

to days. In this timeframe, non-condensable gasses spread and contaminate the containment facilities. Hydrogen generation is still going on, increasing the flammability and detonation risk (mitigated through recombiners or igniters). Largest activity in this early phase is due to iodine isotopes in the aerosol. The composition of the source term (i.e., the radiological inventory exiting the containment) is strongly depending on the failure time of the concrete walls, and the failure mode as well. Main phenomena taking place during SAs are depicted in Figure 2.2 below.

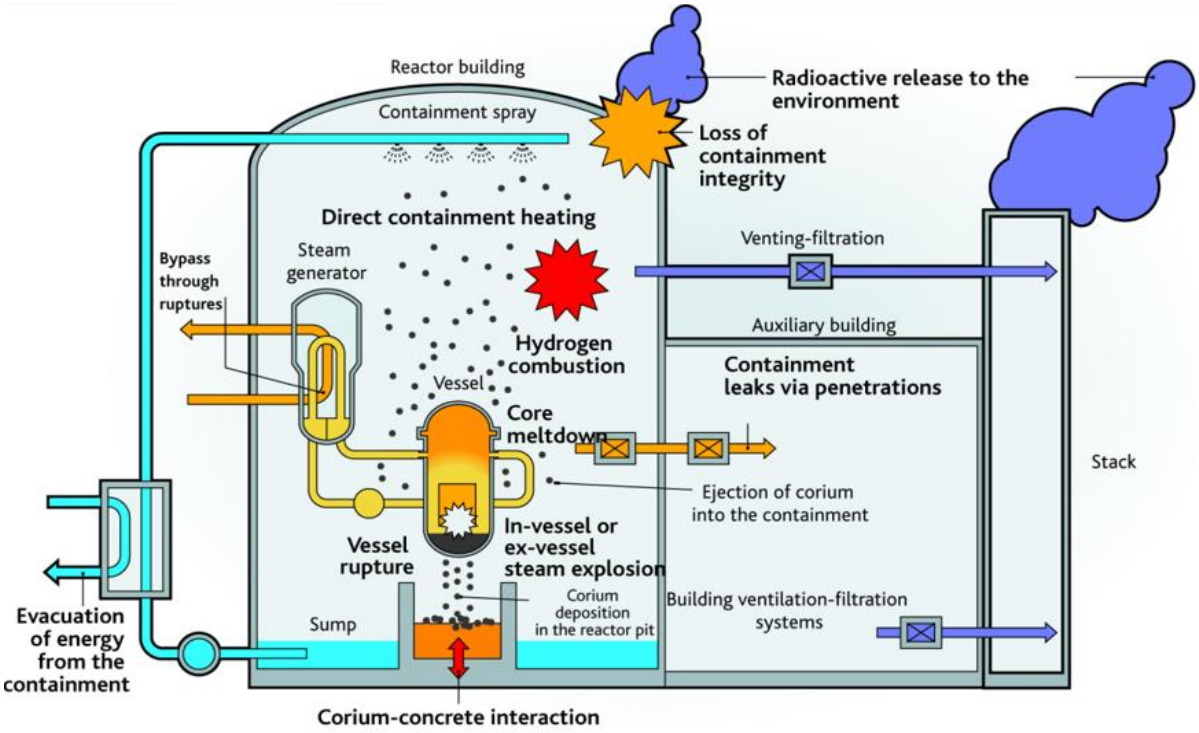

Figure 2.2 SA events [7]

To further lowering the risk of radiological hazards in any plant condition, Safety in Design must be coupled with the principle of Defense in Depth.

2.2. Defense in Depth

The strategy defined by **Defense in Depth** (DID) [3] aims to combine an effective management system, adequate site selection, good design choices, engineering and inherent features and protection tools to reduce the occurrence or delay the escalation of accidental conditions in NPP.

Principle at the basis of DID is the triad **Prevent, Protect and Mitigate**.

DID introduces a series of *levels* [5], each one concerning the main aspect of safety and barriers to be implemented to effectively face any plant state:

- **Level 1**: purpose of first level is to reduce, through Safety in Design, the frequency of every event that could deviate system from NOs. This level requires that the licensee evaluates conservatively and adequately the location, construction, manufacturing, and maintenance of NPP in compliance with Safety Requirements.
- **Level 2**: DID second layer is devoted to the correct installment of EBS and monitoring instruments to avoid the onset of AOOs. Example of barriers belonging to L2 are:
    - Sensors and surveillance;
    - reactor trip system;
    - onsite emergency power supply units.

  In the case plant enters the AOO state, those features shall by themself manage the scenario, reducing the number of challenges to DID Level 3.
- **Level 3:** for the third level it is assumed that, although very unlikely, PIE evolves, and system state becomes formally accidental. Its main goal is to mitigate the condition averting the core melt. Hence, Level 3 embodies all engineered (active, passive) and inherent barriers that should sustain the DBA and DEC-A. Main safety system regarding this level are:
    - Ventilation system;
    - Backup cooling system;
    - CVCS;
    - RHR;
    - Emergency Cooling Control System (ECCS).
- **Level 4:** this level deals with the control and the mitigation of a SA with core partial or total melting. DID L4 barriers must cope with Safety in Design features to cool down corium, limit the radiological release and maintain the containment integrity. To this level formally belongs tools as:
    - Catalytic hydrogen recombiners;
    - In-containment ventilation system;
    - Igniters.

  In addition, it is planned the implementation of a Technical Support Centre to assure help to the onsite management staff.
- **Level 5**: the essential mean of the outer level of DID is to formalize the procedures for onsite and offsite Emergency Preparedness and Response, evacuation of public and evaluation of the source term. Since Level 5 is reached only if measures of Level 4 are hollowed, its goal is to mitigate the contamination on other structures of nuclear island and on the inhabited centers as well.

DID levels shall be [5] independent as far as practical in order to reduce the likelihood of concurrent or consequential failures . Moreover, it is mandatory that all **those features devoted to handle the DEC conditions must not be shared among different systems nor rely on the correct functioning of other safety important items.** The practical application of DID is performed through the installation of multiple, redundant, independent, physically separated, and consecutive barriers covering from the fuel elements up to containment and staff offices.

DID concept is represented in Figure 2.3.

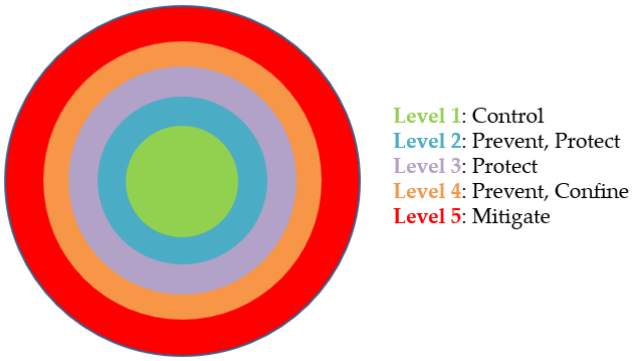

Figure 2.3: DID outline

It should be added the establishment of an accidental scenarios like DBA and DEC-A may occur in a NPP that was operating in NOs, especially when it is suddenly affected by a *cliff-edge effect* (a small perturbation with rapid and abrupt impacts). Hence, elasticity and promptness in response are requirements safety barriers and DID features must always fulfill.

The concurrent application of Safety in Design and DID is thought to be sufficient to secure a *practical elimination* [5] of most concerning conditions NPP could suffer.

Once the main safety features are identified and two previous safety concepts are adopted, it is necessary to conduct an assessment on the entire system to evaluate if the items and barriers are in compliance with safety standards. Such studies have to be carried out through probabilistic and deterministic analyses.

Probabilistic Safety Analysis is a comprehensive, structured approach to identifying failure scenarios, frequency of departure from NOs constituting a conceptual and mathematical tool for deriving numerical estimates of risk [8]. Furthermore, it is devoted to check if the design is balanced [4]. It means that, in the unfortunate case PIEs or cliff-edge effect occurs, the uncertainties on the

consequences are not disproportioned and the escalation of the plant state is easy to predict.

The description of Deterministic Analysis is presented in the following section.

2.3. Deterministic Analysis

The objective of deterministic safety analysis [9] for NPPs is to analytically characterize physical phenomena taking place in a selected NPP during a transient progression, for instance DBA and DECs. It gives the necessary information to judge if selected safety requirements are fulfilled by NPP in transient conditions. Study of this highly challenging states is fundamental to guarantee that safety functions perform with the requested confidence and that the structures, systems, and components are capable and sufficiently effective to keep negligible the releases of radioactive material.

Deterministic approach analytically solves systems of equations in **mean quantities** in a single accidental sequence [6], without giving in output any info about their variance nor spread. Key figures of merit considered during such analyses are hydrogen generation, fission product release or cladding temperature.

A well carried out deterministic study characterizes the entirety of plant states and their evolution through the representation of multi-physics phenomena (thermal-hydraulics, structure behaviors, chemical interactions, neutronics). Particular focus must be devoted to the identification of the widest set of PIEs, CCFs and human errors that could enhance the radiological risk during special NPP operation (such as refueling, maintenance or shutdown), in which departures from NOs are more likely to occur. Deterministic safety analysis can be performed adopting different levels of conservatism in the selection of boundary conditions, system components availability and computer codes. In Table 2.5 the main approaches are presented.

Option	Computer Code Type	Assumptions about systems availability	Initial boundary conditions
1. Conservative	Conservative	Conservative	Conservative
2. Combined	Best Estimate	Conservative	Conservative
3. Best Estimate + uncertainty	Best Estimate	Conservative	Best Estimate, partially unfavorable
4. Realistic*	Best Estimate	Best Estimate	Best Estimate

Table 2.5: DSA approaches [9]

Option 1 has been widely used in the past, when the computational resources were limited and complete description of phenomena was not fully developed. Currently, as state of the art for DSA is chosen the *Option 3* [9], in which best estimate codes are selected to simulate a conservative scenario with slightly pessimistic boundary conditions. The last option (asterisked because usually not coupled with any uncertainty evaluation) is often used to represent AOO and DEC.

It is important to specify that a deterministic analysis is considered to be conservative if a priori it accounts for partial/total failures of safety barriers, or if the boundary conditions are set worse than expected.

Acceptability of the DSA results is judged on the basis of quantitative acceptance criteria [9]:

1. Safety criteria: expressed in terms of activity release and/or dose to workers, usually set by law or by regulatory recommendations.
2. Design criteria: deployed by regulators in form of physical variables to guarantee the integrity of barriers as fuel matrix, cladding, RPV, primary circuit, containment.
3. Calculation criteria: analyst must be confident that adopted codes deliver highly accurate results. Moreover, any simplifying assumption and correlation must be justified and supported.

The third point is fulfilled by comparing benchmark code results with experimental data. Regarding the particular case of SA, several tests have been established for characterizing the main phenomenologies (e.g., core degradation, hydrogen generation, core cavity interaction), but there are still uncertainties due to physical processes that are not still investigated in prototypical geometries with prototypical materials.
Therefore, further comments need to be added on the computational code performing Deterministic Safety Analysis in SA frames. The dissertation follows in the next section.

2.3.1. Computer Codes for SA Safety Analysis in LWR-PHWR

SA in NPPs encompass a broad range of interacting, both in-vessel and ex-vessel events sequences [6] as:

- Single-phase, two-phase thermal-hydraulic behavior in primary circuit and in containment;

- core degradation through cladding oxidation, melt formation, relocation of material towards lower head, melt pool behavior, corium-concrete interactions;
- release of fission products into primary circuit and containment;
- hydrogen accumulation and direct containment heating …

Given the complex analytical description of those phenomena, SA devoted codes have been developed by different institutions following the accident of TMI [1979]. These types of software share an integral approach, in which sets of (usually) 1-D equations regarding the specific aspect are stored in dedicated modules. Then, single package output constitutes the boundary conditions for other units. Being this architecture, SA codes will never be as accurate as 2-D or 3-D tools in a particular description, but they assure acceptable results on large scale (spatial and temporal from initiating event up to the release) with smaller computational effort.

It needs to be added that, even if they were created for SA accident in water reactors, nowadays these codes are being updated for application on sodium, lead and LBE technologies and on spent nuclear fuel pools too.

The main SA codes are:

1. **AC²** [6] : it is a tri-module software in which ATHLET package is used for modelling thermal-hydraulics, structure mechanics and in vessel phenomena, ATHLET-CD for SA phenomena in primary circuit, and COCOSYS unit covers the containment/building response during the accidental sequence. It is developed by GRS.
2. **ASTEC** [6] : ASTEC consists in a cluster of modules, each one handling single features (ICARE for core degradation, CESAR for 2-D thermal-hydraulics). ASTEC is used for reactor safety, source term evaluation and SA management assessment. It is developed by IRSN.
3. MAAP [6] : it models the response of LWR and CANDU power plants during SA. It describes simultaneously thermal hydraulics and fission products behavior within the primary circuit and the containment. MAAP is also used for investigating accident managements strategies, emergency planning and equipment qualification. It is developed by EPRI.
4. **MELCOR** [6] : it is a fully integrated, engineering level computer code developed by Sandia National Laboratory for the USNRC to model the progression of SA in NPPs. Its application covers the majority of phenomena in LWR through a wide set of physical models grouped in packages. A more detailed description of MELCOR is postponed at Chapter 4.

5. **RELAP5/SCDAPSIM** [6] : the last version of this code, deployed by ISS (NC, USA) coupled the robust thermal hydraulics of RELAP with detailed fuel behavior models integrated in SCDAPSIM. It also embeds an uncertainty analysis tool and a detailed 3-D reactor kinetics.
6. **SOCRAT** [6]: of IBRAE, Atomproekt, Rosenergoatom (RUS), its use is intended for VVER NPP under SA. The main three modules are SVECHA, RATEG and HEFEST, developed coupling mechanistic and correlation-based models about thermal-hydraulics, physical-chemical phenomena, fission products release and radioactive transport.

Although deterministic integral codes are key tool for the analyses of SA**, there are still non-negligible uncertainties** in the implemented models ([6] reports for instance debris relocation dynamics and core slumping as the main sources) that require further investigations. For this reason, uncertainty, and sensitivity analyses for the correct tailoring some parameters to the case study should become common practices.

IAEA suggests that a verification-validation campaign should be conducted on the numerical tools performing safety analyses.

2.3.2. Code Verification

IAEA Requirement 18 [9] defines mandatory that code developers conduct processes of model and system code **verification** to qualify model mathematical framework and software architecture [10]. Verification should be done through reviews and de-bugging.

2.3.3. Code Validation

The procedure of code **validation** [9] is performed to assess the accuracy of the results in respect of an experimental dataset provided by experimental facilities properly scaled simulating the prototypical behavior of the reference reactor.

Since this phase is of central importance, it is usually carried out in two separate steps: the former in which it is the developer himself to check the results, while the latter is independently conducted by the user.
Code verification and in-factory validation are usually grouped into a macro-category, called "*Core Internal Development*". The code, before being distributed to the users community to withstand the second step, is called *"Qualified Frozen Code"*. The user validation is often labelled as *"Code Independent Qualification"* and it is targeted on the evaluation of the accuracy of the tool, i.e., estimation of the error in comparison between the code results and the provided dataset [10].

As far as concerns the test selected for validation, it is usually too costly, or practically impossible, to perform trials in nuclear facilities at full scale, especially in SA conditions, and for this reason assessment databases [10] are developed from different kinds of experiments [9], as:

- Basic Test: very simple, governed by phenomena which analytical solution is well known. They are used **to check** if the basis physics and **correlations** in codes are well predicted.
- Separate Effect Test: they could be either scaled or preferably full-scale experiment devoted to collect data on the single phenomenon or combined effects, but all localized in a single component. As concerns Separate Test Effects, particular attention should be given on **settings significantly boundary conditions**, the most representative of real nuclear plant.
- Integral Effect Test: they are usually performed in small-scale facilities in which it is possible to represent all the relevant physical processes and the interactions between the components. These tests should be characterized by the adoption of prototypical materials, fluids, and boundary conditions; test facility should **be** properly **scaled**, avoiding distortion effects on dominant physical phenomena.
- Nuclear Power Plant Level Test in Transient: these are actual maneuvers conducted during commissioning phase of the NPP.

It is important to highlight that it is usually recommended that validation matrix for a single code adopts **data** coming **from different experiments identifying several target phenomenologies** (i.e., one devoted to thermal-hydraulic, other focused more on oxidation or structure mechanics…) in the independent validation frame. Validation of the code against facility at different scales is suggested for assessing overall code capability and the accuracy of most models implemented.

In conclusion, for each model, single code users' groups comparisons and international code-to-code reviews in technical meetings are key features for establishing an additional validation campaign and an uncertainty assessment as well.

An example of scaled, separate effect test which has been largely exploited for code validation in respect of hydrogen generation and Zircaloy oxidation is QUENCH-06, performed ad KIT (Karlsruhe) on December 13, 2000.
Test description will be object of Chapter 3.

3 QUENCH-06 Experiment

QUENCH [11] is a series of **multi purposes**, **scaled down, separate effect tests** conducted at the *Karlsruhe Institut fur Technologie (KIT)* in Germany devoted to the simulation of the termination of an accidental sequence in a LWR core through the injection of steam and water.

The main goals of the experiments are:

- Evaluation of the hydrogen build-up in a heated bundle representative of hot, uncovered core;
- Description of Zircaloy cladding oxidation, cracking, and failure prior to reflooding;
- Understanding core evolution when suddenly cooled down by low pressure water (**quenching**) to suppress the initial degradation that may take place.

The outcome of these experiments provides an extensive and reliable dataset for the validation of SA codes, especially as concerns mechanistic models for zircaloy oxidation, the main process through which hydrogen is produced. It has been proven that, when cladding temperature are high enough (i.e., characteristic of a system in DBA) some effects on the sheaths, such as crack surface oxidation and steam starvation conditions (description of these phenomena is postponed in Section 4.4.1, Section 5.4.7), alter corrosion rate in a way that currently implemented correlations in SA tools suffers to catch. Furthermore, QUENCH results are of remarkable importance for the design of passive autocatalytic recombiners, the assessment of the ignition condition of the mixture steam-H_2 and, more generally, for the determination of correct safety margins.

As concern QUENCH-06, it has been used as OECD International Standard Problem n°45 for blind and open calculation of SA codes.

3.1. Test Facility

The QUENCH-06 facility [11] is composed of a test bundle, electric power supply units, steam-water loop, argon tanks, hydrogen detection devices, temperature, pressure, mass flow rate sensors and in conclusion process control instruments.

Pressure and Instrumentation Diagram (P&ID) is represented in Figure 3.1.

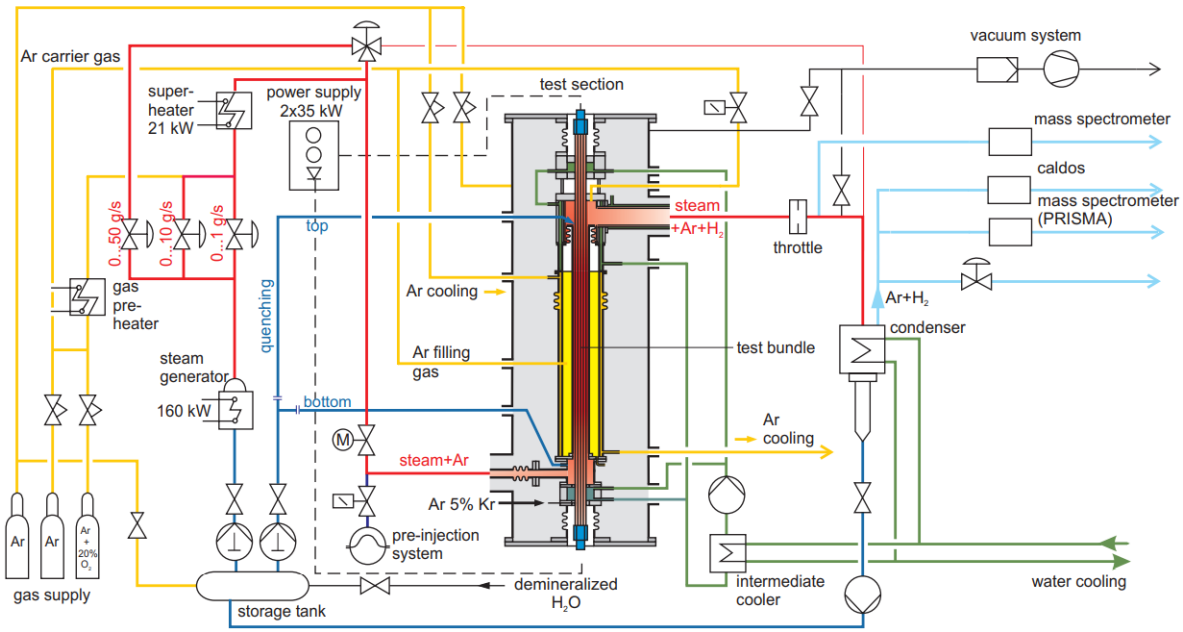

Figure 3.1: QUENCH-06 facility [11]

Square latticed **Test bundle** consists of an unheated central rod, 20 Fuel Rod Simulators (FRS) distributed along two concentric rings, and four solid zircaloy corner rods. Rod cladding is made of Zircaloy-4 (typical of PWR). Internal pressure of the gap is set 2.2 bar (slightly larger than the pressure of the flowing mixture) and filled with Krypton (5%) and Argon (95%). Krypton acts as a tracer for the cladding failure detection. Uranium dioxide is simulated through the adoption of hollowed ZrO_2 pellets (present both in FRS and in the unheated central rod). In the center of the FRS, it is present a tungsten heater wire connected to power supply units by two electrodes at each end of the rod, made of molybdenum and copper. In order to guarantee high insulation in correspondence of the electrodes, identifying in this way the tungsten section as the active part of the bundle, their surface has been coated with a thin layer of ZrO_2. The four corner positions are occupied by solid zircaloy rods (one of these can be withdrawn freely during the test), placed above zircaloy instrumentation tubes. All rods have a fix upper head; hence they are allowed to expand downward during the heat-up phase. The bundle is held in

position by five different grids distributed at various altitudes (lowest one in Inconel, the others made of zircaloy).

Overview of FRS and unheated central rod is shown in Figure 3.2.

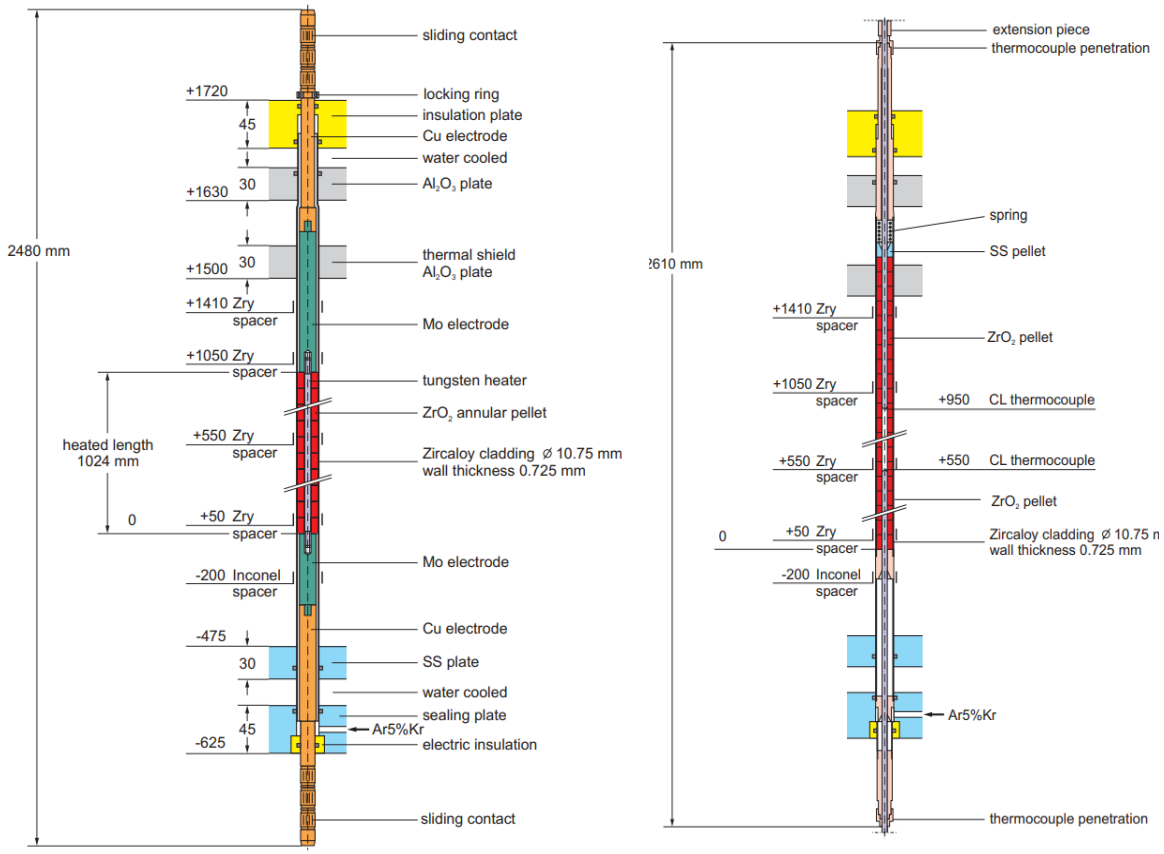

(a) Heated Fuel Rod (b) Unheated Fuel Rod

Figure 3.2 Rod layout [11]

Two power generation units of 35 kW of gross capacity each are connected to the two rings of rods (#1 grouping 8 inner rods, #2 for the remaining 12) through out-of-bundle wires. It is important to specify that the actual value of supplied power into the system is not what will be represented in Section 3.4 and so on., but **it must be reduced accounting for an external resistance R** (for cables resistivity, sliding contact) **about 0.5 mΩ/ring.**

The cooling chamber is limited in the lower part by a sealing plate made of stainless steel and plastic inlays for electrical insulation. In the upper section, system is capped by heat-protection Al_2O_3 shield placed below a plastic plate.

Thermal multi-layer insulation system surrounds the bundle in radial direction. The inner stratum consists of a thin cylindrical slab of zircaloy (addressed as

Shroud), which conducts heat generated by FRSs towards a ZrO_2 fiber sponge and a double-walled cooling jacket made of stainless steel. The annulus between the inner cooling jacket and the outer one is cooled down by a stationary flow rate of argon (elevation between -300 mm to 1300 mm) and subcooled water above. Between the heated zone top point (i.e., upper end of tungsten wire, at reference height of 1.024 m) and 1.3 m altitude zirconia fiber is substituted by a volume entirely filled by argon, whose motion is negligible making conduction and radiation the only energy transfer paths. In this cavity it is also placed an expansion compensator (a stainless-steel spring which elongation is function of the differential strain between the bundle and the insulating system] [12]. Above 1.3 m zircaloy shroud and stagnant argon meatus are not more present and the fluid crossing the bundle is radially bounded by water-cooled inner cooling jacket. The outer cooling jacket is surrounded by an external containment filled with argon at atmospheric pressure.

In Figure 3.3 it is presented both axial and structure of the test bundle facility, and the thermal dissipator system.

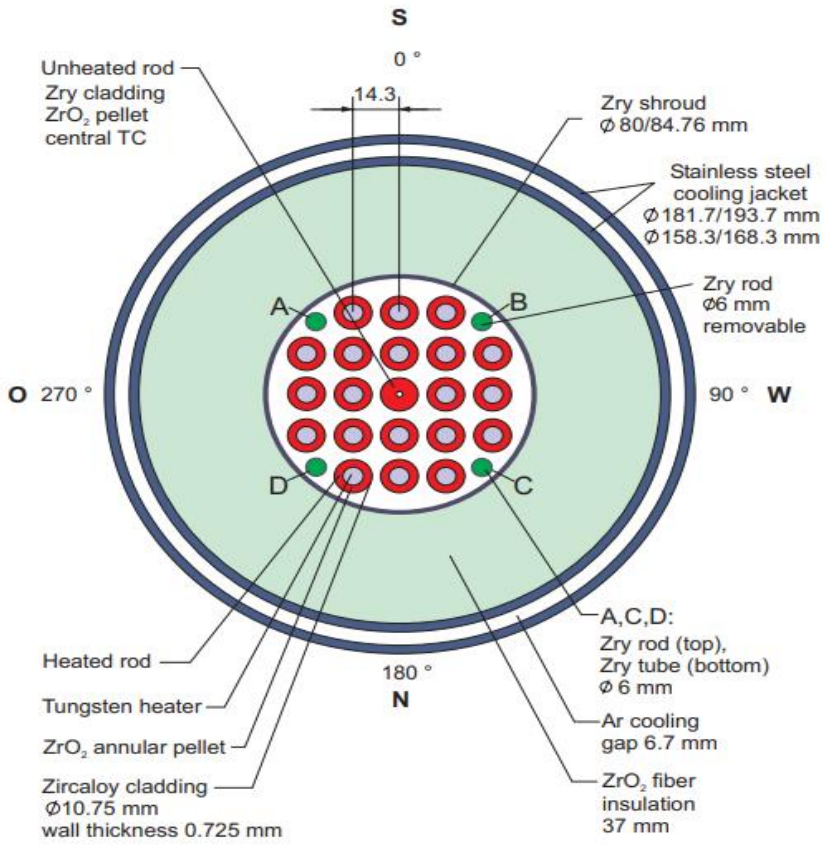

Figure 3.3 Test bundle radial view [11]

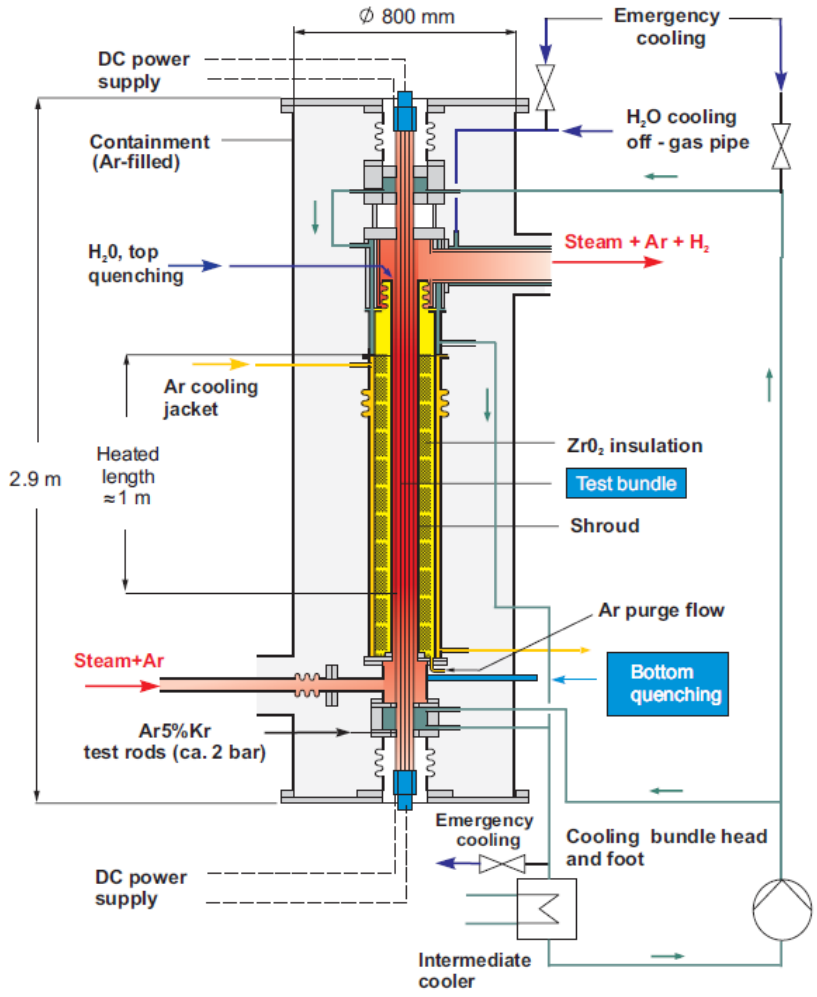

Figure 3.4 Bundel axial view [11]

Flowing mixture composed by superheated steam and argon enters the bundle through the inlet pipe placed at -0.412 m (bottom region) [12], with the pressure being around 2 bar and it moves upward removing heat and carrying hydrogen. In order to get a more uniform flow distribution along the vertical direction, a diffuser (hollowed tube) is placed in the inlet plenum, where the two flowing species come together. Argon-steam mixture, and the hydrogen if present, exits from the test section through an off-gas pipe (cooled by water in counterflow) that directs the flow through the first hydrogen measurement device (Mass Spectrometer GAM-300). Then, the non-condensable portion of the flow rate is separated from the steam in the condenser; and the argon, which now acts as main H_2 carrier, is sent to the hydrogen detectors, namely CALDOS and PRISMA mass spectrometer. Then, water flow is pumped, overheated again, mixed with argon source (from pressurized tanks) and sent back into the bundle.

A junction in the pipes linking the facility with gas supply tanks may divert argon flow to the upper head of the bundle, allowing for the further investigation of any accidental progression in a system partially cooled from above.

Piping circuit is equipped with a **superheater bypass** that allows the water to be pumped directly into the bundle. This option is exploited at the starting point of the quenching phase. In addition, inlet section is connected with the **fast pre-injection system** too, consisting in a pressurized water tank and a valve which opening is ruled by control room. Fast pre-injection items have been added to shorten the time for filling the pipes and lower plenum. In Figure 3.5 water circuit components are presented.

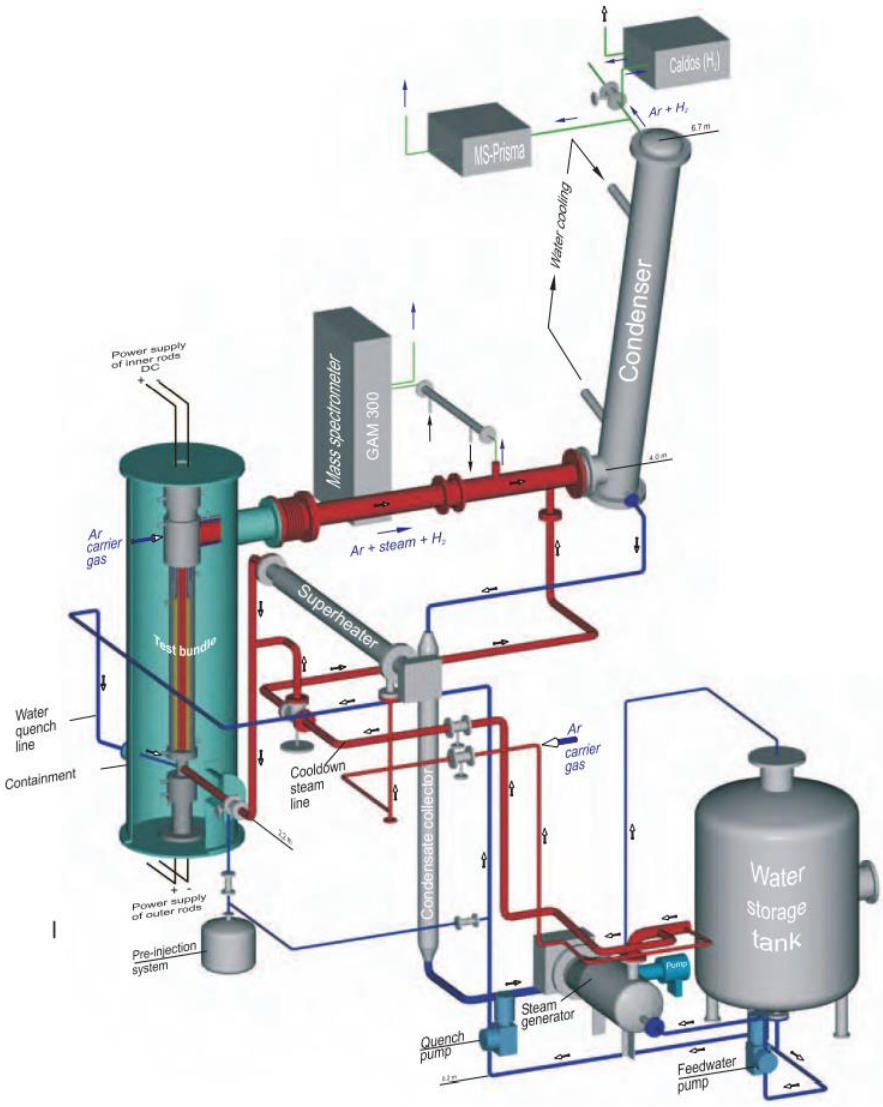

Figure 3.5 Thermal cycle [11]

For the sake of completeness, a more detailed view of inlet-outlet pipes [12] and plena are presented in the figures below.

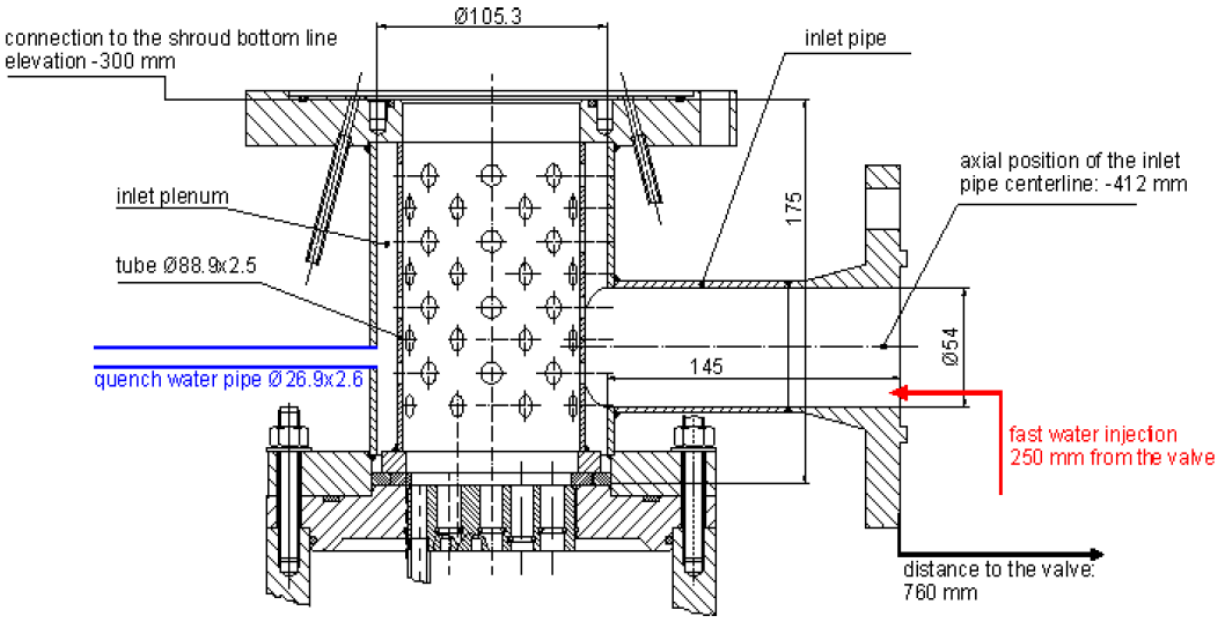

Figure 3.6 Lower plenum [12]

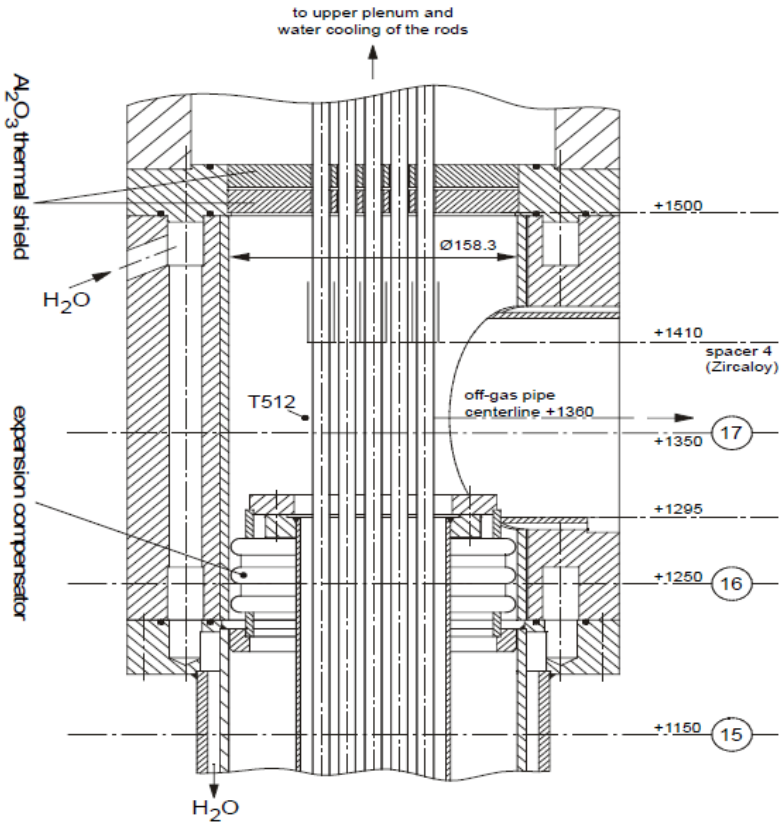

Figure 3.7 Upper plenum [12]

Facility geometries and main material properties are listed in the next tables.

Bundle Design		
Bundle	PWR, 21 rods	
Number of heated rods	20	
Number of unheated rods	1	
Pitch	14.3 mm	
Cladding	FRS	Length 2203 mm, Ø 9.4 mm/10.75 mm, Zircaloy-4
	Unheated	Length 2278 mm, Ø 9.4 mm/10.75 mm , Zircaloy-4
Heater material	Tungsten [W], length 1024 mm (EL 0 mm to 1024 mm), Ø 6mm	
Electrodes	Copper [Cu]	lower electrode: length 390 mm upper electrode: 190 mm Ø 8.6mm
	Molybdenum [Mo]	lower electrode: length 300 mm upper electrode: 576 mm Ø 8.6 mm
ZrO_2 Pellet Stack	FRS	Length 1024 mm (El 0 to 1024mm), Ø 6mm/9.15 mm Coating: Ø 8.6 mm, 9.15 mm
	Unheated rod	Length 1554 mm (EL 0 to 1554 mm), Ø 2.5 mm/ 9.15 mm
Grid spacers	Inconel 718	Thickness 38 mm, Position -200 mm
	Zircaloy-4	Thickness 42 mm, Position 50, 550, 1050, 1410 mm
Gap	Argon (95%), Krypton (5%), Pressure 2.2 bar), Ø 9.15 mm/9.3 mm	

Table 3.1: Bundle geometry [11]

Thermal Insulator		
Shroud	Zircaloy-4, Length: 1600 mm (EL-300 mm to 1300 mm) Ø80 mm/84.76 mm	
Insulating ZrO_2 sponge	ZrO_2 fiber, Length 1324 mm (EL -300 mm to 1024 mm) Ø84.76 mm/158.3 mm	
Insulating argon	Pressure 2 bar, Length 266 mm (EL 1024 mm to 1300 mm) Ø84.76 mm/158.3 mm	
Cooling Jacket	SS-1.4541 EL -300 mm to 1500 mm	Inner Ø158.3 mm/168.3 mm
		Outer Ø181.7 mm/193.7 mm
Annulus between cooling jackets	Quasi-stationary Argon at 2 bar, EL -300 mm to 1024 mm	
	Liquid water at 300K. EL 1300 mm to 1500 mm	

Table 3.2 Thermal Insulator geometry [11]

3.2. Hydrogen measurement devices

Three different instruments are devoted to the hydrogen detection, located between the bundle outlet section and the main pump.

GAM-300 mass spectrometer is connected to the off-gas pipe through a throttle and a bypass section. Given its position, it is the first device to be crossed, and it is assumed to measure in real time hydrogen concentration. Low detection limit is stated to be 10 ppm [11]. GAM is calibrated before the onset of measurements with stationary flows of both a well-characterized Argon-H_2 mixture, and steam. In the bundle outlet pipe GAM-300 sampling tube is inserted, with multiple holes at different depths for allowing a uniform pick up from the mixture. This pipe crosses a heat exchanger in order to avoid steam condensation before the mass spectrometer. The instrument evaluates online the content of several gas, including Kr from any potential clad flaw.

Mass spectrometer **PRISMA** and **CALDOS** devices are located downstream the condenser, measuring with 30 s of delay in respect of the mixture exiting time from the bundle. PRISMA working principle is the same of the GAM, except that it does not deal with humid samples.

CALDOS system [11] instead is based on the different heat conductivities of different gases. It is calibrated ahead of test start with a standard mixture of argon and hydrogen. For the correct functioning, residual humidity of the mixture has to be suppressed through a new condensation step. It is devoted just on the quantification of hydrogen concentration.

Evaluation of the hydrogen flow rate [11] is performed by referring the H_2 concentration to the known argon mass flow rate, according to (3.1)

$$\dot{m}_{H2} = \frac{MM_{H2}}{MM_{Ar}} \frac{C_{H2}}{C_{Ar}} \dot{m}_{Ar} \tag{3.1}$$

with MM being the molar mass, and C the concentrations in vol-%. Once hydrogen flow rate is evaluated at each sampling time, the cumulative hydrogen production is calculated through a simple time integration.

3.3. Test instrument and data acquisition

Sheathed thermocouples [11] are located at 17 different bundle heights between -250 mm and 1350 mm, facing the four azimuthal orientations. In the lower region (i.e., up to 550 mm) NiCr/Ni thermocouples (Ø 1 mm) are placed on both rods cladding and shroud outer surface. W-5Re/W-26Re THCs, with HfO_2 insulation and a duplex shield of tantalum/zircaloy are adopted in the upper zone, whereas conditions are more severe.

Each device has its own designation: TCR for the unheated rod, TFS for fuel simulator, TSH for shroud, TCI and TCO for inner and outer cooling jacket temperature respectively. Particular mention should be given to the THC inserted in the zircaloy instrumentation tubes (under the four zircaloy corner rods), denominated as TIT + corner rod code (A to D). In conclusion, TFS2/1 (wielded to inner FRS at -250 mm) have the top head bent into the channel to measure accurately the inlet temperature of the flowing mixture. Uncertainty in the reported values is given in [11] equal to +-50 K.

Inlet and outlet pipes are equipped with pressure and mass flow sensors.

In the bypass section connecting main pump and inlet section a volumetric flow rate (FM104) device measures the quench flow entering the bundle.

Data processing multichannel (#200) analyzer records at a maximum frequency of 25 Hz per channel. However, the acquisition rate is kept to 1 Hz up to power

ramping, when it is increased up to 5 Hz for allowing a finer collection during quenching.

Location of THCs are represented in Figure 3.8.

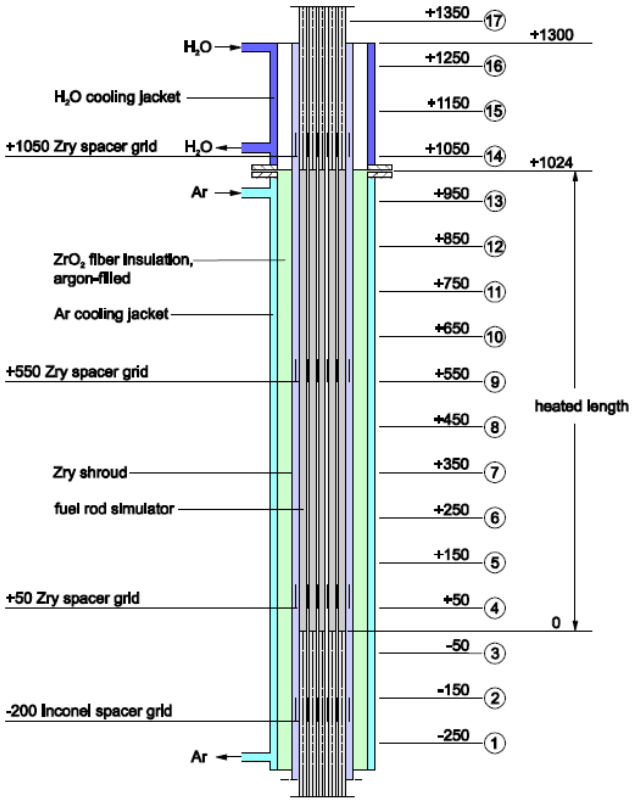

Figure 3.8: Thermocouples [11]

3.4. Test procedure

QUENCH-06 test is subdivided in four consecutive phases, each one characterized by different boundary conditions and phenomenology.

3.4.1. Preparation and preoxidation

The bundle, which is initially at room temperature, is heated up through a stepwise increase in power supply until it reaches a uniform temperature of 873 K, while it is crossed from the bottom by a mixture of 3 g/s of steam and 3 g/s of Argon at 640 K. This **Preparation** phase spans on 7200 s and it is aimed to load thermal masses ahead of the experiment reference starting point. Instrumentation devices are currently not recording.

Once the stabilization period is ended, data acquisition is turned on (**t = 0 s**), power supply is increased from 4kW to 11kW as long as the TFS devices report a cladding

temperature of around 1473 K at the endpoint of the active region. In this first transient, flowing mixture is not changed (still being 3 g/s of steam and 3 g/s of argon).

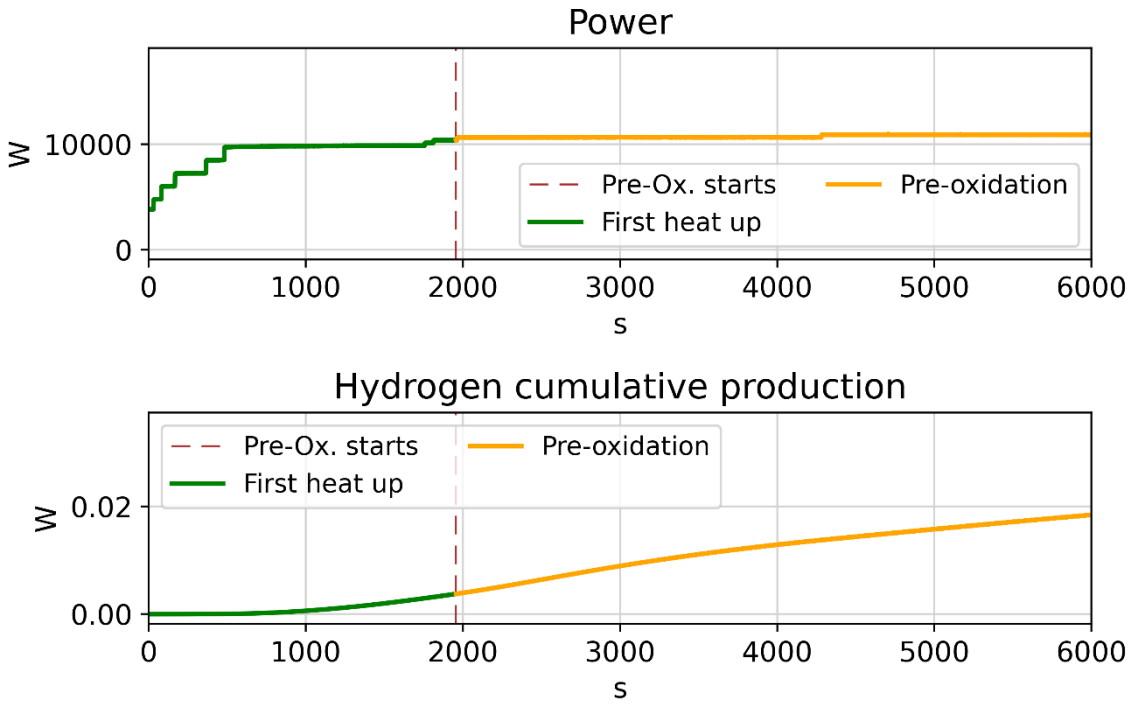

Figure 3.9: Preoxidation phase

In the timeframe shown in Figure 3.9, GAM-300 and the detection devices reveal the presence of hydrogen in the exiting flow, meaning the on-set of zircaloy oxidation. When the above-mentioned temperature is met (**t = 1955 s**), power is set stationary for 4000 s. This key stage is the **Preoxidation**, in which bundle temperature is constant and the hydrogen generation is parabolic in time ($\approx t^{0.5}$) due to the oxidation reaction kinetics of cladding zircaloy in isotherm condition. It is worth noticing that content on the hydrogen production given by the lower plenum stainless steel structures is almost negligible.

Such stage should represent the **early transient in a DBA**, not yet evolved in DEC, in which the core is uncovered, still producing decay heat but safety features are still capable of removing the power, causing no significant increase in structure temperature.

Preoxidation provide remarkable insights for assessing the safety features implemented into the design of the zircaloy cladding.

3.4.2. Power ramping

At the end of preoxidation period**, power is rapidly increased** (from **t = 6000s** to **t = 7179 s**) up to 18 kW at a rate of 6 W/s, causing a steep growth of hydrogen production. System thermal inertia causes an average temperature increment of around 0.3 K/s (on TIT-A/13 measurements basis). Steam and argon mixture injected in the lower plenum of the bundle are still acting as a coolant and hydrogen carriers. The mixture inlet bulk temperature has not been varied.

During this transient, corner rod B is withdrawn from the system and submitted to the metallographic analysis to evaluate the mass of consumed zircaloy and the oxide layer thickness at different altitudes.

This stage is characterized by some failure of the thermocouples at various point due to large thermal excursion or detachment from supporting structure (for instance TFS4/11, TCR13, TSH14/270 …). At the final instants of this phase, GAM-300 detects krypton traces in the mixture, meaning at least a cladding failure. Moreover, P406 sensor output (pressure signal, placed between zircaloy shroud and inner cooling jacket) shows an increase in the pressure across the insulation system, only relatable to shroud failure, probably after ballooning [11].

Power ramping phase, affected by very unfavorable conditions such as strong temperature gradient, poor heat transfer coefficient between cladding and coolant and a strong content of oxidation should resemble a scenario in which the **prototypical system has lost the major heat sink**. It is worth to specify that the **major power source in the final moments of this phase is given by the exothermal oxidation reaction on the zircaloy**, as result of the positive feedback arising from the inability of convection to remove power from the structures. This content is estimated to be greater than the 18 kW inserted through power generating units.

Ending time of the stage is set accordingly to the fulfillment of **quenching condition** [11]**,** that is the following:

- A minimum of three TFSs should have exceed 1973 K
- TCRC 13 (placed at the centerline of the unheated rod, at an elevation of 950 mm) should have measured at least 1873 K.

Given the condition, power ramping is stopped at **t = 7179.5 s**.

Stage outline is proposed in Figure 3.10.

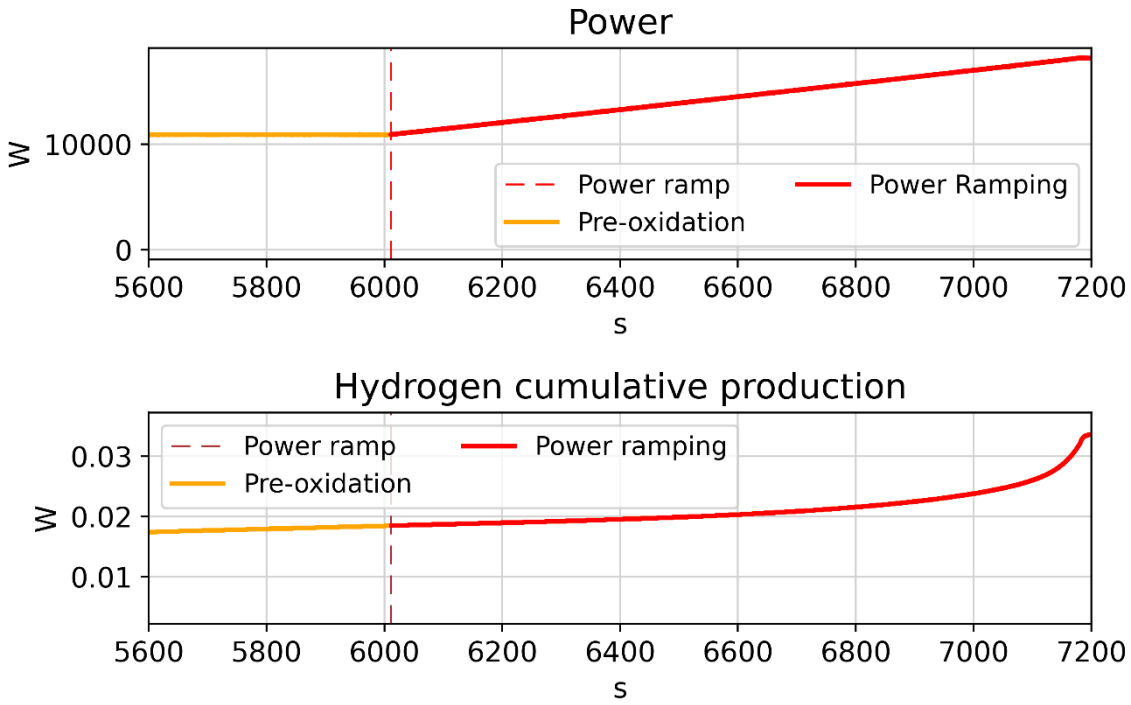

Figure 3.10: Power ramping phase

3.4.3. Quenching

At t = 7179.5 s fast preinjection valve is opened, allowing 4 l of subcooled water at 6 bar and 370 K for pre-filling inlet pipes and the bundle from the bottom. This first quench phase is terminated at **t = 7184.5 s**. In the meanwhile, steam flow rate is turned off, and the argon flow of 3 g/s is switched to bundle head, at an elevation of approx. 1500 mm.

Power is reduced from 18 kW quite sharply to 4 kW within 16 s. This value is maintained for the whole duration of main quench phase to represent a system in which the only energy source is the decay heat of fission products.

With an unforeseen 30 s of delay, at t = 7215 s, main **Quench** water is pumped into the system (at elevation -412 mm) at a flow rate of 42 g/s, corresponding to an average velocity of 1.4 cm/s, with a bulk temperature of 400 K. This flow is kept for 255s.

In Figure 3.11 it is presented an overview of supplied power and hydrogen generation during quench phase.

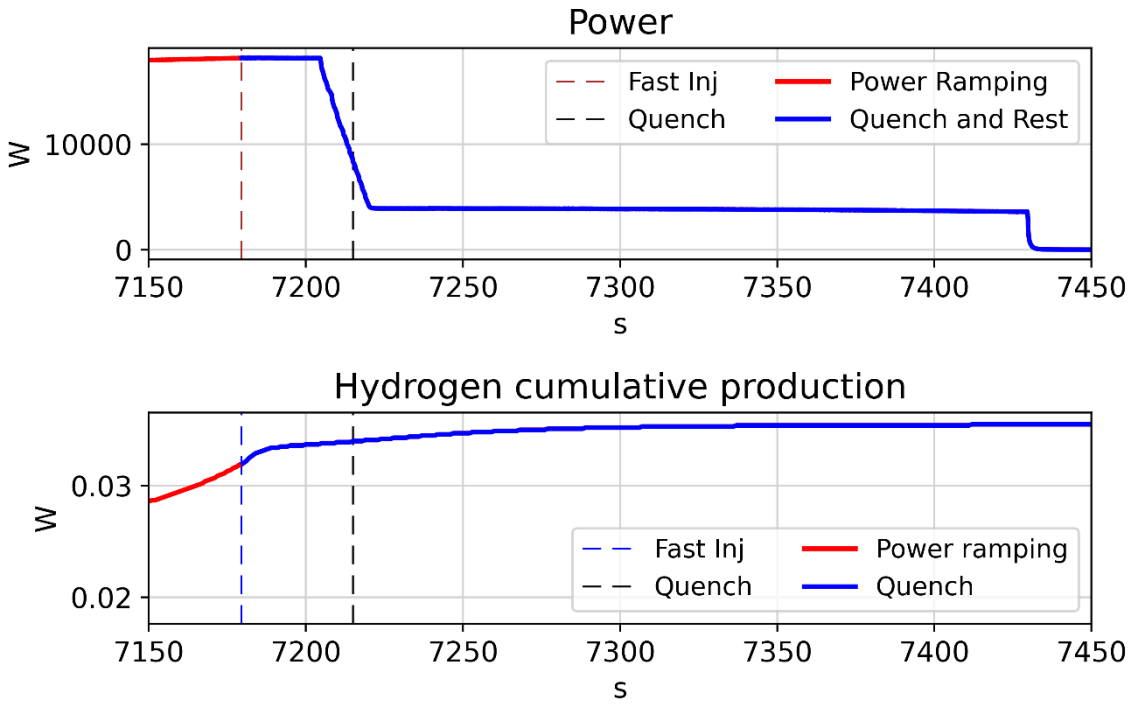

Figure 3.11: Quench stage overview

Quenching stage is aimed to simulate the termination of the evolution of a system in DBA towards a DEC scenario. As safety procedure, quench is quite critical because of the thermal shock induced into the structures and the risk of a sudden steam flash. However, it is effective in stopping the corrosion reaction on cladding and increasing heat removal from fuel pins. In a real prototypical system, the core-covering pool must be maintained until fuel assemblies are sufficiently cold to allow for a correct control and mitigation of the consequences.

Hydrogen production keeps occurring even after water fast preinjection, because electric power is still capable of inducing a partial evaporation, increasing cladding temperature again between t = 7179.5 s and t = 7215 s. However, with the on-set of the main quench insertion, zircaloy temperature has been lowered enough to not trigger anymore oxidation reaction, and hence hydrogen generation is fatally ended.

At around **t = 7430 s**, quench phase is stopped, and electric power is set to zero.

3.4.4. Rest

When main pump stops to insert quenching water into the system, the simulated progression of the accidental scenario is ended. The system is currently crossed by 3 g/s of argon entering from the upper plenum. Electric voltage at clamps is turned

off. At **t = 9000 s** experiment is concluded with the bundle being isothermal at 400 K. Measurement recordings are interrupted at **t = 11420 s**.

The complete sequence of events is depicted in Table 3.3.

Time [s]	Event
0	Bundle is prepared, isothermal condition at 873 K and power at 4 kW. Argon and steam flow enter in the lower plenum.
1955	Start of preoxidation phase, power at 11 kW and bundle is brought at 1473 K
5922	Data acquisition frequency enhanced at 5 HZ
6011	Power ramping starting point
6620	Corner rod B is withdrawn from the system
7100	Temperature escalation, massive hydrogen production and thickening of oxide layers on zircaloy
7179	Fast preinjection, rod failure. Steam injection is ended, while argon is switched in bundle head.
7180	Shroud failure
7215	On-set of quenching phase, power set to 4 kW
7430	Quench water shutoff, bundle disconnected from the grid. Test section is crossed by argon flow.
11420	QUENCH-06 terminated

Table 3.3: QUENCH-06 description [11]

3.5. Main test results

Test section is monitored by a great number of sensors, and it is beyond the purpose of this current work to describe each trend. Nevertheless, in order to represent the main phenomenology and to get the overall behavior, the following Figures of Merit (FOM) are selected:

- Pressure
- Hydrogen production
- TFS2/1 and shroud temperature at Elevation (EL) -250 mm

- Complete trend of temperature at EL 50 mm
- Complete trend of temperature at EL 950 mm
- Complete trend of temperature at EL 1250 mm
- Axial temperature of heated rod and shroud in preoxidation, power ramping and during quenching
- Oxide layer thickness for corner rod prior to quenching, and for heated rods, corner rod and shroud at the end of the test

In the next sections, brief description of each FOM will be presented. Experimental data reported in previous and next chapters are kindly offered by *Karlsruhe Institut fur Technologie*, Germany.

3.5.1. Pressure

System works at a pressure around 2 bar. Until any water injection, pressure drop between inlet and outlet pipe (vertical span: 1800 mm) is 8700 Pa, mainly due to concentrated losses of the grids. Given the considerably low density of the mixture, the accelerative and frictional terms may be neglected. With the water flow rate entering into the test section, pressure gradient increases and become stationary to 0.2 bar (hydrostatic content) after the power shutdown. Wavy trend shown in Figure 3.12 is explained by small fluctuations around 6 g/s in the inlet flow.

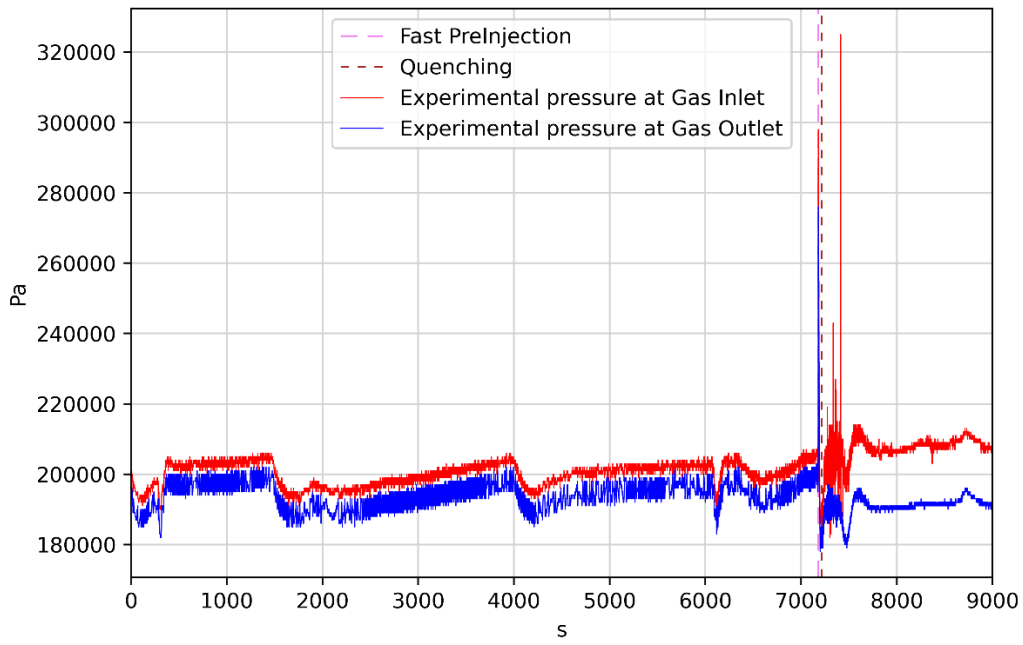

Figure 3.12: Test pressure

3.5.2. Hydrogen source term

Once zircaloy cladding surface temperature overcomes 1100 K, oxidation reaction starts, and the progression of hydrogen production is sub-linear. In power ramping stage, generation rate has a more pronounced exponential trend, meaning of an increasing zircaloy consumption rate. Then, between fast preinjection and main quenching, partial evaporation of water enhances again cladding temperature, causing an additional production of about 4 g in 30 s [11]. **Integral H_2 mass is around 36 g.**

In Figure 3.13 on the right is possible to notice how the three detection devices measure different values of cumulative hydrogen generation. PRISMA output is overestimating the value, maybe polluted by some moist left after the condenser. GAM-300 response will be taken as reference.

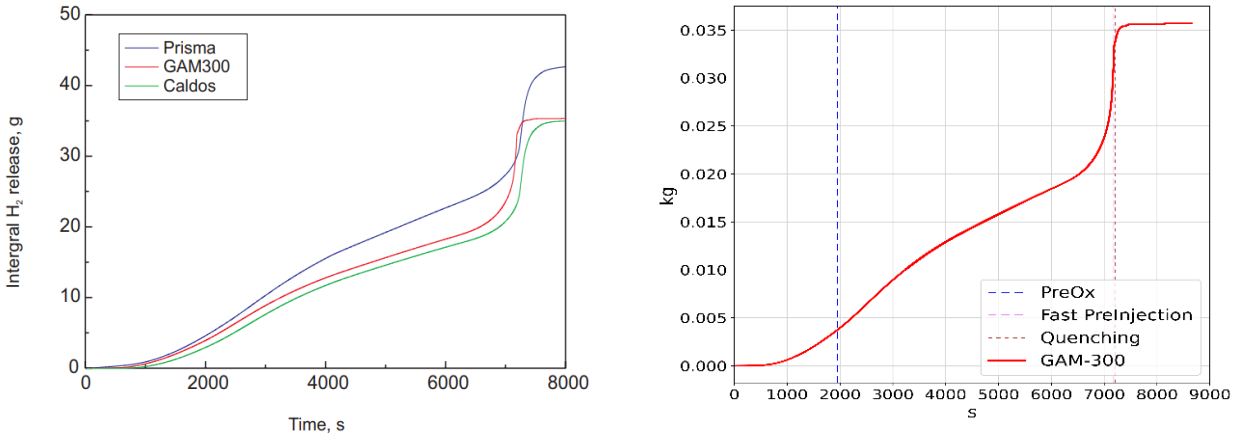

Figure 3.13: Hydrogen response [11]

3.5.3. EL: -250 mm

Sixteen centimeters above the insertion of the inlet pipe, **EL: -250mm** THCs report values of gas and thermal insulation temperature constant in time. At this elevation indeed, there is no tungsten electric wire in the centerline of FRSs, but just molybdenum electrode. Hence, given the rather low resistivity of Mo, power released through Joule effect is negligible and the system does not show any significant heat up (Figure 3.14). Temperature drop after fast preinjection is prompt at t = 7179.5 s and no re-evaporation effects are displayed.

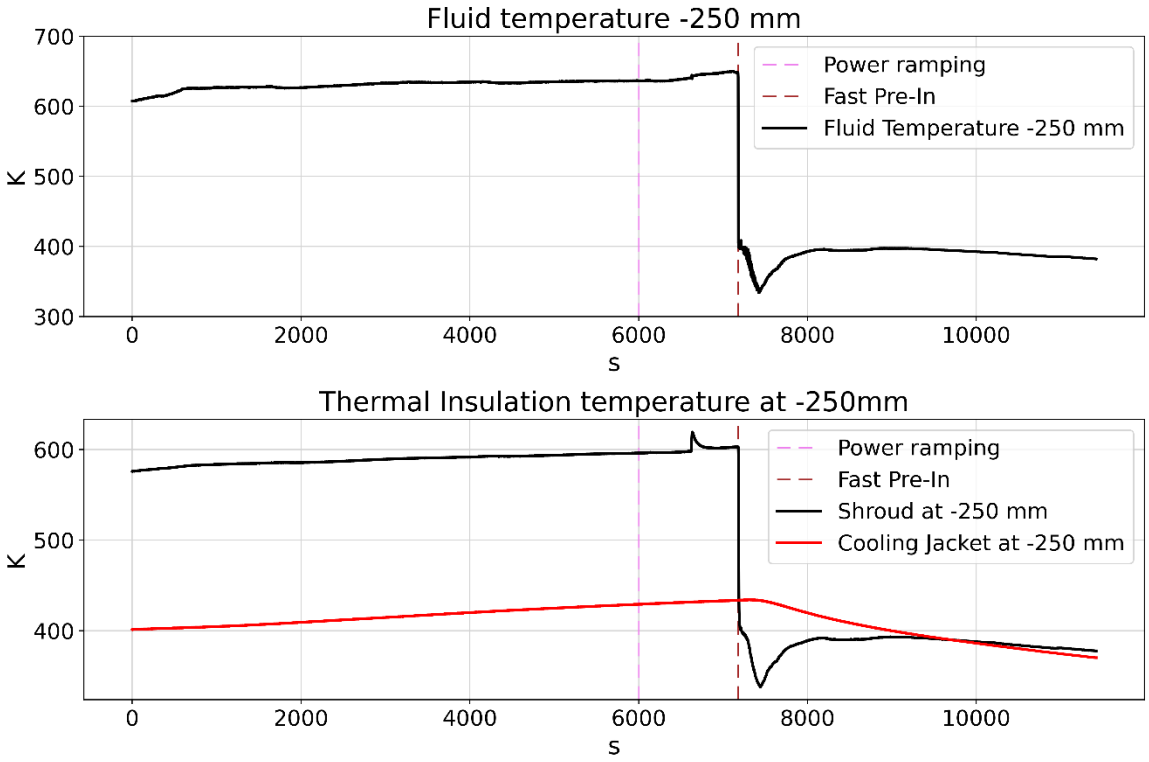

Figure 3.14: EL -250mm

3.5.4. EL 50 mm

It must be specified that as *temperature in one point*, or *temperature of a given structure*, it is meant the average value reported by all those surface THCs at the relative height of a single component facing the four orientations. Although it is true (as shown in [11]) that items present some temperature and oxide layer differences, even at the same altitude, but at several azimuthal degrees, SA codes are not able to detect these variations at all, since their treatment is purely **lumped**. Hence, for sake of simplicity, single height will be represented with a single temperature. Furthermore, from now on, **this work will address fuel rod simulators by considering an equivalent one for ring #1 and for ring #2**. Even if this approximation seems unreasonable given the anisotropy of phenomena like surface cracking and relocation, it is supported by the fact the bundle radius is 4 cm. Hence, giving the tightness of the facility, and the fact that electrical power supplied to each ring is uniformly subdivided among rods, equivalent rod model for each ring can be assumed without major loss of detail.

THCs wielded to structures at this altitude show a slight increase in both FRS and shroud temperature in time, as it is presented in Figure 3.15. It implies that a higher heat flux is established across tungsten wire, ZrO_2 pellet and cladding. Flowing mixture in this region is substantially removing power from heated rods through

convection and releasing a fraction of it to the shroud inner surface, which heats up consequently. It is firstly noticeable a new temperature ramp in FRSs after fast preinjection, meaning part of the liquid water evaporates again.

It must be highlighted that a tight bundle layout (Outer Ø181.7 mm, ΔH 2.5 m) like QUENCH-06, characterized by **a high surface-to-volume ratio**, is estimated to transmit up to ¼ of the inserted power towards the environment, something that is not representative of a prototypical system.

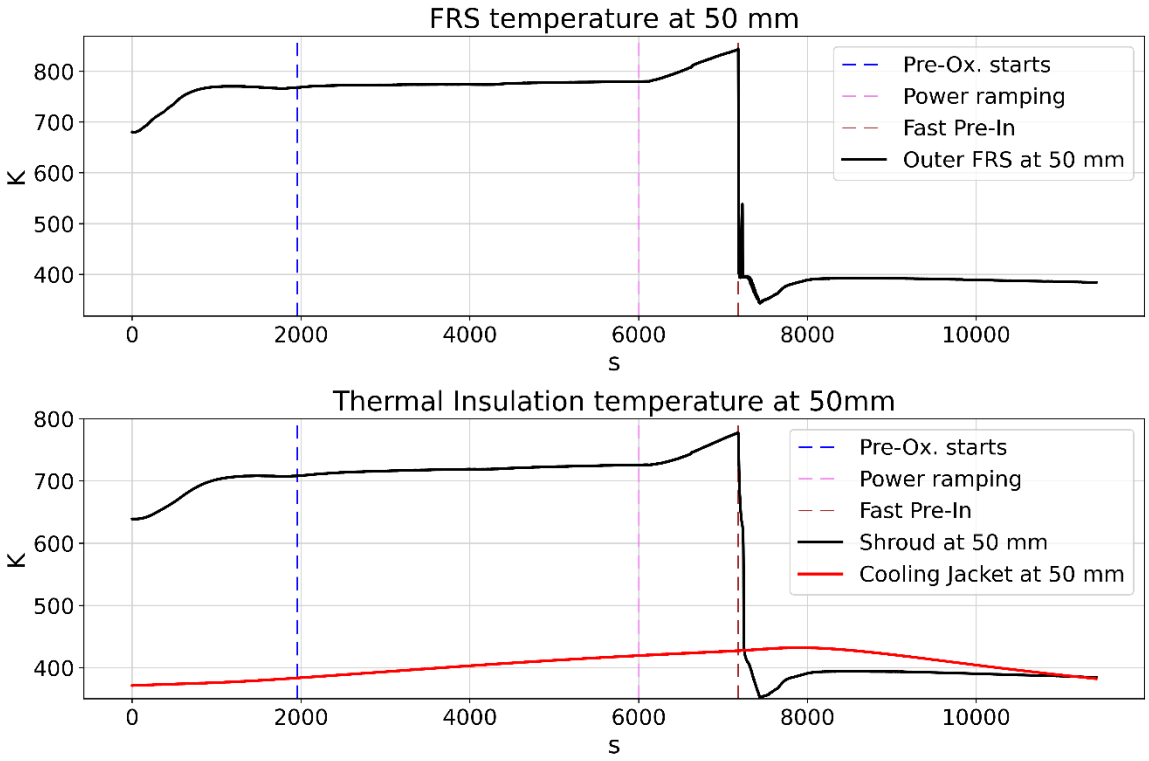

Figure 3.15: EL 50 mm

From EL 0 to EL 1024 mm zirconia fiber sponge is inserted between shroud outer surface and inner cooling jacket. Its porous matrix is filled by steady argon. As shown in figure before, and as it will be plotted again, this insulation layer introduces a very high thermal resistance, which causes a low heat up of the cooling jacket even when power grows up significantly.

3.5.5. EL 950 mm

This reference height is characterized by the most severe condition. It is the highest detecting point in active region, where thermal excursion is the greatest, and the thickest oxide layer is established. Flowing mixture reaches peak temperature at the

active end point, forcing a considerable heat flux towards zircaloy shroud and thermal insulation.

During preoxidation, temperature is about 1473 K, and corrosion on zircaloy by steam is still occurring. In the heat transient prior to quenching, FRSs suffer thermal dilatation and distortions, even if no rod-to-rod contact is reported [11]. Unheated central rod has caught some melt wetting its outer surface and it is affected by pellet-cladding interaction in the inner. Since clad temperature has easily overcome 1900 K, steam oxidation is greatly aggressive, and, as expected, post-test metallographic analyses report an advanced duplex oxide layer (ZrO_2 ceramic layer outside, stabilized α-Zr(O) below). Moreover, during power ramping voids are forming in crystalline structure of zircaloy due to creep, hydrogen embrittlement and downward melt relocation. Consequently, once fast preinjection sharply cools down the bundle, cladding is easily damaged by expanding flaws. Then, given the still high power supplied in between the two water insertions, the hot steam generated by pool evaporation diffuses into these cracks, enhancing oxidation in depth. Shroud has gained an oval shape [11], and it has been pierced due to corrosion, allowing for steam intrusion in zirconia sponge. Shroud oxidation is one of the main sources of hydrogen production.

Figure 3.16 contains the overall temperature trends of the bundle at 950 mm.

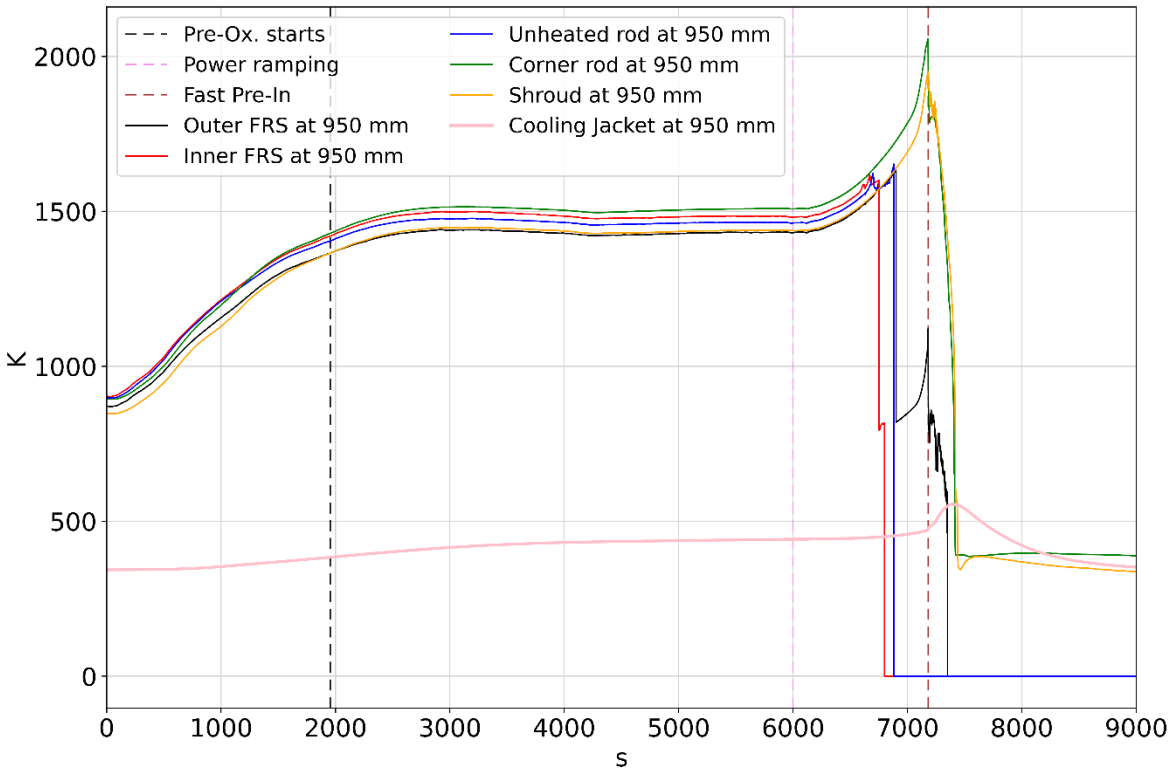

Figure 3.16: EL 950 mm

Thermocouples placed on the FRSs and central rods fail during the power ramping phase. However, based on the values detected by other devices, it is possible to assume that maximum temperature, hit just before fast preinjection, is around 2100 K. Thermal gradient in radial direction is rather small, supported by the facts that:

- even if shroud and corner rod (placed at the periphery of the facility) have no power source, the energy released by zircaloy oxidation heats them up, enhancing radial tails of temperature profile.
- Thermal resistance offered by zirconia sponge establish a very low conductive heat flux towards the environment.

3.5.6. EL 1250 mm

Molybdenum upper electrode is quite ineffective in transmitting power into the flowing mixture. Hence, structures at this point are characterized by lower temperature than below, and a more pronounced thermal gradient in radial direction. At this elevation indeed, zirconia fiber outside the shroud is replaced by an **argon filled volume**, in which it is inserted the expansion compensator (made of steel). Given this change in facility layout, **thermal insulation system is now able to rely on both conductive** (still a poor content) **and radiative energy transfer** towards the jackets and consequently the containment, so radial losses are more relevant, as presented in Figure 3.17.

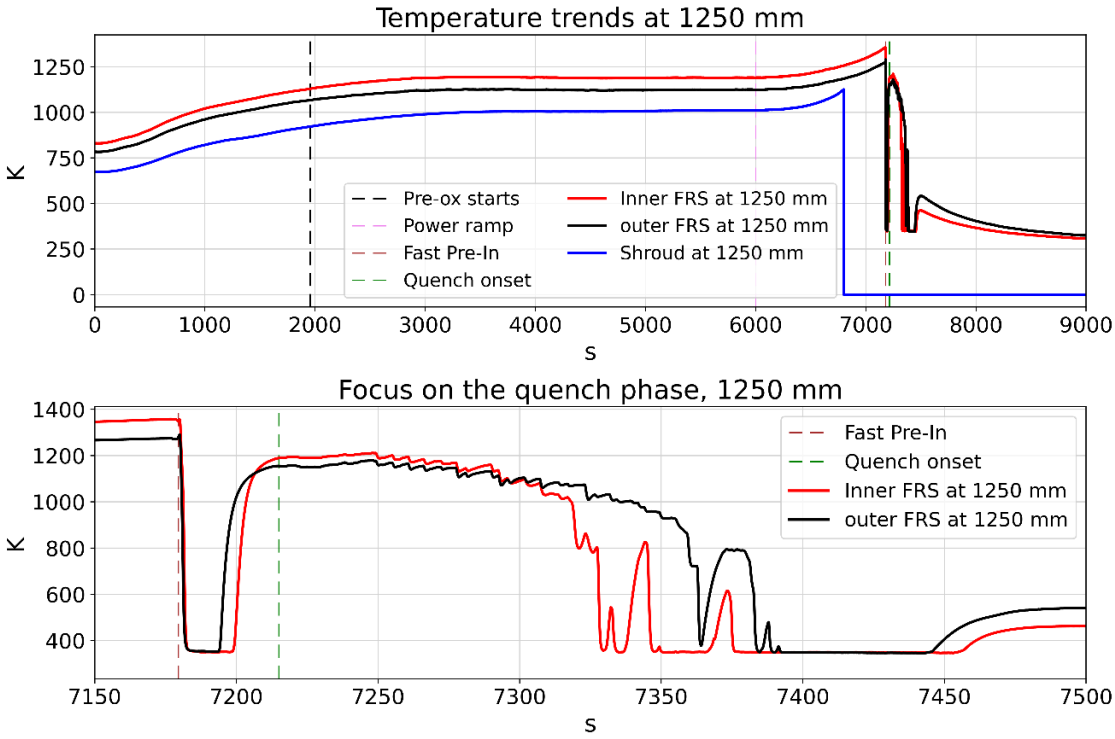

Figure 3.17: EL 1250 mm

Figure 3.17 emphasizes the clear evaporation of preinjected water that increases again the surface temperature of solid structures ahead of the main quenching, even if power is greatly reduced.

This is a crucial result because it becomes obvious that a fast, δ-shape subcooled water flow is not able to suppress by itself the accidental progression of simulated DBA towards a DEC. In addition, argon flowing downward between 7179.5 s and 7215 s is not capable at all to ensure a heat transfer removal from the pins, and hence cladding temperature is enhanced again turning back on hydrogen production.

As concern main quenching, bundle is characterized by slow but enduring decrease in temperature down to 400 K.

3.5.7. Axial temperature profile

From experimental measurements exploited as validation dataset for the open phase of OECD ISP-45 it is possible to extrapolate the temperature distribution of several structures of the test bundle at different stages. This analysis, coupled with the following description of the oxide layers, is of key importance to check the validity and the good response of the corrosion correlations (that link reaction rate with surface temperature) embedded into SA codes.

Figure 3.18 reports the axial profile of the equivalent inner ring fuel rod simulator cladding and the shroud. Except from the meaningless 0 K in correspondence of failed THCs, trends deliver interesting insights that need further explanations.

First of all**, axial temperature profile in active region grows linearly in vertical direction**, reaching a peak at 950 mm. This fact implies that the power generated in the tungsten wire is axially uniform not function of the position. So, by considering convective heat transfer equation with constant heat flux, both flowing mixture and cladding temperature linearly increase, as depicted in the figure below. This behavior is not representative of neither PWR core, in which the mixture heats up vertically following a sine-shape, with power flux being cosine-shaped, nor BWR-like, where the hottest point is even more shifted in middle core region.

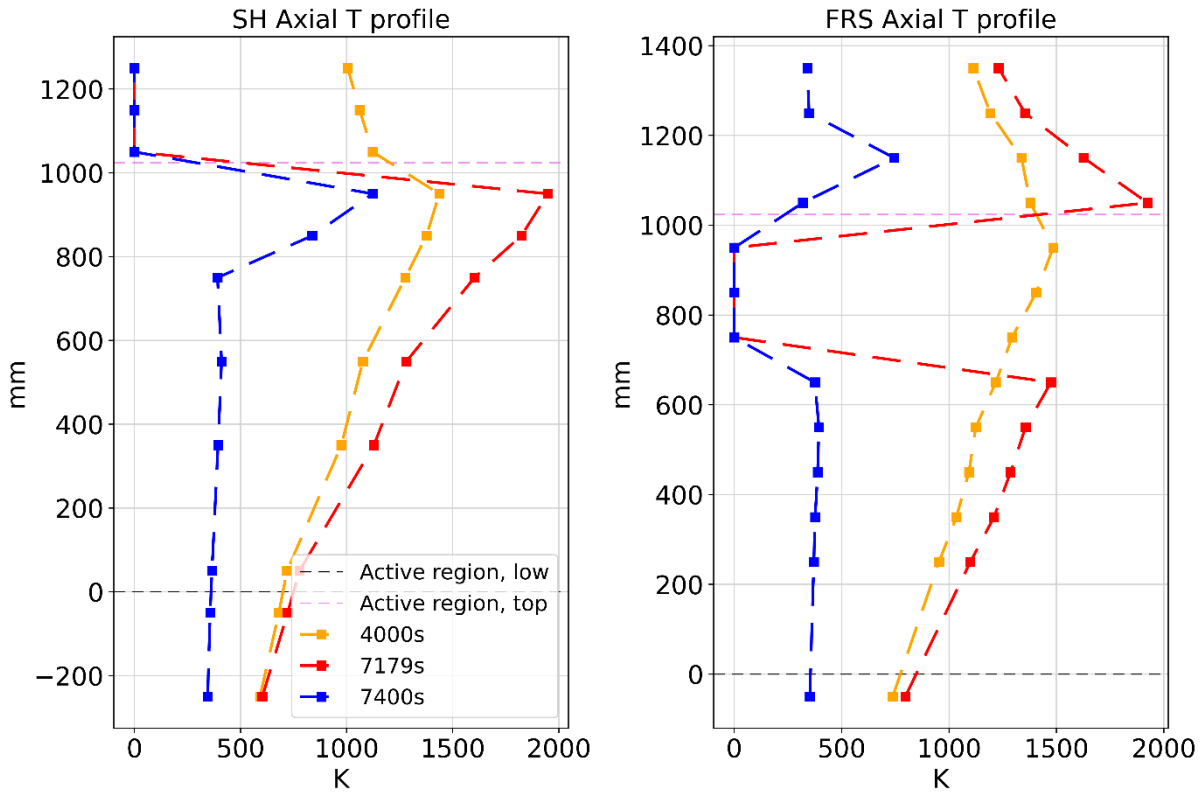

Figure 3.18: Axial Temperature profile

The other important aspect is that even at the end of quenching phase, bundle is not entirely filled with water. This consideration is guessed by the shroud temperature profile at 7400 s. It is almost constant at 400 K up to 800 mm, while above there is a thermal gradient of more than 40 K/cm. This outcome should highlight the fact that the simulated prototypical system, still heated up by decay heat, has some challenges in the highest region still long after quenching injection.

3.5.8. Oxidation Profile

Figure 3.19 describes both the oxidation profile of the withdrawn corner rod B at t = 6620, and the final oxide thicknesses of shroud, FRS, and corner rod A.

Values measured on corner rod B are relevant to evaluate the progression of zircaloy corrosion int the preoxidation phase, characterized by a stationary temperature. For evaluating the thickness, two different experimental methods [11] are adopted: metallographic analysis (which outcomes are shown in figure) and eddy-current (which usually depicts thicker layers). Measurements at 950 mm reports a value of 200 µm (6.9% of corner rod thickness).

At the end of the test, structures display slight oxidation and thin oxide layer up to 800 mm. Then, the more severe conditions cause a steep increase in the oxide layer until 950 mm, in which:

- FRS cladding is oxidized at 91%
- Corner rod at 16%
- Shroud at 21%.

Zircaloy cladding has almost entirely been oxidized to ZrO_2 at that elevation.

It needs to be added that post-test examination, as mentioned above, exhibits a shroud failure between 837 mm and 1000 mm. Actually, pierce and melted material are localized between 270° and 0° in the azimuthal reference. A so advanced corrosion generates scale growth stresses that bends fuel rods and shroud [11], altering geometry and bundle layout modifying the flowing direction. This fact could establish positive feedback on the oxidation process because some portion of the structure area may suffer hot spots. Additionally, post test assessment of the bundle integrity has proven the partial dissolution of zircaloy grids, allowing for a free bending of rods.

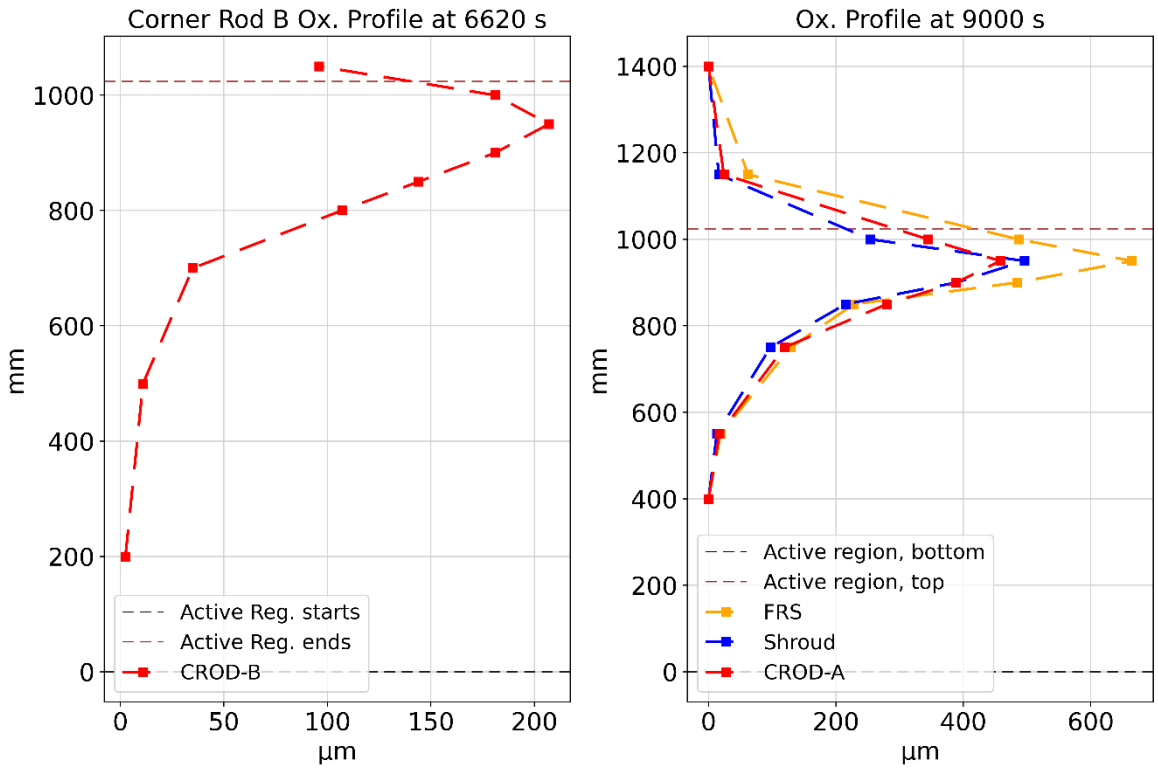

Figure 3.19: Oxide layers thickness

Concurrent to the evaluation of oxide layers progression, it is useful to estimate hydrogen absorption from zircaloy items. Hydrogen diffusion is a crucial source of

embrittlement in PWR claddings, in which primary circuit feels an H_2 overpressure to limit the radiolysis of water molecules. It is reported [11] that hydrogen absorption spans from *5 at-% to 10 at-%* in metal phase, with a peak value localized at 950 mm of *24 at-%*.

3.6. Test additional comments and summary

Prior to preoxidation phase, a partial condensation of the 3 g/s of steam flowing in the bundle is detected in the off-gas pipe, whose walls are cooled by isothermal water at 300 K.

In QUENCH-06 a total mass of 14.6 kg of subcooled water is inserted to suppress the progression of a simulated accidental scenario, which is responsible for the production of 36 g of hydrogen. Quenching is not able to entirely drown the bundle, but a dynamic equilibrium between the water entering the system and the produced steam (by residual heat representing decay power) is established, as shown in Figure 3.20.

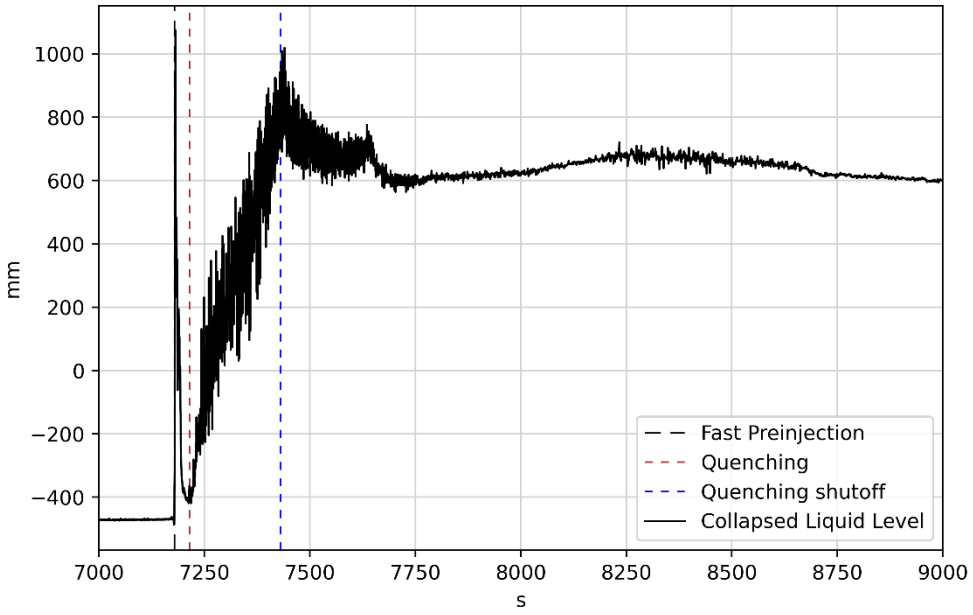

Figure 3.20: Liquid level

QUENCH-06 has withstood transient with almost intact geometry [11], even if its layout has been modified by thermal dilatation and stresses. Cladding structures are characterized by an advanced Zirconia layer and an embrittled structure, with multiple failures mainly due to crack propagation.

Experimental datasets of QUENCH-06 deployed by KIT will be used as validation matrix for a MELCOR code case study. Hence, next chapter will be devoted to a brief but exhaustive presentation of MELCOR code, with its main features.

4 MELCOR Code

MELCOR code is a fully integrated, engineering level computer code developed at Sandia National Laboratory (SNL) for the U.S Nuclear Regulatory Commission (USNRC) as a second-generation plant risk assessment tool [13]. Intended users of MELCOR code are regulators, researchers, and industry as well [6].

It is devoted to simulating both stationary and transient conditions occurring in LWR, SNF pools and gas reactors [6], with the capability to cover a wide range of phenomenologies regarding SA scenarios [14], such as:

- Single-phase and two-phase thermal-hydraulic response in the primary circuit and outside the vessel;
- Cladding oxidation;
- Core heat up, degradation and relocation;
- In-vessel and ex-vessel hydrogen production and combustion;
- Core-concrete interaction;
- Fission products release ;
- Aerosol behavior in the containment.

As mentioned in Section 2.3.1, MELCOR architecture consists of a series of **packages** in which a full set of equations describing a specific phenomenology is implemented. Package are linked through interfaces that internally share information and data, in order to couple all phenomena [14]. Most of the models adopted in each unit of MELCOR are mechanistic with high degree of accuracy, achieved after continuous updating of the code thanks to the several validation steps it has undergone. Furthermore, the tool allows for user-modifications of a large number of options so an easy assessment of each case study may be performed. Among the options upon which users have possibility to change, also single model parameters may be varied to conduct a serial uncertainty analysis.

System modeling in MELCOR should be kept simple but at the same time exhaustive with the objective of capturing the important physics processes effectively with rather small computational effort. Choices for the nodalization are

completely free, except for the core representation, in which pre-built templates must be used.

MELCOR calculation is carried out in two consecutive steps. First step, called **MELGEN**, processes, and checks the input. Then, if no errors are found, a Restart File is written and **MELCOR** is allowed to advance the problem through time schedule.

In the next chapters main MELCOR packages and models will be presented.

4.1. Control Volume Hydrodynamics Package

This unit, coupled with Flow Path (FL) package, is entitled to describe the behavior of the *hydrodynamic material* in the system. Hydrodynamic inventory embeds liquid phase, steam, non-condensable gasses and fog but it does not include aerosols nor melted debris. Each control volume is characterized by pressure, temperatures, masses, and energies.

CVH geometry [13] is defined considering a portion of space available for fluids on the basis of a **volume-to-altitude** table, as plotted in Figure 4.1. Vertical span is sub-divided into segments, to whom a single volume is associated. Obviously, volume at the lowest altitude has to be set to zero, and then it grows linearly by cumulating all sub-volumes labelled to the relative segment. Uppermost segment will be characterized by a volume equal to the total control volume.

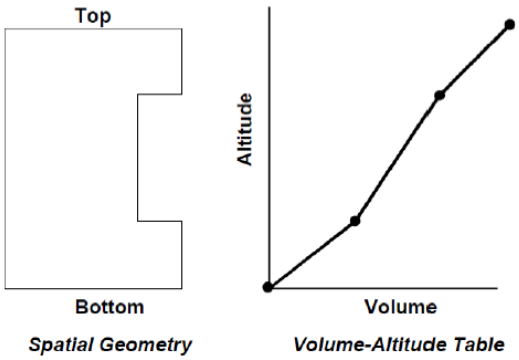

Figure 4.1: CVH geometry [14]

MELCOR requires that a single overall reference value for the altitude is established, in order to check if geometries of control volumes are in compliance with core cells (COR package) and heat structures (HS package).

While evaluating initial total volume in CVH settings, user should discard all the solid items that occupy a selected portion of space in the real system (for instance

the inner cylindrical volume of the RPV shall be reduced by a content accounting for fuel assemblies, grids, control rods, barrel, plates …). However, since it is most likely that a portion of the core melts during the accident simulation, control volume is flexible and it may increase or decrease according to changes in layout after any core relocation.

Control volume is occupied by two phases: a **pool,** and an **atmosphere.** Pool always lies below the atmosphere, and it contains liquid or two-phase water, while steam, non-condensable gasses and fog droplets are placed in the atmosphere. CVH forces the two phases to be in pressure equilibrium ($p_{atm} = p_{pool}$) while the thermal equilibrium may be enabled but it is usually discouraged. Basic information necessary for initializing thermo-dynamical state of the volume are:

1. Pressure of the volume (**lumped** parameter);
2. Temperature of each phase (or a single value if thermal equilibrium is imposed);
3. Volume-to-altitude table;
4. Mass, or volume, or elevation, of the pool;
5. Additional species in the atmosphere, if present, by means of partial pressure, dew point, humidity, mass fractions …

Furthermore, each control volume may be set to *Active* if its thermal-hydraulics has to be updated each time step, *Constant* if properties are not allowed to change or even *Time-Dependent* if the evolution is a priori imposed by the user.

Materials in control volumes are labelled with numbers. Pool, fog, and steam in atmosphere are respectively set as 1, 2 and 3. Any other gas, or liquid component that has to be inserted into the volume may be called through a sequence number (from 4 on) that identifies a species in the **Non-Condensable Gasses Package**.

Additionally, user may explicitly add in each control volume mass and energy sources/sinks regarding a specific material, in terms of absolute quantities or rates. These commands are submitted to MELCOR through devoted packages, such as **Control Function Package** (CF) or **Tabular Function** (TF), which gather vectorial quantities inserted by the analyst and submit them as commands to each package (i.e., it is possible to specify how much water the accumulators insert into the primary circuit, what will be the temperature of a given structure for the whole simulation or decay heat trend). Energy sources or sinks may be expressed by means of temperature. If a control volume has a superheated steam source (or subcooled water), its enthalpy will be address by considering the temperature vector specified in the CF package and the pressure of the control volume itself,

which is allowed to vary during the calculation. Heat sources are incorporated in CVH equations from other packages, usually COR and Heat Structure.

Equations embedded into the CVH package aim to resolve mass and energy conservation for all the species belonging to the control volume, and their transfer between pool and atmosphere.

4.2. Flow Path Package

Flow Path (FL) package describes the connections between control volumes, modeling **motion of fluid** and **pressure drops**. Materials in each flow path have no residence time, hence no sources of heat and mass may be introduced. Furthermore, FL equations do not calculate energy and mass transfer between the two phases flowing, but they allow pool and atmosphere to exchange momentum.

Flow paths have to be horizontal and/or vertical, linking a *from* control volume to a *to* control volume, as shown in Figure 4.2. Junctions, namely insertion points of each flow path into a CV, may be at different altitudes. Positions of the junction FL-CV are important to define flowing materials, velocity, and void coefficient of the mixture. All these parameters will be boundary condition for the *to* control volume resolution schemes.

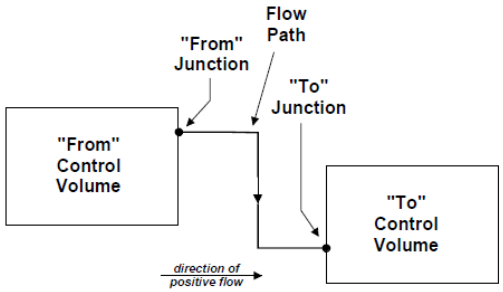

Figure 4.2: Flow Path [14]

Main features for initializing a flow path are Area (FLARA), and Length (FLLEN). If the flow path represents a **pipe**, area will be cross-sectional area and FLLEN its actual length. However, pipe has to be model also through CVH in order to account for the above-mentioned mass-energy transfers not embedded in FL. Flow Paths may refer even to the **open connections between control volume**s (for instance, modeling the interface between two adjacent control volume in the core region). In this case, FL area shall be the coolant passage area, and the length equal to the difference between bottom and top altitudes of one of the linked CVs. Doing so it is possible to fully evaluate distributed pressure drops occurring in the vertical span covered by the control volume.

As shown in the figure above, each flow path can be sub-divided into segments, whose lengths will be used for the determination of the distributed pressure losses. FL package has additional features that could be specified to account for form drops, pumps, valves and blockages, and flow direction.

FP equations describe single phase motion and a wide range of two-phase flows (supported by proper models of momentum transfer, void fraction, slip factor and flashing). In addition, they assess form, gravitational and frictional pressure losses.

4.2.1. CVH-FL Governing Equations

CVH equations are tightly bounded with FL equations to evaluate thermal-dynamical evolution of the hydrodynamic material.

If thermal equilibrium between the two phases is selected, treatment of the following equations will be fully explicit. If it is not, a **semi-implicit formulation** of the governing equation will be adopted to ensure a timestep always greater than acoustic Courant limit [14]. Courant number is defined as in (4.1):

$$Co = \frac{v\Delta t}{\Delta x} < Co_{max} \tag{4.1}$$

with v being species velocity, Δt timestep, Δx center-to-center distance of the two connected control volumes, and C_{max} parameter specific to each case ($C_{max} > 1$ for implicit description).

Conservation of mass [14] for each material in CVs is presented in (4.2):

$$\frac{\partial \rho}{\partial t} + \boldsymbol{\nabla} \cdot (\rho v) = \boldsymbol{\Gamma} \tag{4.2}$$

with $\boldsymbol{\Gamma}$ volumetric mass source density, ρ material density and v its velocity. Then, integrating it on the i-th control volume for the m-th material, it becomes (4.3):

$$\frac{dM_{i,m}}{dt} = \sum_j \sigma_{ij} \alpha_{j,\phi} \rho^d_{j,m} v_{j,\phi} F_j A_j + \dot{M_{i,m}} \tag{4.3}$$

with j subscript for the flow path, σ_{ij} factor that accounts for the direction of the flow in respect of i-th control volume (sign-function, or null), ϕ for phase (atmosphere or pool) in which material m belongs, $\alpha_{j,\phi}$ volume fraction of ϕ-phase in the j-th FL, ${\rho^d}_{j,m}$ density of the m-th material extracted from d-th donor *("from")* CV in j-th flow path, v velocity of ϕ-phase in the j-th FL, A flow path area, F its open

fraction (0 < F < 1) and finally $\dot{M_{i,m}}$ external sources of mass flow for the particular material in the control volume.

Energy conservation for pool and atmosphere is derived similarly from partial differential equation [14], neglecting gravitational potential energy and volume average kinetic energy terms, as expressed in (4.4):

$$\frac{\partial E_{i,\phi}}{\partial t} = \sum_j \sigma_{ij}\alpha_{j,\phi}\left(\sum_m \rho_{j,m}^d h_{j,m}^d\right) v_{j,\phi}F_j A_j + \dot{H_{i,\phi}} \tag{4.4}$$

where $h_{j,m}^d$ is the specific enthalpy of m-th material in flow path j coming from d-th volume and $\dot{H_{i,\phi}}$ the non-flow energy rate for the ϕ phase into the i-th CV (energy sources inserted by users).

Velocity field in j-th flow path for the m-th material is determined by resolving the 1-D line integral of the acceleration equations along a streamline from the center of the *from* control volume to the center of the *to* control volume (its representation is comprehensively reported in *Chapter CVH/FL-RM-19* [14])

This set of ordinary differential equations is converted to linearized-implicit finite difference equations for solution in MELCOR [14]. The new velocity calculated at end of step is inserted in the advection term of (4.3), (4.4) to update materials mass and control volume phases energy. Anyway, iterative procedure is needed due to the non-linearity of frictional term in pressure drop formulation, which is depicted below.

Total pressure drops [14] in a flow path are evaluated as in (4.5):

$$\Delta P_{j,\phi} = \frac{1}{2}\widetilde{K}_{j,\phi}\rho_{j,\phi}|v_{j,\phi}|v_{j,\phi} + \sum_s \frac{2f_{\phi,s}L_s}{D_s}\rho_{\phi,s}|v_{\phi,s}|v_{\phi,s} + \rho_{j,\phi}g\Delta z \tag{4.5}$$

where $\widetilde{K}$ is form loss coefficient (user specified), f the Fanning friction factor for the s-th sub-segment of length L_s and diameter D_s the flow path. Fanning friction factor for frictional losses are calculated both for single phase mixtures (classical formulation of Poiseuille for laminar, Colebrook-White for turbulent regime) or by means of two-phase wall friction if atmosphere and pool are flowing at the same time.

4.3. Heat Structure Package

Heat Structure (HS) package calculates 1-D thermal conduction across solid, intact structures with boundary conditions set at the two surfaces. MELCOR HS may be vertical, horizontal, or inclined at any angle, and the geometries to be selected are cylindrical, rectangular, or spherical.

An example of heat structure is shown in Figure 4.3

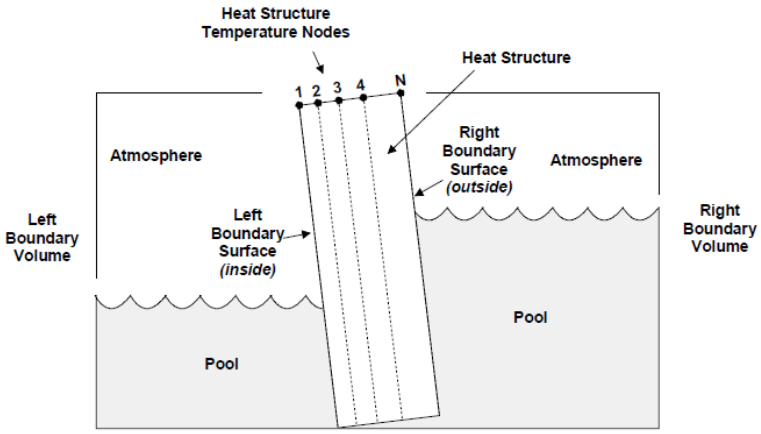

Figure 4.3: Heat Structure [13]

Each component is nodalized in intervals, specified by the user and may be non-uniform. On the *Inside* surface N = 1 node is placed, while the *n*-th node is located at the *Outside* surface. The region between two adjacent nodes is called *mesh interval* and it may be filled by any solid specified in the **Material Package** list, that contains all the required info about the thermo-mechanical properties of the materials too.

For the initialization of the single heat structure, boundary conditions and characteristic parameter on the two surfaces must be provided.

Boundary conditions may be:

- *Symmetry*: adiabatic surface;
- *Convection*: HS evaluates the Heat Transfer Coefficient (HTC) on the surface receiving in input thermal-hydraulics data from CVH package. This condition requires the definition of a boundary control volume;
- *Temperature, power, flux, or HTC vs time*: through CF or TF packages, previous quantities are set on the surface for the whole simulation.

In case convective condition is chosen, additional data are needed, as:

- *Area* and *axial length* of the surface;

- Characteristic lengths for the calculation of Reynolds, Nusselt, Grashof and Sherwood numbers;
- Information about the flow, if it is internal or external (to adopt the correct set of correlation).

For limiting the computational efforts, user may define a *critical pool fraction*. This quantity is the minimum fraction of wetted surface under which HS package calculates the convective heat flux coming from the control volume pool. This feature is particularly useful when the atmosphere temperature is considerably higher than the temperature of pool. The same option is available for inhibiting atmosphere energy exchange.

It is possible to insert into a Heat Structure, and specify in which mesh interval, a *power source* defined through CF or TF package.

This package is equipped with two models (*gray gas* and *equivalent band*) to account for radiative energy released on a surface from a boundary control volume.

HS package evaluates also mass transfer between the structure and the boundary volume using correlations or expression for the mass flux (usually heat-mass analogy). In addition, it implements model for the description of de-gassing phenomena through which it is possible to model ice condenser in the containment.

Solution schemes adopt **finite difference method in a fully implicit treatment to solve the integral 1-D heat conduction equation and boundary condition equation**. Since thermo-mechanical properties of the material are explicit function of the calculated temperature, an iterative procedure is required at each step. Particular attention should be given by the users on the length of each mesh interval: it should be small enough for the accurate resolution of energy and mass transfer, but not smaller than the thermal diffusion length to avoid oscillation and undesirable timestep reductions.

Thermal diffusion length [13] is reported in equation (4.6) below,

$$\Delta x \geq L_D = \sqrt{\frac{4k\Delta t_{max}}{C_p}} \tag{4.6}$$

where k is the thermal conductivity of material in the mesh interval, Δt_{max} maximum computational timestep and C_p volumetric heat capacity.

4.4. Core Package

MELCOR Core (COR) package models the thermal response and degradation of the core and lower plenum, including the lower head, in both stationary and transient condition. Therefore, it is able to describe phenomena occurring during an accidental state, such as oxide formations, melting, candling, debris formation and slumping [13]. Items represented through COR Package exchange mass and energy with control volumes and heat structures.

Nodalization is carried out by sub-dividing core region radially in concentric **rings**, and axially in **levels**. Each portion of space located in a certain ring at a certain altitude is called **cell**. This scheme is independent from the representation of control volumes and HSs, but the above-mentioned compliance in respect of a reference altitude must always be fulfilled.

COR nodalization frame is proposed in Figure 4.4.

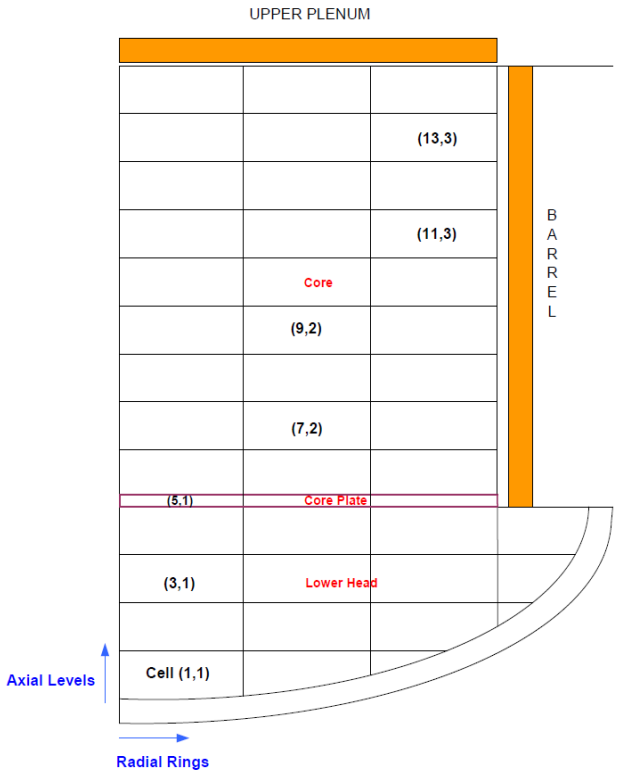

Figure 4.4: COR nodalization [13]

Each cell must be coupled with a control volume placed in the same region; for the rings it is necessary to define a unique HS with which exchange heat (usually the upper plate), while all levels have to be surrounded by relative heat structures (vessel walls for instance).

In a single cell, several intact components [13] may be modeled, as:

- fuel pellets;
- claddings;
- canister walls for BWR, PWR baffle and core formers;
- supporting structure;
- non supporting structure.

Additionally, COR allows the user to initialize cells with components that are already degraded:

- particulate debris: result of collapse of fuel rods;
- oxidic and metallic molten pools.

COR cells account for the presence of fluid to evaluate convective energy transfers but also determine the change in layout after melt relocation. The flowing mixture (single-phase, two-phase) is stored in the *channel* and *bypass* portion of each cell. As concern the channel, sum of channels flow area for all cells on a level must be equal to the ratio *volume/height* of the control volume they are interfaced with. For the bypass instead, its presence is not mandatory but usually exploited when modeling the outermost ring of PWR (where the shroud is present) or the space between assemblies in a BWR.

Each individual component in the cell is described by a lumped equilibrium temperature, on which basis are calculated internal energy and thermo-mechanical properties.

Single cell outline is shown in Figure 4.5.

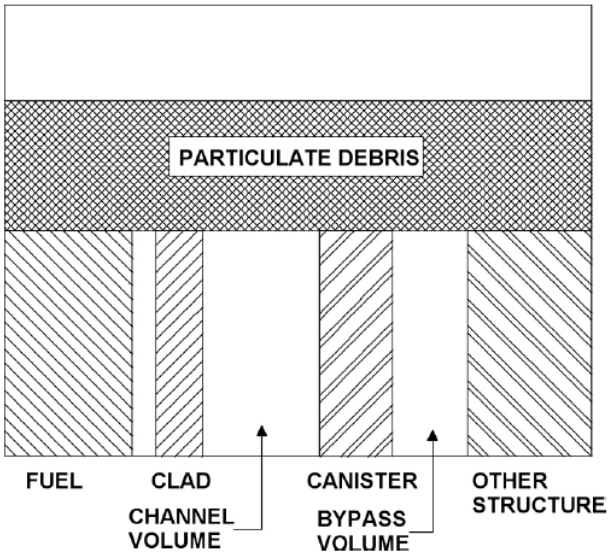

Figure 4.5: COR cell [13]

Supporting structures are cell components able to sustain their own weight and the weight of the above-placed items. They may represent edge-supported plate, grid-supported plates, and guide tubes for control rods. Once they fail, they are usually converted in particulate debris together with everything placed above. User may specify different failure criteria, mainly critical temperature, critical thickness or by means of a logic function (through which it is possible to consider creep or buckling phenomena). **Non supporting structures** are not able to carry any additional weight and they fail when the residual thickness is under a minimum value, or by overtemperature. Examples of prototypical non supporting components are control rods, control blades and stiffeners.

COR modeling of **lower head** is of key importance for the estimation of core melting progression, ablation and ex-vessel accidental progression simulated by MELCOR code. It may be represented as curved (hemispherical or truncated hemispherical) shell, or flat plate of user defined thickness and composition. Additionally, several lower head-cylindrical vessel junctions are available for including a wide range of reactor layouts. External surface of the lower head has to be coupled with cavity control volume. 2-D Temperature profile through lower head is used in the thermo-mechanical response model for the determination of stress-strain in lower head to predict creep failures by means of Larson-Miller parameter [14]. Furthermore, COR package accounts for lower head failure when differential pressure between lower plenum and cavity overcomes a threshold, when the induced strain is higher than breaking limit or on the basis of user defined logic function.

Eight different materials are embedded into COR package:

- Uranium dioxide (UO_2);
- Zircaloy;
- Zirconium oxide (ZrO_2);
- Steel (carbon, stainless);
- Steel oxide;
- Boron Carbide (B_4C) or Ag-In-Cd for control rod poison;
- Inconel;
- Additional electric heaters: Tungsten (W), Molybdenum (Mo) and Copper (Cu),

whose properties and composition may be changed through MP package. Melting, relocation and solidification are tracked independently for all COR material, unless *material-interaction model* (for eutectic formation) is turned on.

COR library contains templates of common core geometries, by which it is easier to represent reactor layout. It is possible to choose among PWR, BWR, PBR (Pebble

Bed Reactor), PHWR (Pressurized Heavy Water Reactor), PMR (Prismatic-Core Modular Reactor) and ACR-700 (Advanced CANDU Reactor).

COR cells initialization requires detailed definitions of component surface area and hydraulic diameter for the description of convective heat transfer towards the flowing phases in the channel and bypass. Moreover, user can specify view factors and cell-to-cell path lengths for the evaluation of radiative energy exchange. COR package accounts by default the conductive content between cells in the same ring.

In the next few sections, brief descriptions of interesting phenomena and related MELCOR models are reported, in view of the creation of QUENCH-06 MELCOR input.

4.4.1. Oxidation Phenomenology and COR Modeling

MELCOR implements oxidation models for multiple material, like zircaloy, steel and boron carbide. Code is able to predict B_4C corrosion accurately both in oxidizing and reducing environment by means of two different correlations. Metal oxidation is calculated following a standard parabolic kinetics approach: in case of isotherm system, oxide mass on the metal grows as the square root of time, as presented in equation (4.7) of solid-state diffusion of oxygen in metal layers:

$$\frac{dW^2}{dt} = K(T) \tag{4.7}$$

with W being mass of oxidize metal per unit surface of metal and K(T) Arrhenius-type reaction rate. MELCOR allows oxidation for zircaloy cladding, canisters, and control rod guide tubes. Stainless-steel components that may oxidize are supporting and non-supporting structures. Conglomerate debris is also included as material available for oxidation, but it is usually deactivated [14].

In particular, **Zircaloy corrosion** needs for further study since it will be of key importance in QUENCH-06 input. The phenomenon starts when metal surface temperature overcomes 1100 K (but this *cut-off temperature* in MELCOR may be changed via sensitivity coefficient) in two concurrent ways, in which water and oxygen molecules acts as oxidants:

$$Zr + 2H_2O \rightarrow ZrO_2 + 2H_2 + Q_{ox,water} \tag{4.8}$$

$$Zr + O_2 \rightarrow ZrO_2 + Q_{ox,oxygen} \tag{4.9}$$

with exothermal power calculated from the enthalpies of reactants and products [14], as presented in (4.10), (4.11):

$$Q_{ox}(T) = Q_{ox}(T_0) + H_{rp}(T) - H_{rp}(T_0) \tag{4.10}$$

$$H_{rp}(T) = H_r(T) - H_p(T) \tag{4.11}$$

here H_r is reactant enthalpy, H_P product enthalpy and T_0 reference temperature of NCG package. The oxidation reactions of zircaloy are greatly energetic, since $Q_{ox,water}$ is around 5.797 MJ/kg$_{Zr}$, while $Q_{ox,oxygen}$ 12.065 MJ/kg$_{Zr}$. Control volume temperature is set as T for the determination of reaction rate and energy released in the material undergoing corrosion.

MELCOR by default adopts the **Urbanich-Heidrich** [13] correlation for Zircaloy-Steam corrosion, with transition temperatures at 1853 K and 1873 K. Code interpolates K(T) between the two transition temperatures. Exceeding upper threshold temperature, reaction rate feels a steep increase, enhancing oxidation and hydrogen production, as shown in Figure 4.6.

For Zircaloy-Oxygen reaction, K(T) has no transition temperature, and it is Arrhenius-type with constant coefficients [14]. In Figure 4.6 behavior of the default Zircaloy-Oxygen reaction rate is reported. MELCOR conservatively chooses the higher reaction rate if both steam and oxygen are present in oxidant flowing mixture.

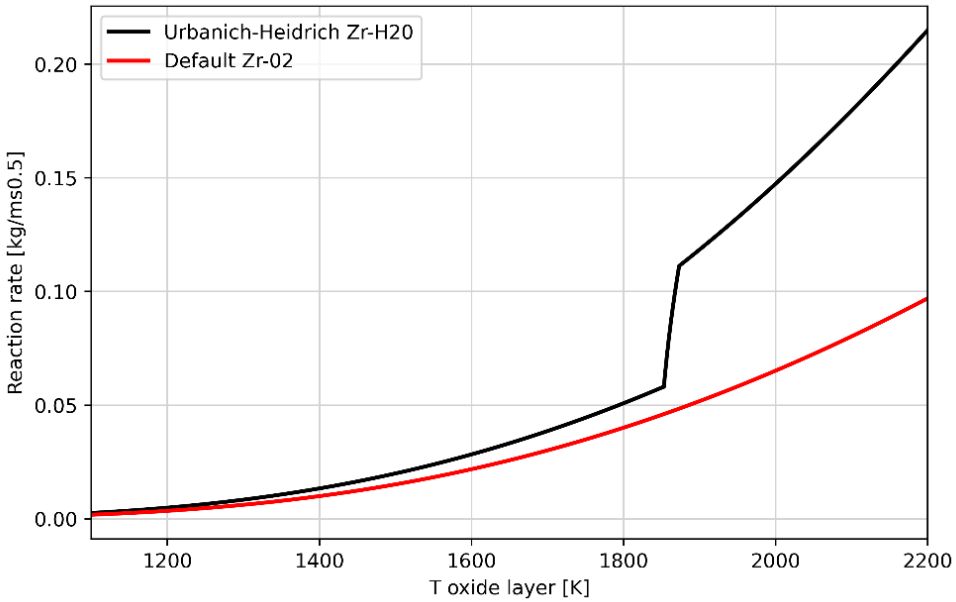

Figure 4.6: Default K(T) for Zircaloy Oxidation

In addition, MELCOR code is able to describe oxidation in presence of very low concentration of oxidants, in which the reaction rate is limited by gaseous diffusion.

Once the mass of metal β-Zr undergone transition to α-Zr(O) and zirconia is evaluated, evolution of oxide layer is calculated as follows:

$$\delta = r_0 - r = \frac{w}{\rho} \tag{4.12}$$

$$\frac{d\delta}{dt} = \frac{K(T)}{2\rho^2\delta} \tag{4.13}$$

where δ is oxide layer thickness and ρ is zircaloy density. By focusing on the Zr mass m that has reacted per unit length of oxide layer, (4.14) and (4.15) become:

$$m = \pi\rho(2r_0\delta - \delta^2) \tag{4.14}$$

$$\frac{dm_{Zry}}{dt} = \frac{\pi K(T)}{\rho}\left(\frac{r_0}{\delta} - 1\right) \tag{4.15}$$

that releases linear power q [MW/m] equal to:

$$q = 6.53\frac{dm}{dt} \tag{4.16}$$

In actual prototypical configuration, zircaloy corrosion in steam and oxygen is characterized by a purely parabolic kinetics until *Break-away* occurs. Break-away is the detachment of embrittled oxide layer due to vibration and acting forces, exposing fresh unoxidized metal to the oxidant phase. This phenomenon, which establish a cyclic corrosion in which the overall trend is quasi linear (as presented in Figure 4.7), is strongly affected by the cladding temperature. Hot zircaloy surface, typical of accidental scenarios indeed, has break-away time significantly lower than in operational conditions (in which break-away may also not occur at all).

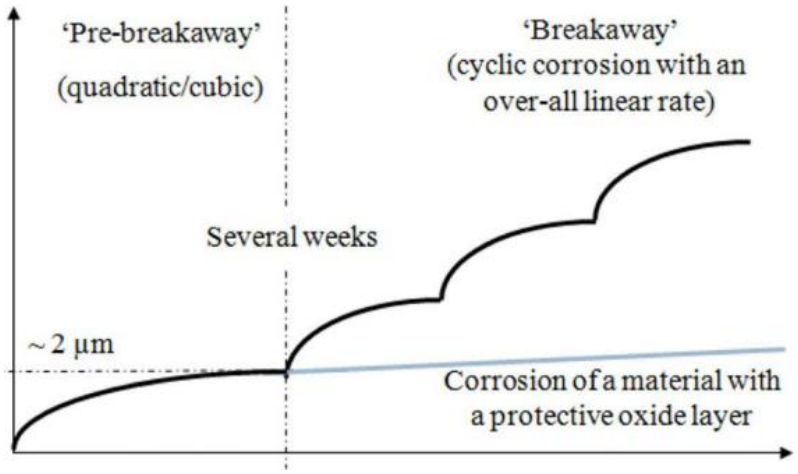

Figure 4.7: Zircaloy break-away [16]

MELCOR accounts for post-breakaway K(T) only for the Zr-O_2 reaction [13]. However, in the following versions of MELCOR, also steam cyclic corrosion parameters should be introduced [13].

A more qualitative description of zircaloy oxidation with steam is postponed in 5.4.7 for introducing the several correlations implemented in QUENCH-06 model.

4.4.2. Quench Front Velocity Model

Velocity of waterfront cooling core region during transients is greatly dependent from heat transfer parameter and cladding temperature. It is evaluated by means of Peclet number [14] (*Dua-Tien* correlation) as:

$$Pe = \frac{v\delta_S}{\alpha} = (\overline{Bi}(1 + 0.4\overline{Bi}))^{0.5} \tag{4.17}$$

where v is quench front velocity, δ surface thickness, α thermal diffusivity, and $\overline{Bi}$ Biot number of the wet portion of surface component in a cell. Biot number is described in (4.19):

$$\overline{Bi} = Bi\frac{(1-\Theta)^2}{\Theta} \tag{4.18}$$

where

$$Bi = \frac{HTC^*\delta_S}{k} \tag{4.19}$$

with k thermal conductivity, HTC* heat transfer coefficient associated with the quenched portion of component surface and Θ dimensionless temperature (equal to

one if the unquenched surface has a temperature equal to the maximum temperature (T_{super}) against which a quench front can progress [14]).

MELCOR parameter that may be modified through sensitivity coefficients are h* and T_{super} [13]. Default values implemented in the code are 150 kW/m^{2}K and 600 K respectively.

4.4.3. dT/dz Model

CVH nodalization is usually much coarser than COR nodalization. In order to achieve a fine temperature and mass fraction distribution for the detailed evaluation of convection and mass transfer between component and channel in each core-lower plenum cell, MELCOR is equipped with dT/dz Model. First COR cell (in flow direction) of the axial stack that is linked with a single control volume assumes as **inlet temperature** the temperature of the atmosphere entering the control volume. Then, channel temperature of the successive COR cells is obtained through a simple energy and mass balance. dT/dz Model provides also MELCOR simulation to gain superior capability of predicting energy transfer in presence of little or no flow [14].

Adoption of this model requires that the heat structures that radially bound COR region communicate with fluid temperature evaluated by dT/dz itself. This feature is selected by turning on the card *HS_L/RBF* and specifying the outermost ring cell in HS package.

4.4.4. Calculation Framework

COR package adopts an **explicit numerical scheme** [14] for advancing thermal state of core structure in time, with a sub-cycling capability to reduce numerical instabilities. Energy generation, heat transfer rate and oxidation rate are determined at the start of cycle based on the current components temperature and geometry condition. Net energy income for each component is obtained by multiplying these rates by the executive timestep. Then, at the end of cycle thermal state is updated and core degradation models calculate core material relocation and eventual debris formation.

4.5. Material Properties and Non-Condensable Gas Packages

Material Properties unit lists thermo-mechanical properties of the solid (or handled as solid) material used by other packages and enthalpy tables for the electric heaters that could be included into the COR description. MP has some default species which

characteristics are already present in MELCOR, taken from NIST JANAF database [17], like UO_2, Zircaloy, Steels, FeCrAl, aluminum oxide, boron carbide, graphite, and concrete. Users are allowed to define new material. Properties compulsory to be inserted as CFs or TFs are :

- Density vs temperature
- Enthalpy vs temperature
- Thermal conductivity

Additional features that may be specified are melting point, volumetric dilatation coefficient and molecular weight.

Non-Condensable Gas package contains information about the flowing species. As stated before, each fluid phase must be labelled with a sequential number relative to the species available in the library. Gasses are modeled as ideal gases and are characterized by molecular weight, energy of formation, and specific heat capacity expressed in terms of polynomial function of temperature. As for solid material, gases may also be user-specified.

4.6. Control Function Package

Control Function (CF) package allows MELCOR user to build function of variable available in MELCOR database and submit them to other packages. Differently from TFs, which are pure mathematical function (hence stated a priori) [13], values of each CF are themselves variable in the database. It means that they are calculated at start-of-timestep by taking into account the current value of the variable they are describing, and during the sub-cycling they may change.

They are mainly used as utility for several possible applications [13], as the definitions of:

- Rate of mass or enthalpy in CVH sources;
- Velocity of phases in FL;
- Fission, or decay, power;
- Logical function for failure criteria, valve openings, temperature and pressure control, and safety items operations.

4.7. Sensitivity Coefficients

MELCOR subroutines are closed and not available to be changed by independent users. However, the tool guarantees great flexibility in modeling since a great number of **Sensibility Coefficients** (SC) may be tuned to customize numerical

resolution schemes, embedded correlations, or failure limits. Furthermore, uncertainty analysis can be conducted by running several MELCOR calculations, each one with different sampled SCs.

In Table 4.1, a list of additional packages not used in this thesis work is presented, with a brief description.

Package	Objective
Accumulator (ACC)	Stable and improved modeling of accumulators and engineered safety features
Burn (BUR)	Modeling gas combustion in control volume
Cavity (CAV)	Description of melted core concrete interaction, including effects of ablation, gas generation and direct containment heating.
Decay Heat (DCH)	Evaluation of decay heat power resulting from decay of fission products, both in core material and in suspended or deposited aerosols.
Executive (EXEC)	Responsible for the overall executive control of the simulation.
Radionuclide (RN)	Modeling of the behavior of fission products aerosols, vapors, and traces, including release and condensation-evaporation phenomena.

Table 4.1: MELCOR packages

4.8. MELCOR Code Validation

As already described in Section 2.3.3, verification and in-house validation of physical models encoded into the analytical tools are necessary to provide developers indications on how algorithms, numerical methods and models may be improved [15].The independent validation campaign made by the users is aimed to check if the code is actually able to represent an extensive range of target phenomenologies against several test facilities. Additionally, beginners may gain new skill and better insight of the code by validating it in respect of challenging experiments.

MELCOR code, in particular, has been validated in respect of several datasets, obtained on the basis of analytical results, code-to-code comparison, from TMI and Fukushima SA accidents and experimental tests (basic, separate, and integral effects). Main test contributors to MELCOR validation campaign are *USNRC*, *Electric Power Research Institute* (EPRI), *Department of Energy* (DOE) and *OECD* though the International Standard Problems [15].

SNL suggests that inputs describing test facilities should adopt default settings for main parameters, in order to perform a "frozen" assessment of the implemented tool without an excessive tailoring of the simulation. However, experimental set-ups are usually characterized by non-prototypical geometries, and hence users are allowed to modify settings for code validation, as long as sensitivity analyses are conducted followed by reasonable justifications and documentation.

More than 50 validation sources have been proposed for MELCOR Assessment. These tests cover multiple phenomenologies and physics processes, like heat up and heat transfer (in- vessel and ex-vessel), material oxidation, core degradation, molten pool downward progression, fast cool down by reflooding, critical heat flux and thermal crises, hydrogen production and detonation, core-cavity interaction, FP release, aerosol deposition and more.

An outline of MELCOR validation tests is depicted in Figure 4.8.

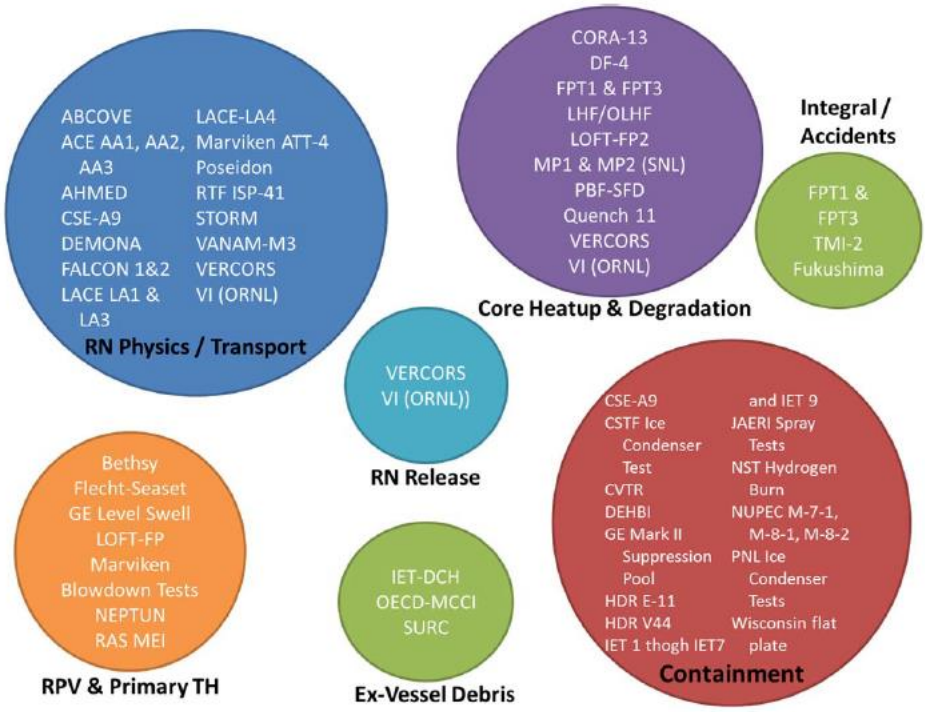

Figure 4.8: MELCOR Validation Tests [15]

Next validation campaign will be devoted to check the accuracy of results of model of point kinetics, lower head penetration, flashing, stratified countercurrent flows and the template for High Temperature Gas Reactor. In conclusion, MELCOR package that currently are not undergone any assessment of the response are **Condenser P.** (CND), **Fan Cooler P.** (FCL) and **Passive Autocatalytic Recombiners P.** (PAR) [15].

In the next chapter QUENCH-06 input will be described in terms of nodalization, models and correlations adopted. Results and comments about the validation of MELCOR code in respect of the above-mentioned test is postponed in Chapter 6.

5 QUENCH-06 MELCOR Input

This chapter will be devoted to presenting QUENCH-06 nodalization scheme for MELCOR v2.2 code. Development of the input has been carried out relying on the user interface *Symbolic Nuclear Analysis Package* (SNAP) [18]. for what concerns CVH, FL, MP, NCG and HS packages. COR package, instead, has been built through direct coding in ASCII file for gaining more flexibility given the non-nuclear geometry.

The following input contains the computational representation of the bundle region from **EL -476.58 mm to EL 1500.00 mm**, embracing lower and upper plenum. Radially it models **from radius 0 mm to** the inner cooling jacket outer surface at **radius 84.15 mm**. Additionally, it includes simplified descriptions of the fast water injection system and power supply. Water loops, superheater and gas tanks are embedded in this model only as boundary conditions. Hydrogen detection devices, thermocouples and other instruments are not taken into account in the current version of the input deck.

In the next sections each package structure will be outlined. Results of the simulation instead, are postponed to Chapter 6.

5.1. QUENCH-06 CVH-FL Modeling

The entire volume available for hydrodynamic material to cross the bundle is subdivided into 12 **test control volumes** (TCVs), from EL -474.20 mm to EL 1500.00 mm. For the complete representation of boundary conditions and package-to-package requirements, input is featured with 10 **additional control volumes** (ACVs), whose purposes will be described below.

5.1.1. Test Control Volumes

Test control volumes are initially filled with superheated steam, pressure being 2 bar and atmosphere temperature 600 K. Pool is not inserted but its presence is allowed since quench water will be flowing in the bundle after t = 7179.5 s. These

volumes are set to *active* in order to update their properties in time, and in *Non-Equilibrium*, ensuring just the pressure equilibrium between the two phases and not the thermal one. Total volume for each TCV is calculate by multiplying the coolant passage area (CPA, more or less constant up to 1300 mm where it enlarges in absence of thermal insulation) by the relative vertical span. Coolant passage area is expressed by the (5.1):

$$CPA = \begin{cases} \pi {r_{sh,in}}^2 - A_s & -474.20\,mm < z < 1300.00\,mm \\ \pi {r_{cj,in}}^2 - A_s & z > 1300.00\,mm \end{cases} \quad 5.1$$

with $r_{sh,in}$ being zircaloy shroud internal radius, $r_{cj,in}$ inner cooling jacket internal radius and A_s sum of all solid structures (FRSs, Corner rods, central rods mainly) base areas at the given altitude. It is important to clarify that TCVs located in an altitude where is placed a supporting grid will have a slight reduced volume.

Lower plenum TCV is defined as *CVH_01*. It embraces the available volume in correspondence of copper electrode, from EL -474.20 mm to -300.00 mm. Being the lowest volume, it contains the sources of argon, steam and liquid water that will pass though the test section in upward direction. Table 5.1 provides a schematic description of material sources specified in CVH_01. All the CVH sources of the QUENCH-06 model are inserted by the users through TF and CF packages.

CVH_01 Sources		Avg. Value	Time Interval
Steam	Mass flow rate	~ 3 g/s	[0 s, 7179.5 s]
	Temperature	640 K	[0 s, 7179.5 s]
Argon	Mass flow rate	~ 3 g/s	[0 s, 7179.5 s]
	Temperature	640 K	[0 s, 7179.5 s]
Quench Water	Mass flow rate	~ 42 g/s	[7215 s, 7468 s]
	Temperature	397 K	[7215 s, 7468 s]

Table 5.1: CVH_01 sources

Right above -300.00 mm, *CVH_02* extends up to 0 mm encasing all hydrodynamic volume relative to the lower molybdenum electrode.

Active region of the bundle (i.e., where centerline of the FRSs is occupied by tungsten wire) spans from 0 mm to 1024.00 mm. Since in this region flowing mixture significantly removes power from the structure, and it is affected by steep axial temperature gradient, it has been sub-divided into 8 equal TCVs (each one of vertical dimension equal to 128.00 mm), namely *CVH_31* so on until *CVH_38*.

Region in correspondence of molybdenum upper electrode is described by 2 different TCVs. *CVH_04* covers from 1024.00 mm and 1300.00 mm, where the bundle is still encapsulated by thermal insulation system, even if ZrO_2 fiber has been substituted by stagnant dissipating argon. *CVH_05*, which is located above CVH_04 and it extends up to 1500.00 mm representing the upper plenum, is the largest of all test control volumes, given that flowing mixture at that elevation is radially bounded directly by the water-cooled inner cooling jacket. CVH_05 has an argon source, which characteristics are reported in Table 5.2, accounting for the argon mass flow rate that is switched to bundle head after fast pre-injection.

CVH_05 Source		Avg. Value	Time Interval
Argon	Mass flow rate	~ 3 g/s	[7179.5 s, 9000 s]
	Temperature	298 K	[7179.5 s, 9000 s]

Table 5.2: CVH_05 source

In Table 5.3 below a brief summary of test control volumes is depicted.

TCV	Elevation	Volume
CVH_01	EL -474.20 mm to EL -300 mm	5.3653E-4 m^3
CVH_02*	EL -300 mm to EL 0 mm	8.9141E-4 m^3
CVH_31*	EL 0 mm to EL 128 mm	3.72992E-4 m^3
CVH_32	EL 128 mm to EL 256 mm	3.84952E-4 m^3
CVH_33	EL 256 mm to EL 384 mm	3.84952E-4 m^3
CVH_34	EL 384 mm to EL 512 mm	3.84952E-4 m^3
CVH_35*	EL 512 mm to EL 640 mm	3.72992E-4 m^3

CVH_36	EL 640 mm to EL 768 mm	3.84952E-4 m^3
CVH_37	EL 768 mm to EL 896 mm	3.84952E-4 m^3
CVH_38	EL 896 mm to EL 1024 mm	3.84952E-4 m^3
CVH_04*	EL 1024 mm to EL 1300 mm	8.18093E-4 m^3
CVH_05*	EL 1300 mm to EL 1500 mm	3.520459E-3 m^3

* volume is reduced for the presence of a grid spacer

Table 5.3: Test Control Volumes

The twelve flow paths connecting pairs of control volumes are featured by the following properties:

- The two junctions are located at the same elevation to represent the open interface between two TCVs
- Length of each FL is specified as the height of the *from* control volume. The only exception is **Flow-Path_45** that links CVH_04 to CVH_05, in which two segments are defined, both referring to the heights of *from* and *to* TCVs. In the case a supporting grid is present in the *from* control volume, length of the FL is reduced by a factor equal to grid thickness.
- $D_{hy} = 0.0161123\ m$ as hydraulic diameter, $CPA = 0.0030074\ m^2$
- Second segment of Flow-Path_45 (i.e., describing flow motion and pressure drops in CVH_05) has $D_{hy} = 0.0551900\ m$ as hydraulic diameter, and $CPA = 0.0176900\ m^2$
- Absence of flow paths form coefficients, since in KIT deployed data no information about concentrated pressure drops is reported.

5.1.2. Additional Test Volumes

CVH Input is completed by an additional set of control volumes aimed to model fast injection system, off-gas pipe, containment environment and to fulfill MELCOR inter-packages requirements.

Tank_out is a Non-Equilibrium ACV devoted to representing off-gas collector. It is placed above 1500.00 mm, and the volume, which is set to Constant in time, is 1000 m^3. Due to the fact that Tank_out thermophysical properties do not change during the simulation, from its pressure (namely 2 bar) the code will reconstruct backward the pressure of all TCVs dependently on the results of (4.5) for each flow path.

Containment CV models test section case [Figure 3.1]. The only phase allowed to fill this ACV is atmosphere, composed just by Argon, at a constant temperature of 415 K and pressure 2 bar. It is not linked through any flow path to the test volumes, but it has been inserted to express external boundary conditions for the COR lower head and for the lower plenum heat structures.

Bundle_Inlet is a very small control volume located below CVH_01, from EL -476.58 mm to EL 474.20 mm. It has been submitted into the input to express COR lower plenum (encapsulated by flat lower head), but it actually does not represent any physical portion of QUENCH-06 facility.

Concerning water fast preinjection, it is not possible to include it as material source directly into CVH_01, because its pressure prior to valve opening is 6 bar, three times greater than system pressure. Additionally, MELCOR code does not permit to add a pressure source into control volume. Hence, in order to get the correct enthalpic content of fast preinjected water flow, *PreWater_tank* has been modeled. It consists of a 0.1 m^3, subcooled water filled (370 K, 6 bar), Constant control volume placed right below CVH_01. It is linked with CVH_01 though a flow path and a valve, whose parameters have been determined as results of a sensitivity analysis that ensures 4 l of subcooled water to enter the system in 5 s.

Between EL 1024.00 mm and 1300.00 mm, zirconia fiber sponge in the thermal insulation system is replaced by a volume filled with stagnant argon, modeled in MELCOR by means of *Argon_Ins* ACV. This volume contains only argon for the whole transient, at a pressure being around 2 bar. It is allowed to evolve in time since it acts also as bypass for COR Shroud component, and moreover it establishes convection with the inner cooling jacket placed at the same elevation.

Bypass_1 to *Bypass_5* are five active, dummy control volumes spanning from EL -474.20 mm to EL 1024 mm. They are modeled with the purpose of representing a 0.5 mm argon filled annulus between the lower plenum diffuser cage or zircaloy shroud outer surface and the zirconia fiber layer. They have been inserted following the QUENCH-11 description in MELCOR developed in [19]. Their presence is mandatory since the Shroud component in COR package requires bypass volumes with which exchange power. In bypass network it is not permitted the water to flow. It is worth specifying that, even if the presence of these bypasses is a distortion of the actual thermal insulation system, simulation results are not affected at all since annulus is exceptionally thin, and there are no flow paths linking each bypass volume. The choice not to link ACVs with FLs is supported by the fact that in this way power is not removed by COR Shroud though convection, but heat is just conducted across steady argon towards the zirconia fiber sponge. In Figure 5.1 a complete description of CVH package of QUENCH-06 MELCOR model is shown.

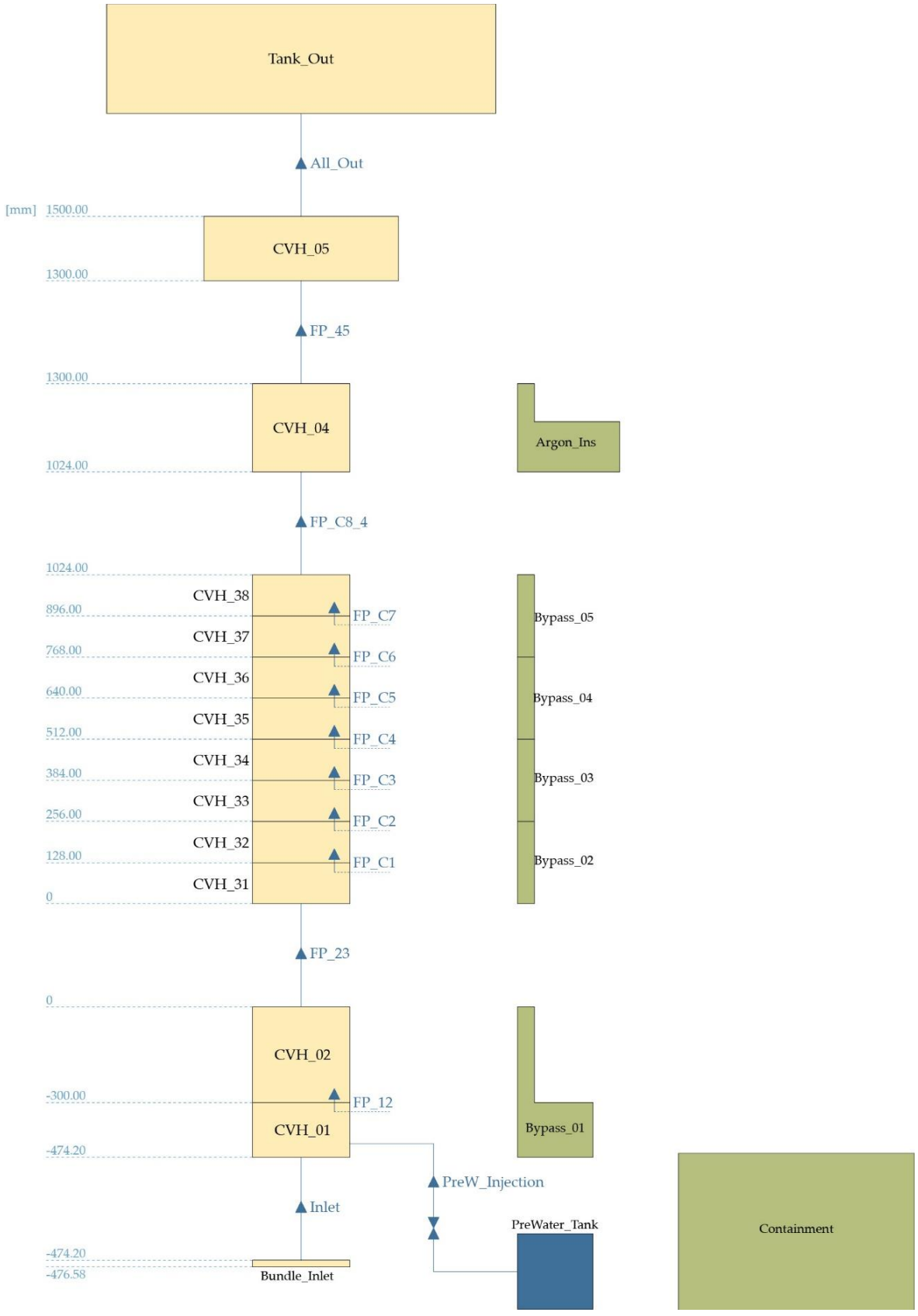

Figure 5.1: CVH-FL model

In Table 5.4 an outline of Bypass control volumes is presented.

ACV	Volume	Elevation
Bypass_1	4.75922E-4 m^3	EL -474.20 mm to EL 0 mm
Bypass_2	3.42851E-5 m^3	EL 0 mm to EL 256 mm
Bypass_3	3.42851E-5 m^3	EL 256 mm to EL 512 mm
Bypass_4	3.42851E-5 m^3	EL 512 mm to EL 768 mm
Bypass_5	3.42851E-5 m^3	EL 768 mm to EL 1024 mm

Table 5.4: Bypass ACVs

In order to reduce any potential numerical error arising from the failure in convergence in the solution of CVH equations (in sparse form), **SC4415(2)** (Convergence criteria for the iterative solver) and **SC4415(3)** (Maximum number of iterations permitted for the iterative solver) are increased to 1.0E-5 and 1000.0.

5.2. QUENCH-06 NCG Modeling

Thanks to Non-Condensable Gas package, QUENCH-06 flowing species are defined. By default, MELCOR requires the presence of subcooled **water** (Pool), water **droplets** in suspension (Fog) and **steam** (H2O-Vap). **Argon** gas can be inserted by submit the command *AR* in gas code library.

Since QUENCH-06 model accounts for material oxidation and mass transfer between flowing mixture and stainless-steel structures, COR package forces the user to include in the available species also **hydrogen**, **oxygen**, **carbon monoxide**, **carbon dioxide** and **methane**.

5.3. QUENCH-06 MP Modeling

Material Properties package contains all thermo-mechanical data about the solid material exploited in COR and HS packages.

Concerning materials adopted in the thermal insulation system**, stainless-steel** for the cooling jacket is the only one already embedded in MELCOR. **Zirconia Fiber Sponge** properties are specified following the indication deployed by KIT in [20],

where density is just a fraction of the theoretical density of ZrO_2 (to model its porous matrix), while melting point is kept 2867 K. Also, thermal conductivity and specific heat of zirconia are modified to account for the different matrix of the sponge. For the expansion compensator located at 1250.00 mm, since no specifics are defined in reports, it has been chosen **ASTM A240 TP 321 Stainless Steel** [21], **whose properties are taken from** [22]**.** Density of ASTM steel is set by the user equal to 30% of its actual density to account for its spring geometry. By doing so, once ASTM steel is placed into HS mesh, the heat conducted through it will be lowered than if it was full solid.

QUENCH-06 COR package embodies **zircaloy** and **zirconia** that are embedded in MELCOR library. **Molybdenum** and **copper** electrodes, and the **tungsten** heater as well, are characterized by properties inserted by the user according to NIST thermochemical tables [17]. **Aluminum oxide** has been specified too as solid material for upper plate heat structure. In addition, in order to predict the oxidation of stainless-steel, also **stainless-steel oxide** is included in QUENCH-06 material set. COR package obliges the definition in MP of uranium dioxide, carbon steel, stainless-steel 304 and silver-indium-cadmium, but they will not be exploited in the model.

5.4. QUENCH-06 COR Modeling

Through COR package fuel rod simulators, unheated central rod, corner rods, zircaloy shroud and grid spacers have been modelled.

QUENCH-06 COR structure is a PWR-like core, in which the card *ELHEAT* has been turned on to account for the presence of electric heaters substituting uranium dioxide as the main power source. Test bundle is divided into *4 concentric rings* and *42 axial levels*, for a total of 168 cells. Each cell contains geometry data (including local hydraulic diameter and surface areas) of several solid structures (zircaloy cladding, zirconia, heater) representing the actual material composition and layout of QUENCH items at the given **altitude-radial position**. In addition, channel areas are specified into the cells to allow fluid motion and to evaluate heat and mass transfer within it.

In the following two sections, radial and axial subdivisions of test bundle are presented in detail.

5.4.1. Rings

Facility from radius 0 mm to radius 42.38 mm is subdivided in 4 rings. Coolant passage area is divided among the four annuli on the basis of ratio *ring area-total QUENCH-06 base area.*

Ring #1 contains the unheated fuel rod. Central rod cladding is specified as **Zircaloy Cladding** and the zirconia pellet as **Supporting ZrO_2.**

In Ring #2 the eight inner fuel rods simulators are represented by means of an *equivalent FRS* with total mass and total surface area. This ring contains zircaloy cladding, supporting zirconia annular pellets, supporting zircaloy and stainless-steel for spacers and the electric heater. Molybdenum and copper electrodes are defined respectively as *ELM1* and *ELM2,* while the Tungsten wire as *MATHT.*

Ring #3 represents the radial portion of the bundle occupied by the twelve outer FRSs. Its composition is almost equal by the one of Ring #2, except that the items surface area and stored masses are higher in the third ring.

The outermost ring (namely Ring #4) describes the periphery of the chamber, including four zircaloy corner rods, instrumentation tubes and shroud. Corner rods are modeled in MELCOR as a single Zircaloy Cladding with a mass equal to the sum of the four corner rods and instrumentation tubes masses. Inside the cladding no items are inserted. By representing corner rods as solid cladding, MELCOR evaluates their oxidation and relative hydrogen production, which it would not be considered in the case of their description as Zircaloy Non-supporting structures. As concerns the zircaloy shroud, MELCOR provides, and suggests, the SH components, available for modeling core barrel in PWR. Adoption of **SH component** forces the user to specify on the right surface at least a bypass boundary control volume. Thus, QUENCH-06 shroud in MELCOR will by bounded on the right by Bypass ACVs at the different elevations.

Al_2O_3 plate is defined as the upper boundary heat structure with which all rings may transfer power.

In Figure 5.2 and Table 5.5 outline of the rings, with their dimension, is presented.

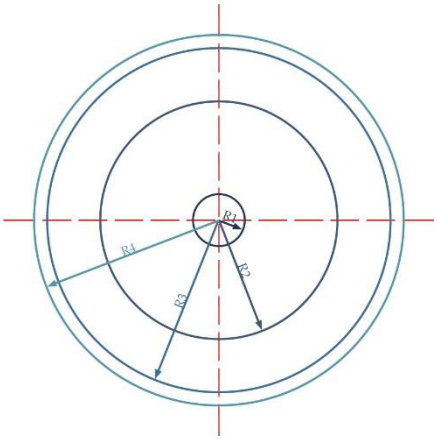

Figure 5.2: COR rings

Ring	Radius
Ring #1	6 mm
Ring #2	27.975 mm
Ring #3	39 mm
Ring #4	42.38 mm

Table 5.5: Ring radii

5.4.2. Axial Levels

Test bundle is axially sliced into 42 levels from EL -476.58 mm to EL 1500.00 mm. All the cells on a single axial level must be coupled with a control volume located at the same altitude. The additional specification of a bypass control volume is usually not required, with exception of levels in the outermost ring in presence of shroud or canisters.

Axial level (AL) #1 contains the MELCOR lower plenum mentioned in Section 5.1.2. It is important to notice **that it is not the actual lower plenum** (i.e., QUENCH-06 region between -474.20 mm and -300.00 mm) but just core portion encapsulated by COR lower head, which it is completely dummy since it is not possible to identify it in the test section geometry. This first axial level does not contain any structure, it is coupled with the Bundle_Inlet (treated as lower plenum) control volume and it extends from EL -476.58 mm to EL -474.20 mm. The *flat* Lower head (LH) is located at EL -476.58 mm. It is radially divided into 4 concentric rings, matching the radial structure of the COR, and has a thickness equal to shroud thickness (2.38 mm), which is further subdivided in 6 vertically stacked segments. On the outer surface, lower head transfers energy with Containment. Planar junction between LH and SH is located at EL -474.20 mm.

Above AL #1, second Axial Level (AL #2) is occupied by the core supporting plate, made of stainless-steel. This structure carries the weight of all COR components. Spanning from EL -472.20 mm to EL -470 mm, it is linked with CVH_01.

AL #3 and AL #4 embraces axial portions of solid items in correspondence of lower copper electrode. These levels are of identical length 85 mm, extending up to EL -

300 mm and therefore representing the actual bundle lower plenum, reported in Figure 3.6. AL #3 and AL #4 are still linked with CVH_01.

Structure between EL -300 mm and 0 mm, matching lower molybdenum electrode, are sub-divided in 5 levels of 60 mm length each. AL #6 contains the Inconel grid, but it is modeled as stainless-steel supporting structure, since Inconel can be inserted just as cladding. Control volume coupled with AL #5 to AL #9 is CVH_02.

Active region is described by means of 24 axial levels to increase accuracy where oxidation, hydrogen production and heat up are the most significant. Each axial slice covers 42.667 mm in elevation, and hence every control volume from EL 0 mm to EL 1024 mm interacts with a triplet of COR levels. In AL #11 and AL #22 two zircaloy spacer grids are placed.

AL #34 to AL #38 contain portion of items located in correspondence of CVH_04, between end point of the active region and the upper plenum. AL #34 is featured with the third zircaloy grid. AL #38 is the highest level in which SH component in Ring #4 is present. Each axial levels covers a vertical span of 55.2 mm.

The last four axial levels (50 mm single height) contain the solid structures in the upper plenum, where the flowing mixture exchanges heat directly with the cooling jacket without any additional thermal insulation layer. The actual coolant passage area in this region is significantly enlarged, but COR radii are not modified. However, this change in layout lies in an increased channel flow area and hydraulic diameter of Ring #4, now filled just by corner rod components. Last zircaloy grid is located in AL #41.

Initial temperature for all components in the COR package is set accordingly to experimental data deployed by KIT.

In Figure 5.3 COR nodalization of bundle region is shown

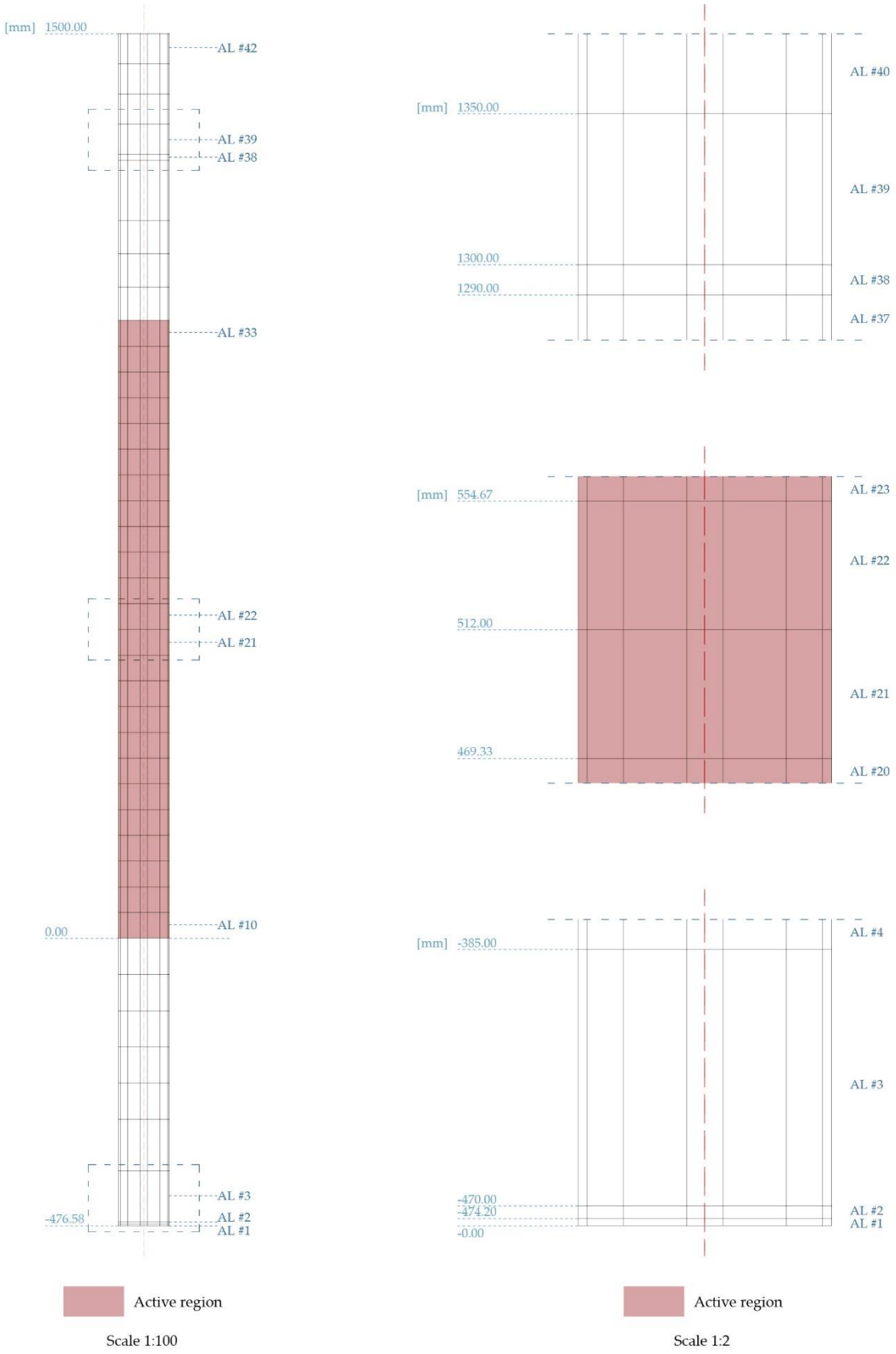

Figure 5.3: COR axial nodalization

5.4.3. Supporting Structure Definition

Card *COR_SS* is provided by MELCOR for overwriting and inserting additional data about supporting structures material and characteristics. Core supporting plate (AL #2) and the bottom grid (AL #6) are made of stainless steel and specified as PLATEG. PLATEG [13] represents part of a grid-supported plate that initially supports fuel rods and eventually particulate debris above it. Its failure (failure criteria will be reported in Section 5.4.4) implies that it loses the capability of carrying the above structures weight (including debris), but the plate itself does not collapse nor relocate below. As concerns the remaining four grids, they are set as PLATEG too but made of Zircaloy.

Zirconia pellet stack (with stack also electrode ZrO_2 coating will be considered) are not included in COR_SS because no built-in option is fully able to describe their specific geometry and composition. However, correct mass of ZrO_2 supporting structure is inserted in each cell.

5.4.4. COR Failure Criteria

Lower Head fails when the differential pressure between lower plenum (*Bundle_Inlet*) and cavity (*Containment*) exceeds 200 bar. Given the rather low system pressure, power supplied and inlet flow rates, and the fact that during heat up transient the bottom region is characterized by the lowest temperature in the bundle, LH failure and ex-vessel material relocation is expected not to occur in QUENCH-06 simulation.

Core supporting plate and the five grids are allowed to fail if local cell temperature becomes higher than 2400 K. Zircaloy grids sustain weight until the thickness of unoxidized metal is larger than 10 μm. This value is imposed very low by the user because in the experimental set up these grids are not actually devoted to support any structure, but they acts only against rod bending preventing contact. Hence, in order to not provide biased results due to the failure of these spacers, that would imply a complete loss of the initial geometry following material relocation, the occurrence of grid collapse is almost completely prevented in this way. Critical thickness for stainless-steel components is not provided.

As concern fuel rod failure criteria, they may be modified by means of sensitivity coefficients, in particular COR1131 (Molten Material Holdup Parameter) and COR1132 (Core Component Failure Parameters), to account for the different material composition of FRSs in QUENCH facility. Temperature to which oxidized fuel rods can stand in the absence of unoxidized Zr in the cladding is shifted from 2500 K to 2990 K, which is zirconia melting temperature. This variation is

introduced to avoid occurrence in the simulation of major failures, relocation and candling of components that had proven experimentally resistance to such challenging conditions Furthermore, fuel rod critical temperature, at which it will collapse no matter material state or composition, is no longer 3100 K, uranium dioxide melting temperature, but 3695 K, tungsten melting temperature.

Shroud failure default settings are maintained in the model. It should be noted that material relocating after shroud failure is directed towards bypass region, not the channel.

5.4.5. Power Supply

Supplied power (which trend is shown in Section 3.4) should be reduced by a factor accounting for the external wire resistance and sliding contact. In *COR_ELPOW* card, it is possible to insert power and tension at the clamps for each ring, with *CORNRES* parameter that represents the out-of-bundle resistance. CORNRES has been set ~0.52 mΩ/ring for the preoxidation phase, and then slightly reduced during power ramping. Power generated by Joule effect in electric materials is calculated by the code applying default correlations of resistivity function of temperature [13].

In Figure 5.4 effect of the wire resistance on the power is reported.

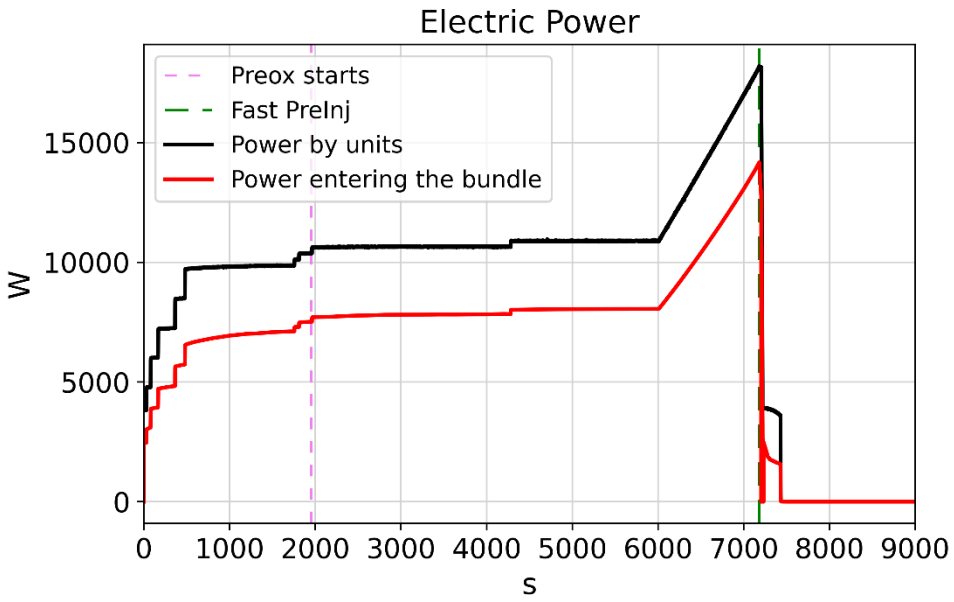

Figure 5.4: Electric Power

Due to the nature of the experimental test, fission power and decay heat cards are not turned on for this computational input.

5.4.6. COR Additional Models and Parameters

COR dT/dz Model with default parameters has been adopted to gain more accuracy in the axial temperature distribution.

Radial radiative exchange factors (*FCELR*) for thermal radiation among COR cells has been updated to better describe energy transfer across gray flowing mixture from FRSs to zircaloy shroud. Default value of MELCOR v2.2 equal to 0.1 has been set equal to *1.0* in QUENCH-06 model.

Candling Model (*COR_CHT, COR_CMT*) is activated and default parameters [13] for molten pool heat transfer and material transport are kept in the simulation.

5.4.7. Zr oxidization correlations implemented in QUENCH-06 Model

The general analytical description of zircaloy oxidation reaction has been reported in Setion 4.4.1. In this paragraph, a more qualitative overview of the various modifications occurring in the crystalline structure of zircaloy is presented, in order to provide sufficient basis for the following overview of the Zircaloy-Steam reaction rate correlations adopted in QUENCH-06 model.

Phase diagram of zirconium with different percentage of oxygen in its crystalline structure is shown in Figure 5.5.

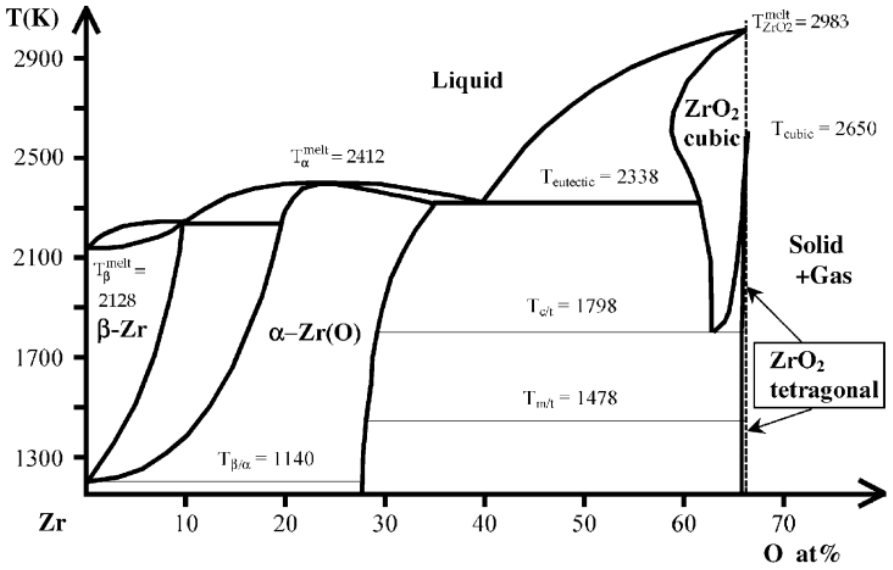

Figure 5.5: Zirconium-Oxygen phase diagram [23]

At temperatures above the $(\beta+\alpha)/\beta$ allotropic transition for zirconium alloys, steam reacts with the metal to form a superficial oxide layer of zirconia (ZrO_2) and an intermediate layer of oxygen stabilized α-Zr(O), process being mediated by oxygen

diffusion in solid state [24]. It has been experimentally proved that up to 1800 K growth kinetics of both layers is parabolic, and it is well described by means of Arrhenius-type reaction rate function of surface temperature. At temperature larger than 1900 K a discontinuity in the velocity of oxide scale growth has been noticed. Urbanich and Heidrich [24] in 1977 motivated the variation in the process kinetics as due to the allotropic transition of superficial zirconia from tetragonal to cubic (duplex oxide), characterized by higher oxygen diffusion coefficient. Concurrently, also oxidation of the oxygen-stabilized α-phase is triggered, causing a steep increase in corrosion and subsequently in hydrogen production. However, given the complexity of the phenomenology, parabolic description of oxidation over 1900 K is kept in SA tools, but with enhanced reaction rates.

It should be added that Zircaloy-4, adopted in PWR core, has been designed to be less resistance to corrosion in respect of Zircaloy-2 (BWR), since primary circuit environment is reducing. Its composition is indeed lacking Nickel to avoid or limit the effect of hydrogen diffusion (due to hydrogen overpressure necessary to keep limited water radiolysis) that would create hydrides and voids embrittling the cladding itself.

The following is a brief description and representation (Figure 5.6) of the different parabolic correlation that will be tested in QUENCH-06 MELCOR model. To be more consistent with latest tests and considerations [23], the two transition temperatures, mentioned in Chapter 4.4.1, are set equal to 1800 K and 1900 K.

5.4.7.1. Urbanich-Heidrich Correlation

Urbanich-Heidrich formalism is by default adopted in MELCOR calculations.

Urbanich-Heidrich provides two correlations [24], covering both low temperature and high temperature regimes. Formulation has been developed by conducting two different experiments: *Hydrogen Evolution Method*, in which electrically heated zircaloy specimens are exposed to steam and hydrogen evolution rate is measured, and *Weight Gain Method*, in which it has been directly evaluated the mass of zirconia consumed though stoichiometric evaluation. However, recent studies [23] suggest that hydrogen evolution method layout provides biased results due to the occurrence of hydrogen blanketing effect. Hydrogen blanketing (alternatively Steam Starvation, which is more or less the same phenomenon) is the establishment of a thin layer of gaseous phase surrounding the item undergoing oxidation, which consequences are significative in high temperature range, limiting dramatically steam transport and supply to the surface. Hence, analysts currently consider *Urbanich-Heidrich* correlation to underestimate corrosion kinetics above 1800 K [23].

In addition, several studies conducted through computational tools report little overestimation of results for T < 1800K.

5.4.7.2. Baker-Just Correlation

Baker correlation [24] delivers single expression for K(T) valid for the overall temperature domain. Its formulation is obtained thanks to a large number of observations on electrically heated zirconium wires in water pools. The extent of the reaction is determined by hydrogen evolution method. This correlation is in general agreement with the *Urbanich* in low-T range, then it predicts faster reaction and thicker layers for T > 1900 K.

In the simulation exploiting this formulation, the two transition temperature are set equal to keep the purely exponential trend of the reaction rate.

5.4.7.3. Cathcart-Pawel Correlation and Leistikow-Schanz Correlations

Cathcart-Pawel and *Leistikow-Schanz* correlations are devoted to describing parabolic reaction rate behavior for Zircaloy-4 cladding with surface temperature lower than 1800 K. *Leistikow* et al. [23] experimental set up consists in short pipes exposed to flowing steam in tubular furnace, and the detection procedure is carried out by weight gain method. *Cathcart* and *Pawel* test evaluates oxidation kinetics of specimens heated in flowing steam environment through metallographic analysis of ZrO_2, α-Zr(O) and oxygen uptakes measurements.

5.4.7.4. Prater-Courtright Correlation

Formulation of *Prater* et al. covers the high temperature region, above 1900 K. Experiment is performed by heating one side of a disk specimen in contact with steam through CO_2 laser beam, and monitoring hydrogen production rate [23]. It is nowadays considered as the *best estimate correlation* since it is able to describe very harsh condition, and it accounts for metal with duplex oxide layers too. However, it is characterized by uncertainties, mainly due to the thermal gradient across zircaloy surfaces and to the fast detection system [23].

5.4.7.5. Volchek-Schanz Correlation

Volchek et al. approach evaluates a best-fitted parabolic rate for a wide group of experimental data above 1900 K [25]. Actually, *Volchek* work provides K(T) also for mid-range temperature (1800 K < T < 1900 K) but not in Arrhenius formulation. Hence, since it is not possible to implement in MELCOR such a rate, and due to the fact that between the two transition temperature code linearly interpolates boundary values of the low-T correlation and high-T correlation, formulation

covering this temperature interval has been discarded. Lower value of high temperature regime *Volchek* reaction rate may be explained by the fact that it takes into account for the fitting procedure also outcome of experiment in which the hydrogen blanketing occurs and it is measured effectively.

QUENCH-06 model is tested with 6 different K(T), as reported in Table 5.6. The overall trend of each K(T) implemented in the simulation is shown in Figure 5.6.

Simulation	T: [1100 K-1800 K]	T > 1900 K
1. Reference	Urbanich-Heidrich	
2. Baker	Baker-Just	
3. L-V	Leistikow-Schanz	Volchek-Schanz
4. CP-V	Cathcart-Pawel	Volchek-Schanz
5. L-Pr	Leistikow-Schanz	Prater-Courtright
6. CP-Pr	Cathcart-Pawel	Prater-Courtright

Table 5.6: QUENCH-06 Correlations

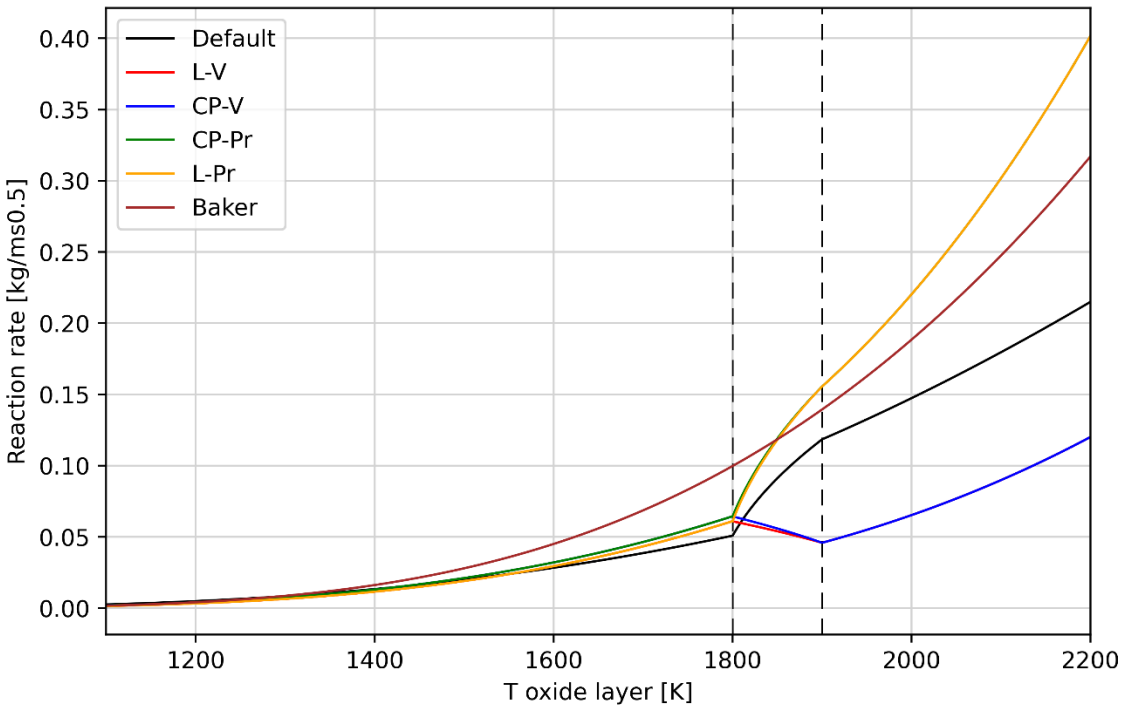

Figure 5.6: K(T) trends in QUENCH-06

The multiple reaction rates may be specified in MELCOR via sensitivity coefficients C1001 (Zircaloy Oxidation Rate Constant Coefficient). However, it is worth specifying that code requires manual input of $K^2(T)$. Therefore, reaction rate squared is interpolated between the two transition temperature.

As concern Zircaloy-Oxygen reaction, default parameters are kept, as shown in Figure 4.6. Oxidation cut-off temperature is maintained at 1100 K.

5.5. QUENCH-06 HS Modeling

QUENCH-06 MELCOR input is featured with 43 heat structures that model thermal insulation system (ZrO_2 fiber layer and the inner cooling jacket), inlet section steel walls, Al_2O_3 upper plate and the expansion compensator. HS #1 to HS #42 subdivision matches the axial nodalization of COR package.

On the right surface of each HS are specified the boundary conditions for the computational model of QUENCH-06. As requested by COR dT/dz Model, on the left surface of each HS card HS_LBF (Left Boundary Fluid Temperature Option) is activated. If convective condition is imposed on a HS, characteristic length for heat transfer and surface area are specified.

Between EL -476.58 mm to EL -300 mm, test section inlet plenum steel walls are modeled with 4 single layer heat structures. Left surface exchange heat through convection with CVH_01, while the right surface does the same but with Containment control volume.

Heat structures (HS #5 to HS #33) surrounding test section from EL -300 mm to EL 1024 mm consist of two meshes:

1. Inner layer of ZrO_2 fiber, on which left surface convection with the Bypass control volume located at the same elevation is activated.
2. Outer layer of SS for representing portion of cooling jacket. CF temperature of the right surface is imposed for the whole transient.

Figure 5.7 reports an example of active region heat structure.

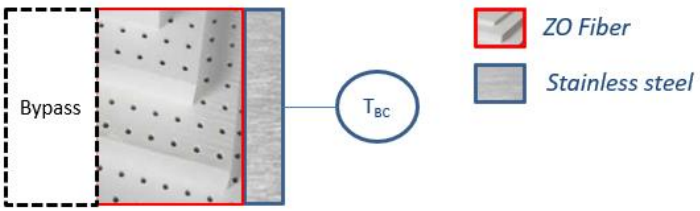

Figure 5.7: HS example 1

HS #34 to HS #36 represent just the cooling jacket in the region above active zone. On their left surface, they receive convective heat flux from Argon_Ins control volume, while temperature is still imposed on the right.

In HS #37 (Figure 5.8) left mesh is filled with ASTM steel (with reduced density) for the modeling of the expansion compensator. Right mesh consist again of stainless-steel of the cooling jacket, with temperature on the external surface set accordingly to thermocouples data..

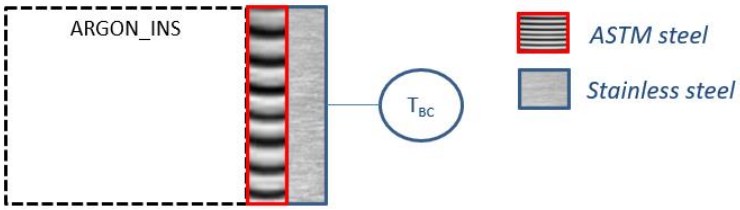

Figure 5.8: HS #37

Five uppermost HSs model upper plenum region from EL 1290 mm to EL 1500 mm. Temperature is imposed on the right surface.

HS #43 is the Al_2O_3 upper plate specified as boundary structure for COR rings. Outer surface for this HS is adiabatic.

Thermal insulation heat structure are allowed to receive also radiative heat flux on the left surface, which is mainly transmitted through 0.5 mm thick *gray-gas* argon bypass.

This QUENCH-06 Input is then launched in MELCOR v2.2, and the results of the simulation with appropriate comments are illustrated in the next chapter.

6 QUENCH-06 MELCOR Input Results

MELCOR calculation of QUENCH-06 test covers all phases, from the first heat up transient until Rest at 9000 s.

Chapter 6 is composed of two parts. The former will present the result of *Reference* case study, in which Urbanich-Heidrich correlation for Zircaloy-Steam is exploited. The dissertation will include the FOM cited in Section 3.5, both from a qualitative and quantitative point of view, and comments of the results. On these main aspects, Fast Fourier Transform Based Method (FFBTM) Analysis will be performed to practically evaluate accuracy of input results and highlight further development needs. The latter instead will be devoted to estimate the sensitivity of the tool in respect of several different zircaloy oxidation formulations.

6.1. Overall Phenomenology Qualitative Assessment

In the following plots, values predicted by *Reference* input will be addressed as Reference.

This section will deliver a brief overview, from a qualitative standpoint, of the response of the system in predicting the phenomenologies occurring in the four main stages of QUENCH-06 experiment, which are represented by means of power trend in Figure 6.1.

At the end of Preparation phase, power supplied is raised from 4 kW to 11 kW, while the test section is crossed by argon and steam [Figure 6.1]. FRS temperature increases up to 1100 K in the midplane of active region at t = 1955 s. MELCOR input successfully predicts this heat up transient [Figure 6.2] and the subsequent first hydrogen generation [Figure 6.3], which is mostly occurring in the upper region of the active zone, around EL 900 mm.

Power is then kept for the following 4046 s, i.e., Preoxidation phase. With the system being in stationary condition, bundle temperature is estimated constant in time accordingly to the experimental trend. Nevertheless, Zircaloy-Steam oxidation is

still occurring because of some hot region characterized by surface temperature higher than 1100 K. As shown in Figure 6.3, predicted hydrogen generation is qualitative similar to the actual trend, but it tends to slightly deviate from the experimental line, and the reason will be explained in Section 6.2.3.

With the on-set of Power Ramping, supplied power is enhanced to further boost structures heat up and hydrogen production. Once again, bundle temperature increase is well estimated, as shown in Figure 6.2, but the hydrogen production rate calculated by MELCOR input is lower than the response of GAM-300 device, as results from the in inferior slope in time. Nevertheless, the input deck is qualitatively able to describe the high temperature oxidation on zircaloy structures.

At t = 7179.5 s quenching condition is fulfilled and the fast water injection system inserts into the test section 4 l of water in 5 s. Concurrently, steam source is turned off, argon flow rate is switched to the upper plenum, and power is set to 4 kW to reproduce decay heat in nuclear fuel. With 30 s of delay, main reflood injection fills the cooling chamber at a rate of 42 g/s for 255 s. Quench phase stresses the input deck, which is not able to predict the sudden evaporation of preinjected water and the re-heating of the bundle structures. Of course, as plotted in Figure 6.3 this discrepancy results in the failure of the input in estimating the post fast preinjection hydrogen generation, that is about 4 g.

At t = 7431 s quench is turned off, no more power is supplied and argon becomes the only flowing species in a now cold test section. Rest stage does not introduce any particular challenge to QUENCH-06 input, which represents a system constant at 400 K with no more ongoing oxidation reaction.

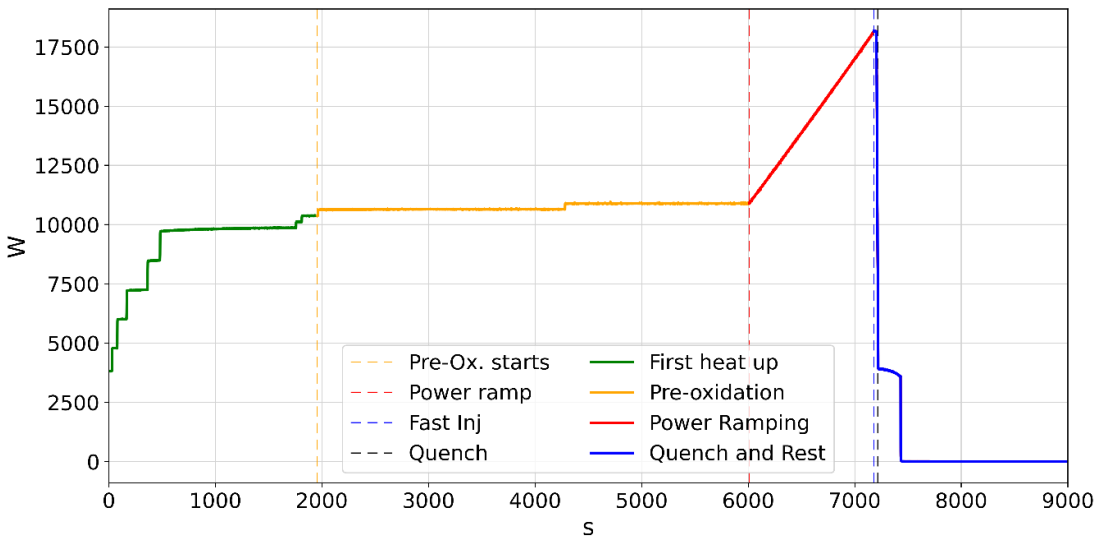

Figure 6.1: Power supply and QUENCH-06 stages

Table 6.1 below reports the main mass sources specified into QUENCH-06 Input, in agreement with actual test injections.

Time [s]	Event	QUENCH-06 Input Flowing mixture
0	Test starts, heatup from 873 K to 1473 K	3 g/s steam 3 g/s argon
1965	Preoxidation stage onset, power at 11 kW	‘’
6011	Power ramping	‘’
6620	Corner rod B withdrawal for metallographic analysis	‘’
7179.5	Reflood on-set through fast water injection	0.78 g/s water 3 g/s argon in bundle head
7184.5	Fast water injection ends	3 g/s argon in bundle head
7215	Main quench, power to 4 kW	42 g/s water 3 g/s argon in bundle head
7431	Power shutoff, quenching ended	3 g/s argon in bundle head
11420	Test termination	-

Table 6.1: QUENCH-06 Input mass sources

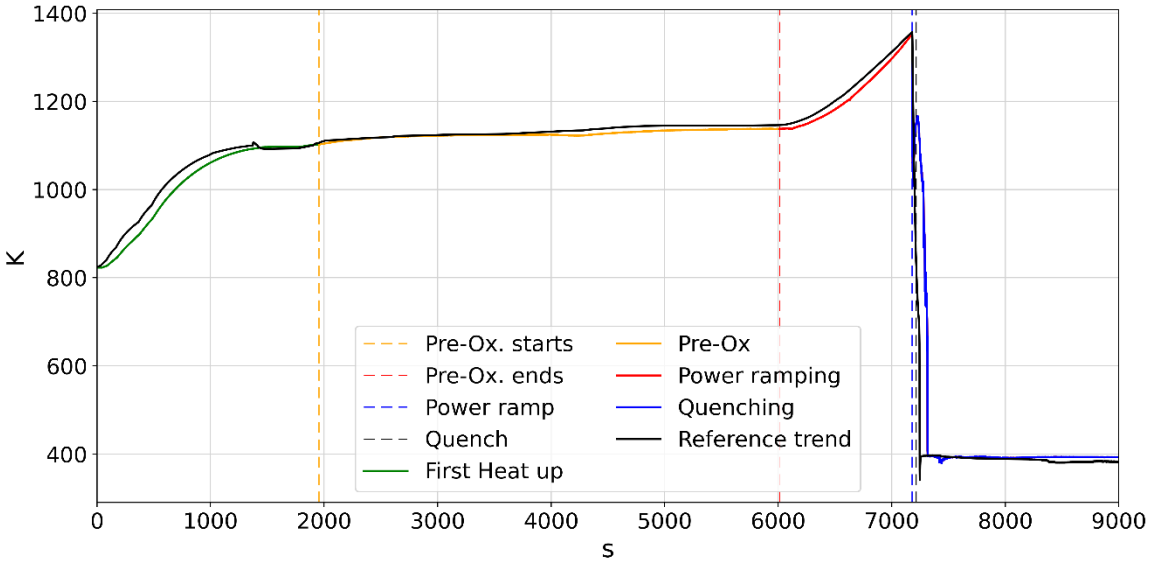

Figure 6.2: EL 550 mm temperature comparison

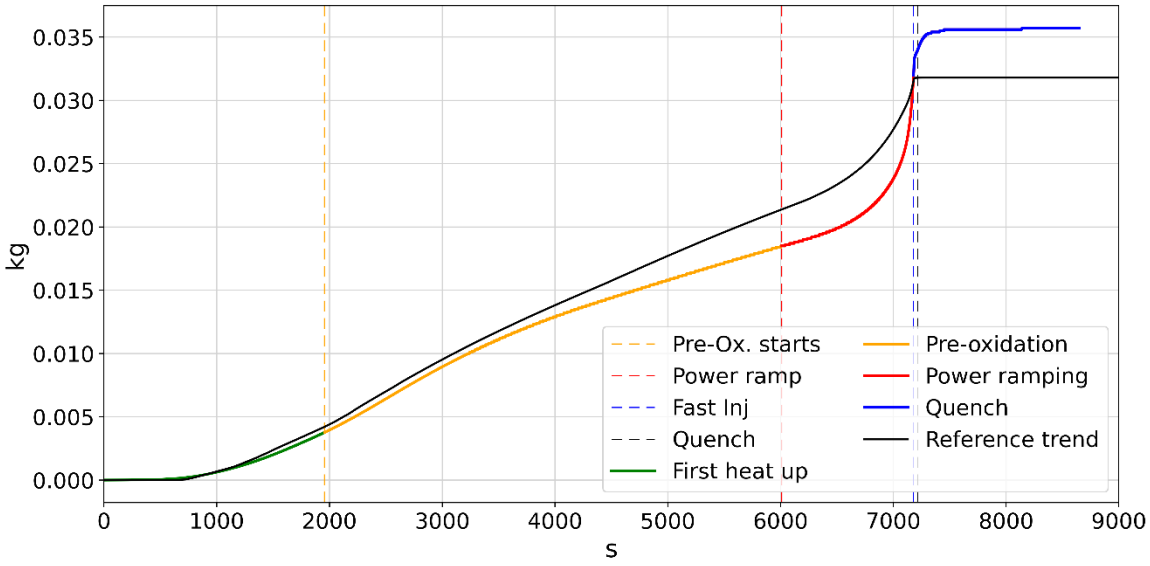

Figure 6.3: Hydrogen cumulative production comparison

6.2. Analytical Description of *Reference* Input Results

Current section is devoted to presenting a detailed analytical description of the main phenomenologies and physical processes predicted by QUENCH-06 *Reference* input. Most important results will be further addressed from a quantitative point of view for delivering a practical estimation of the accuracy of the developed input deck.

6.2.1. Power Balance

Power balance evaluated by MELCOR input is plotted in Figure 6.4. It has already been stated that the actual power specified in reports should be reduced accounting for external wires resistances. Flowing mixture removes though convection 4500 W between EL -250 mm and the off-gas pipe junction elevation during preoxidation, when the system has quasi-stationary behavior.

Violet dashed line shows stored power trend in fuel rod simulators, corner rods and shroud.

Green line represents the power transmitted to the left surface of the thermal insulation system. In order to deliver an accurate description of the power lost to environment, it should be included also the fraction of power discharged on the zircaloy shroud. Unfortunately, it is hard to identify a variable assessing this content. Nevertheless, it is possible to guess that the power lost outside the test section during preoxidation is about 2000 W, which is consistent with [1], just by adding to *Shroud Losses* line the content of *Pstore* line, that actually represents power transmitted to the shroud that is not spent in heating up thermal masses.

Power released by zircaloy oxidation becomes predominant in the late power ramp phase, implying a sudden additional heat up of bundle structures until quenching.

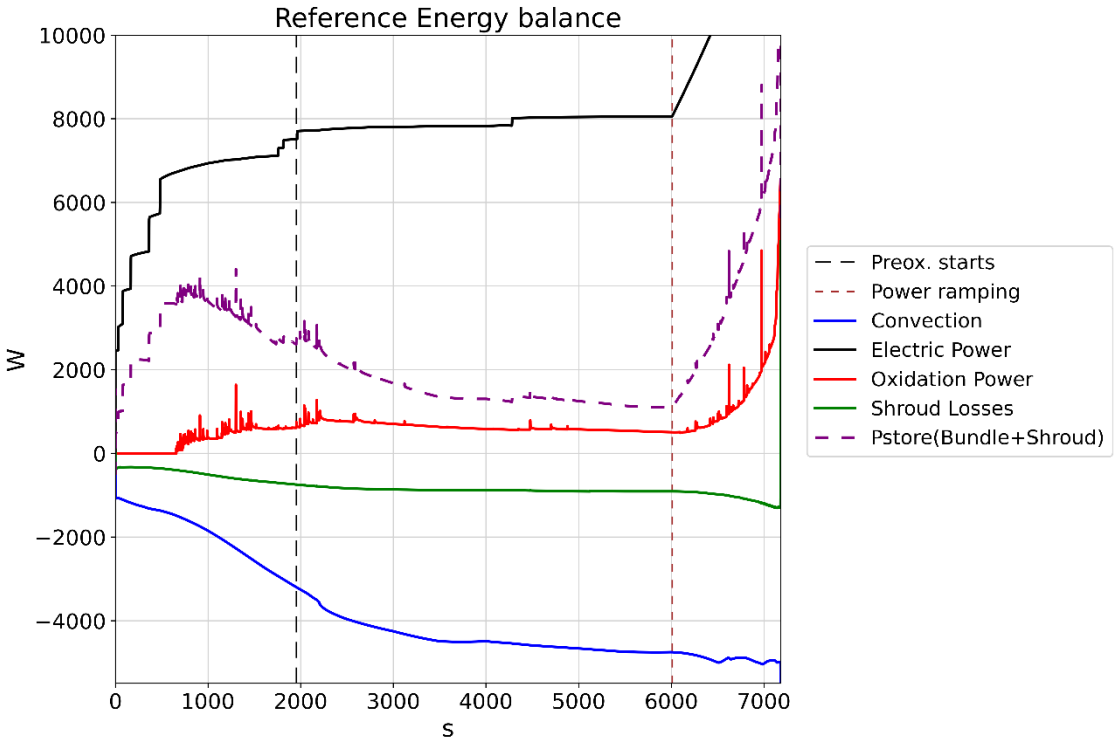

Figure 6.4: Power balance

6.2.2. Pressure

As mentioned in Section 3.5.1, the estimated pressure drop across the bundle until quenching is about 8000 Pa. Given the relative low density of the flowing species, the main content is due to the form losses across the grids. The choice is to not equip QUENCH-06 MELCOR simulation with concentrated loss coefficient since no data has been found in reports.

Tank_Out ACV controls the pressure evolution for the bundle placed below. In order to reduce the computational efforts and stabilize the numerical resolution, its pressure has been set constant to 2 bar for the whole transient. Pressure experimental devices show fluctuations mainly due to flow intermittences. However, wave amplitude is small enough to not have any significant consequences on the thermodynamical evolution of the system.

As concern the pressure after the quenching phase, the overall drop is well predicted by the code, proving that the implemented geometry is consistent with the actual test section.

In Figure 6.5 exponential data and code predicted pressure are presented.

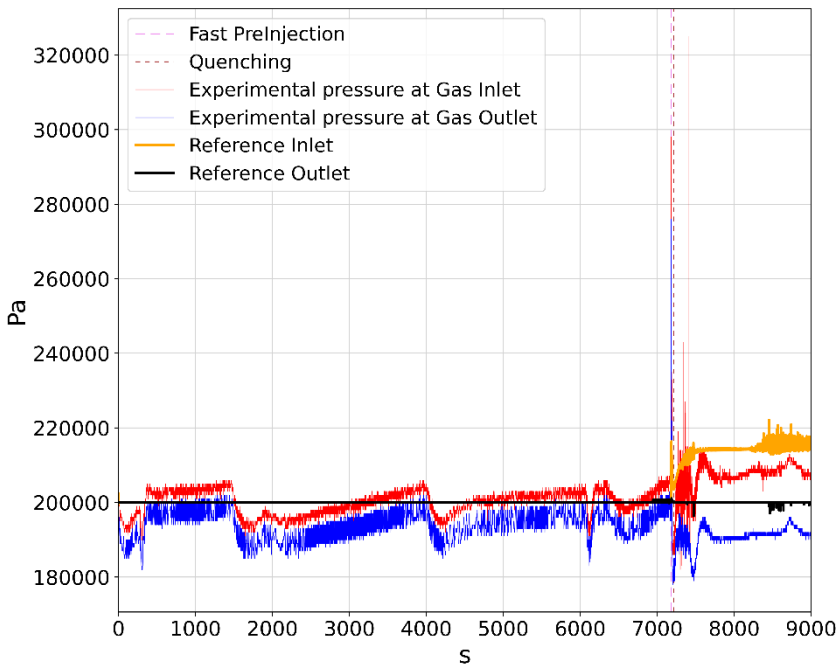

Figure 6.5: Pressure comparison

Fast water preinjection causes a spike in bundle pressure up to 3 bar. Main reason behind the underprediction of such spike by QUENCH-06 simul is due to the simplified layout of the inlet pipe, in which actual cross sectional area and length

have been modified just to ensure the correct boundary condition of 4 l of water to enter the system within 5 s. The spike at gas inlet during quenching is assumed to be just signal noise.

6.2.3. Hydrogen production

Hydrogen is generated by the oxidation reaction occurring on zircaloy structures exposed to high temperature steam. As described in Section 3.5.2, the adoption of Urbanich-Heidrich correlation tends to overpredict the hydrogen build-up in low temperature regime, and underestimate it when surface temperature overcomes 1900 K. This trend is clearly visible in Figure 6.6 on the left, in which the estimated cumulative H_2 mass grows faster than the output of GAM-300. On the other hand, when power is quickly ramped up, bundle active region exceeds 1900 K and the hydrogen production rate increases more than estimated by the code. The result is a steeper hydrogen production gradient in experimental trend just before the fast water preinjection. Nevertheless, given the rather high uncertainties involved in such process, the code is thought to be sufficiently accurate in predicting the on-set and the cumulative hydrogen production until quenching.

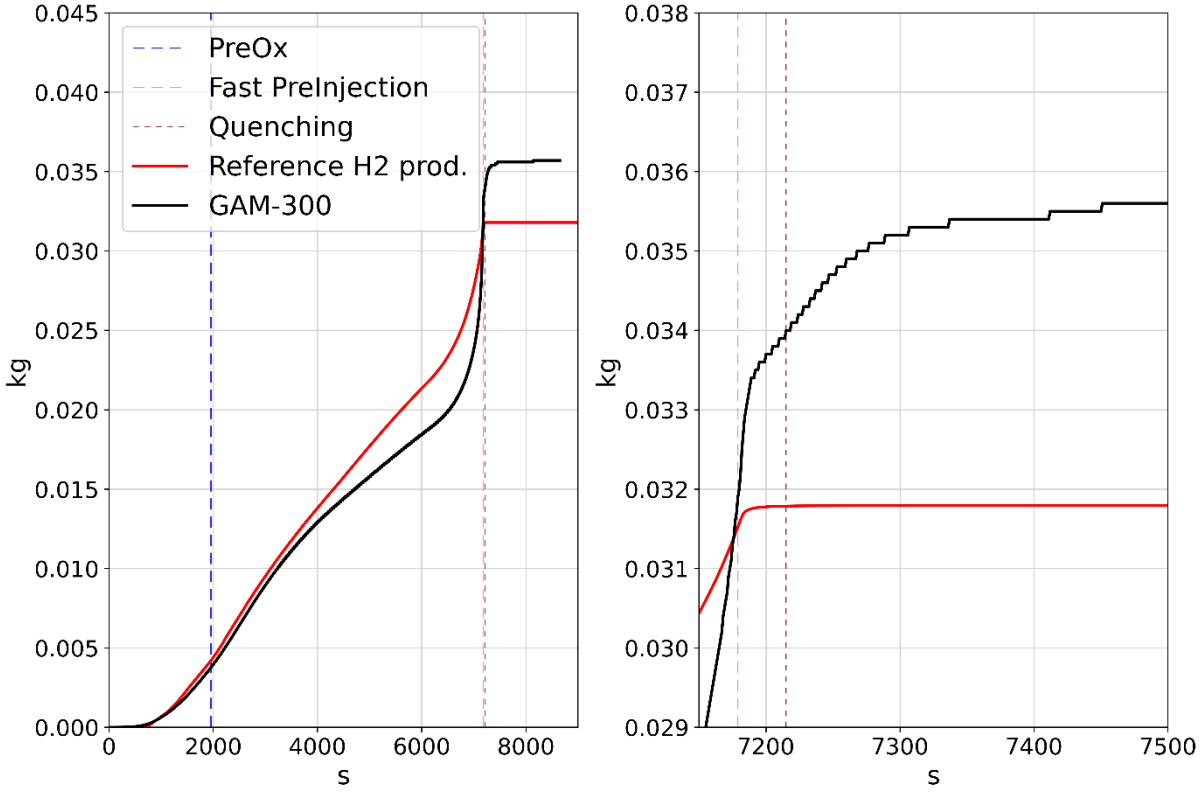

Figure 6.6: Hydrogen cumulative mass comparison

Figure 6.6 on the right reports the hydrogen generation post fast water preinjection. In Section 3.5, it has been stated that, even if power has been reduced to simulate decay heat, bundle is still capable of inducing a partial evaporation of the preinjected water. The steam arising cools down quite ineffectively zircaloy rods and shroud, resulting in a further oxidation and hydrogen production. It is estimated that ~4 g of hydrogen has been released between t = 7179.5 s and the end of the test. Unfortunately, as it will be presented in the next sections, MELCOR developed input lacks the capability to detect and reproduce this evaporation in such a limited time interval. Therefore, surface temperatures do not increase again, and post fast preinjection hydrogen generation is not predicted by the tool.

Thermal evolution of bundle structures in given radial position-altitude will be characterized by a lumped temperature, measured at its outer surface. Temperature estimated by the code in a cell at a selected altitude will be plotted against the relative thermocouple data.

6.2.4. EL -250 mm

First detection point of QUENCH-06 is located in correspondence of the fifth axial level of the COR structure, that is linked with CVH_02. As concern the mixture temperature, shown in the upper graph of Figure 6.7, model well predicts the overall trend. MELCOR Fluid Inlet Temperature is the COR channel temperature of the cell *(ring = 2, ax. Level = 5)* and not the temperature of the CVH_02, to be more accurate in representing the actual position of the thermocouple thanks to the adopted dT/dz Model. Regarding shroud component, isothermal behavior in time is calculated in agreement with the experimental measurements.

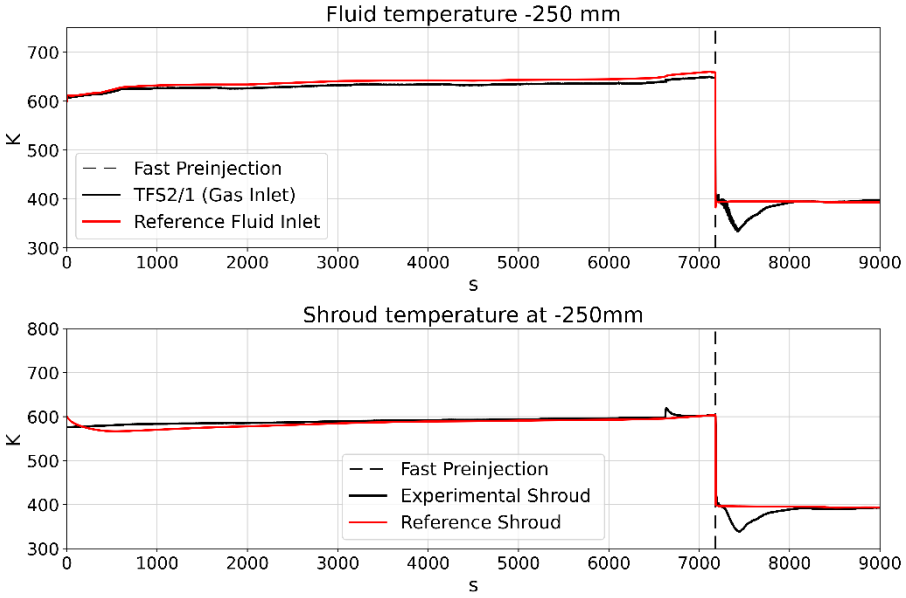

Figure 6.7: EL -250 mm temperature comparison

Power released by molybdenum electrode is not sufficient to induce a sudden evaporation of the preinjected water at this elevation. Therefore, the slight heat up displayed in experimental trend during quenching is due to the fact that the fast preinjected water is 30 K colder that the main water flow entering with 30 s of delay. This transient phase seems challenging to be modeled by the MELCOR input.

6.2.5. EL 50 mm

Figure 6.8 exhibits a predicted outer ring FRS temperature at this elevation ~100 K larger than the actual value. This overestimation is believed to be caused by an excessive fluid heating in the lower electrode region (i.e., from EL -250 mm).

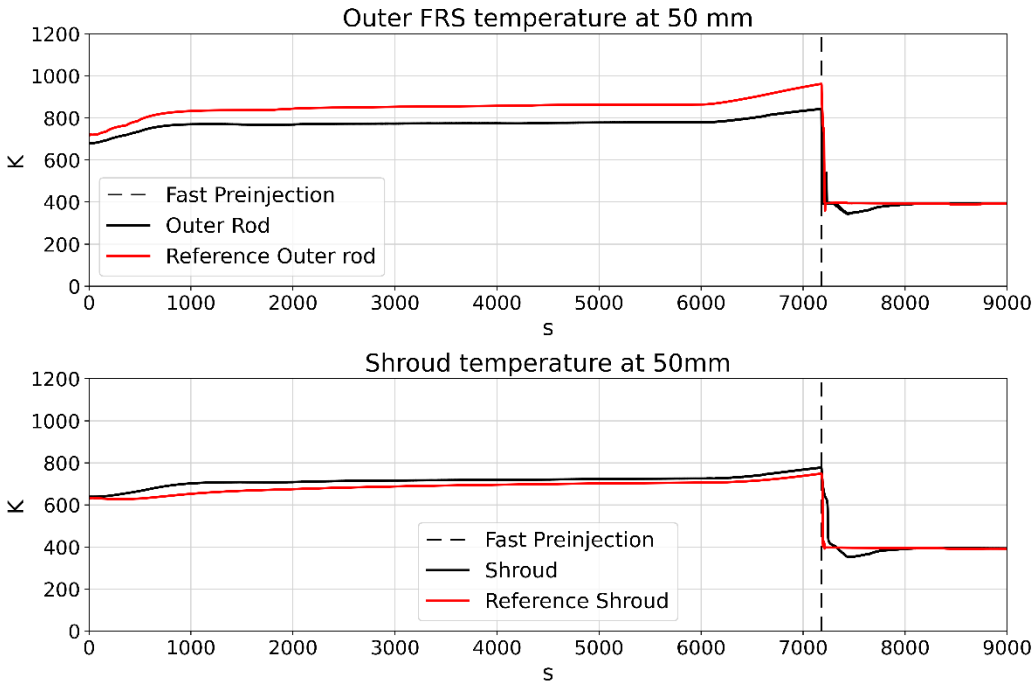

Figure 6.8: EL 50 mm temperature comparison

On the other hand, shroud surface temperature matches closely the experimental trend. Nonetheless, from EL 50 mm it is possible to notice that MELCOR input predicts a radial temperature gradient greater than the real temperature distribution at a given altitude. Flat trend of temperature in radial direction occurs because the oxidation establishes power sources in all the structure at the different radii [Figure 3.16].

In Figure 6.8 it may be expressed also the ~~inability~~ limit of the developed ~~model~~ nodalization to describe the partial evaporation, occurring in the active region, of the 4 l of fast injection water.

6.2.6. EL 550 mm

FRS temperature at the midplane of the active height are in compliance with the cladding thermocouples output. Outer rod shows a limited overprediction of about 40 K, but it is qualitatively in agreement with actual trend. Prediction for the unheated central rod, which is not reported in Figure 6.9, matches the experimental trend.

Regarding the zircaloy structure located in the external ring, calcualtion delivers a trend lower than expected of about 80 K. This difference is more pronounced during the stationary period of preoxidation and it shrinks during power ramp.

In Figure 6.9 below the overall temperature evolution at EL 550 mm is plotted.

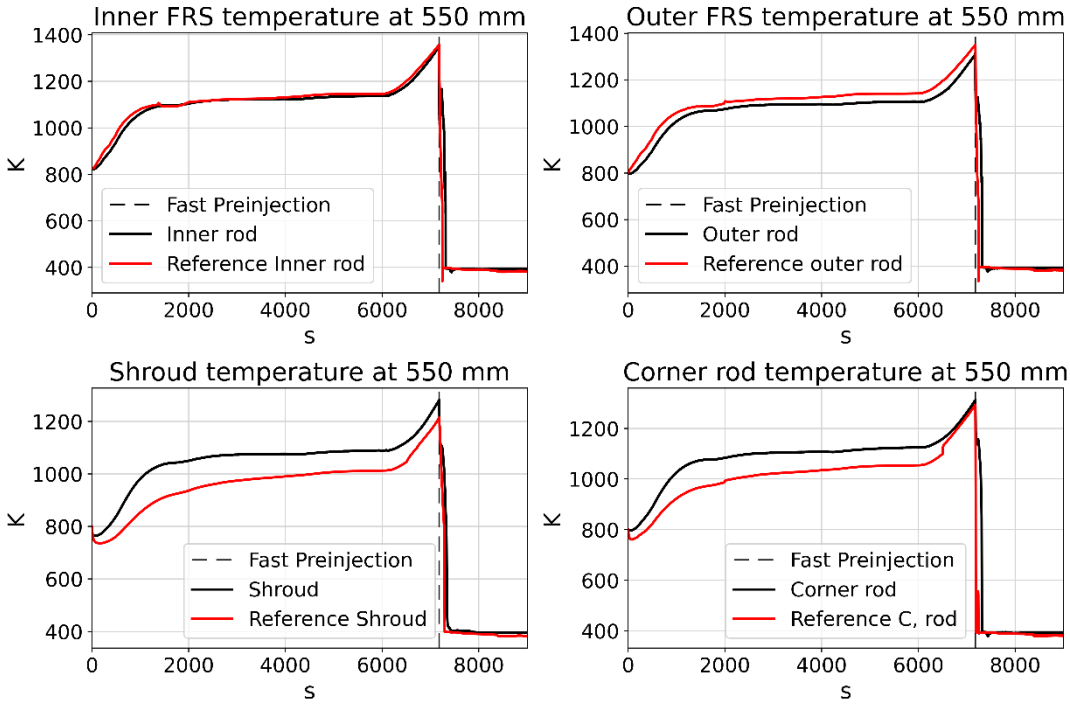

Figure 6.9: EL 550 mm temperature comparison

At this elevation it is clearly noticeable how the QUENCH-06 input is unable to predict the evaporation of the preinjected water. Drop in estimated temperature is monotonous, and the final value is more or less constant until the end of the simulation.

In Figure 6.10, detailed temperature trends for the two equivalent fuel rod simulators are reported to highlight how the input fails to describe the re-evaporation.

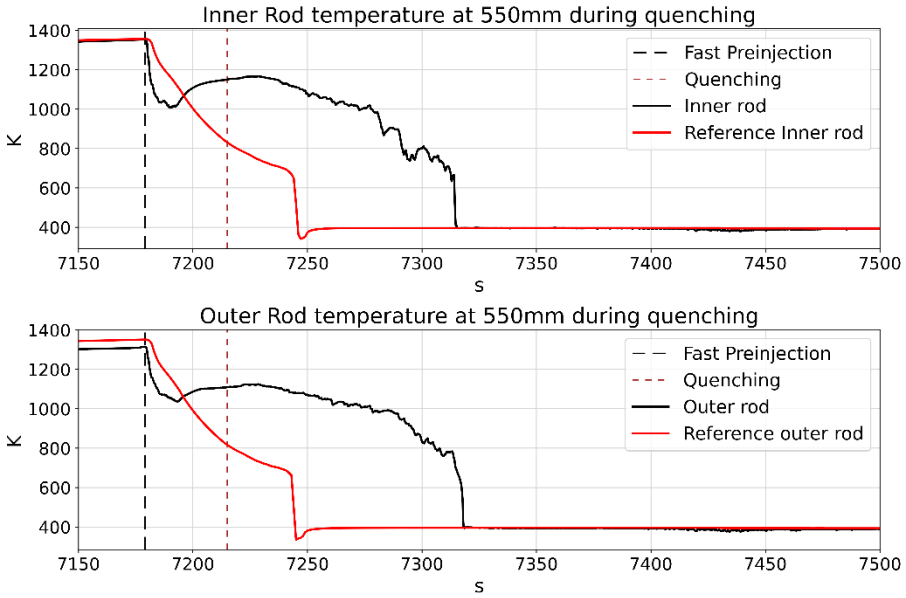

Figure 6.10: EL 550 mm re-evaporation

6.2.7. EL 950 mm

This altitude corresponds to the hotter region of QUENCH-06 test bundle. MELCOR model delivers high accurate FRSs surface temperature. As displayed in Figure 6.11, the temperature gradient in radial direction is steeper than the experimental, resulting in slightly colder corner rods and shroud.

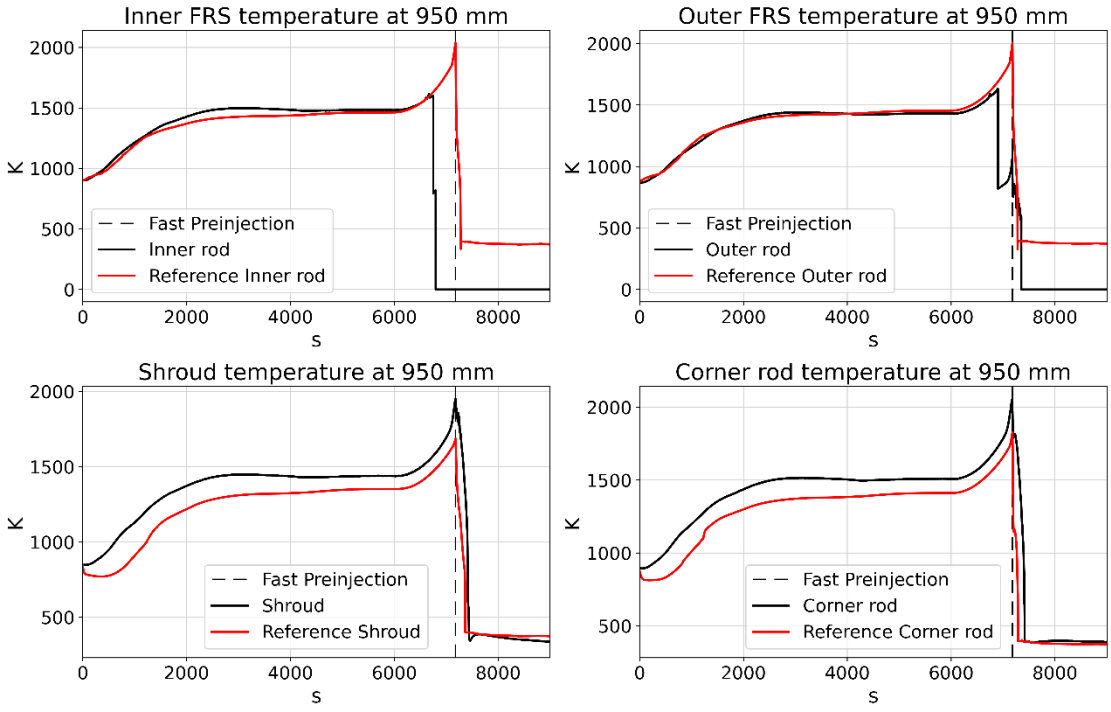

Figure 6.11: EL 950 mm temperature comparison

6.2.8. EL 1250 mm

The upper portion of the test section stresses the most the developed computational input. In this region zircaloy shroud in surrounded by stagnant argon, which is rather difficult to represent.

In the early stage, model predicts an almost null temperature increase for the FRSs, while the shroud is even subject to cooling. Reason behind this estimation is that test section at this altitude may be affected by the presence of condensed film. Given the negligible power generated in molybdenum electrode during Preparation and the effectiveness of the thermal insulation system to remove heat from the bundle (especially at this elevation, where the cooling jacket temperature is almost constant to 300 K), a fraction of steam could condense, moving downward from the off-gas pipe towards the active region. In QUENCH-06 facility, this phenomenon occurs in the off-gas pipe, but bundle thermocouples at EL 1250 mm do not detect any drop in temperature due to condensed film.

Flowing mixture is not able to remove power from the FRSs, enhancing their surface temperature. This aspect causes an excessive radial thermal gradient between the rods and the shroud, as displayed in Figure 6.12.

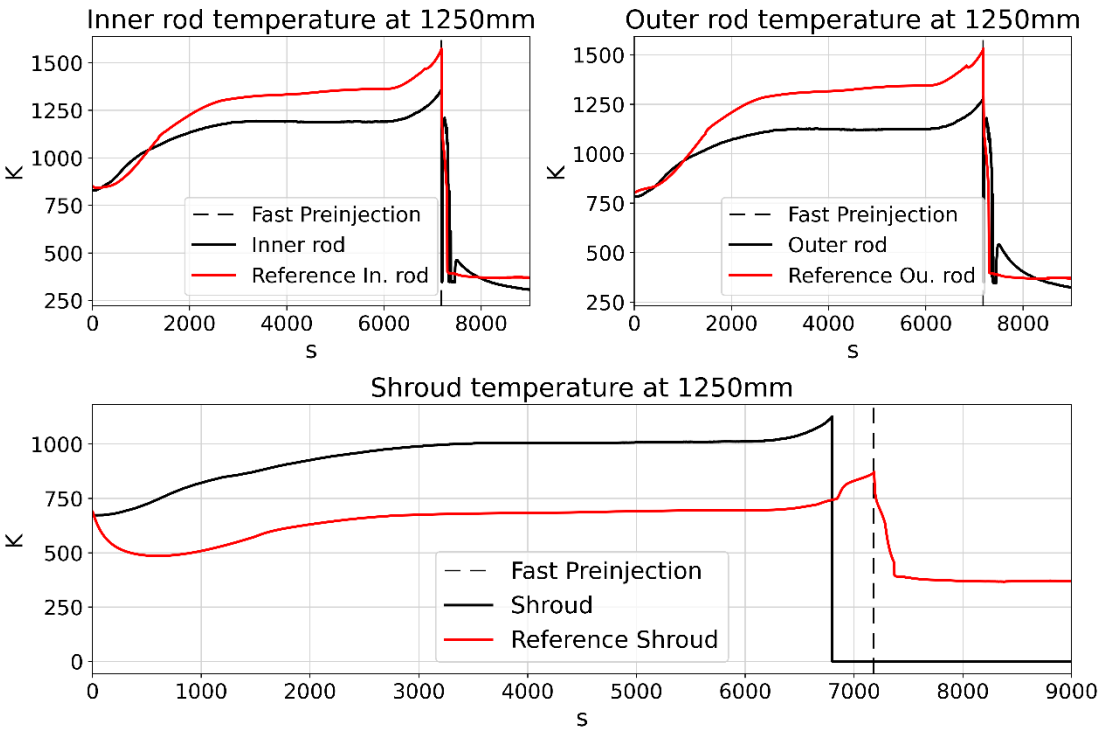

Figure 6.12: EL 1250 mm temperature comparison

The identified reason for temperature discrepancies is that *Cooling Jacket and Argon_Ins ACV are not correctly modeling the thermal losses at EL 1250 mm*. If the heat sink fails in removing heat from the mixture, the power generated enhances fluid bulk temperature and subsequently rod surface temperature of the structures. In a previous version of QUENCH-06 MELCOR input, the thermal insulation at this elevation was represented as just a two-layers heat structure, in which the first mesh was filled by Argon handled as solid material. Thermo-physical and mechanical properties of argon were inserted according to [17] in MP package. However, even with in that layout system was not able to assess the thermal losses. At this elevation indeed, bundle transmits power towards the environment mainly through **radiation** across the stagnant meatus, without relying on neither conduction nor convention. It is impossible to enable the radiative exchange between two nodes bounding a single mesh, and hence the representation through HS has been discarded. Argon_Ins ACV is a more correct approach , but further studies are recommended for the resolution of the discrepancy between experimental measurements and predicted trends at EL 1250 mm.

6.2.9. Axial Temperature Profile

This section presents a pair-wise comparison between the experimental data and MELCOR results regarding the axial temperature profile of shroud and FRS in Preoxidation, Power ramp and Quench phase.

6.2.9.1. FRS Axial Temperature Profile Comparison

FRS temperature is overall well predicted by the model. In the preoxidation stage, the calculated total axial gradient in active region is slightly lower than the experimental distribution, but during power ramp this difference is shrinked. A small overestimation is presented in the upper region, maybe due to the excessive default molybdenum resistivity.

Regarding the right plot in Figure 6.13, quench injection flattens fuel rod temperature profile to 400 K. However, it is noticeable that the liquid level does not cover the entire elevation of the test section, because the temperature value at EL 1150 mm is far higher than in the region below. The failures of the thermocouples between EL 750 mm and 950 mm make hard to estimate just on this basis the elevation of collapsed level of the water pool. Quench front level tracking will be further investigated in 6.2.11.

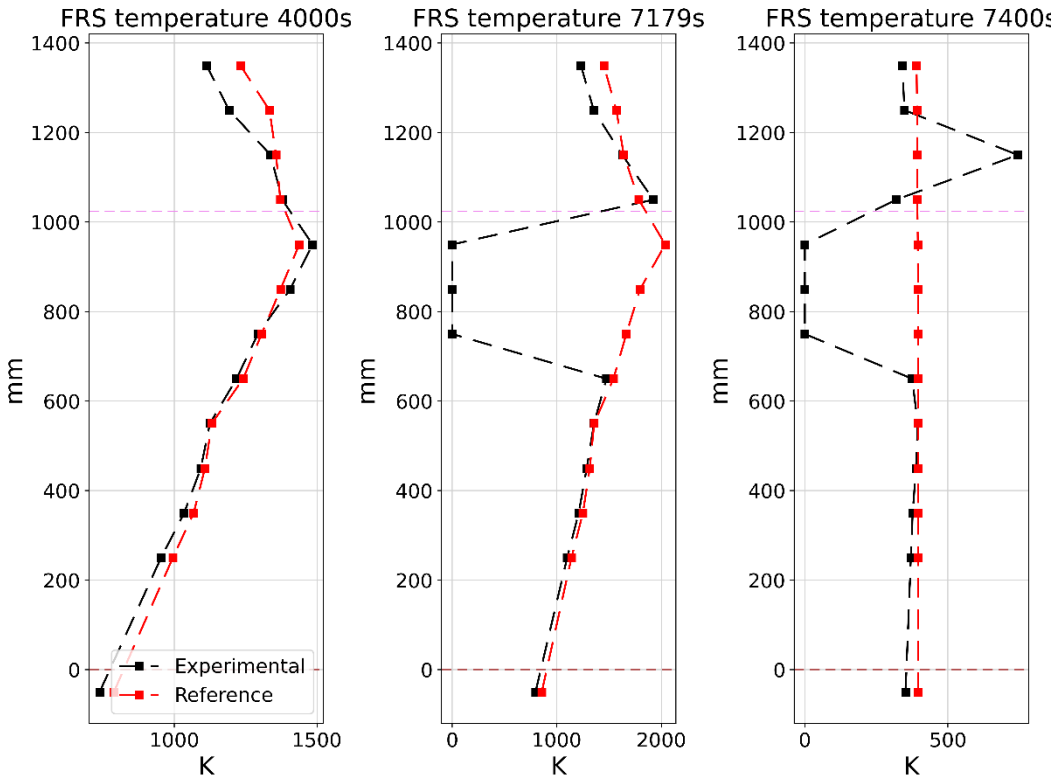

Figure 6.13: FRS axial temperature comparison

6.2.9.2. Shroud Axial Temperature Profile

In Figure 6.14 shroud experimental temperature distribution in the three main stages is displayed against the MELCOR previsions.

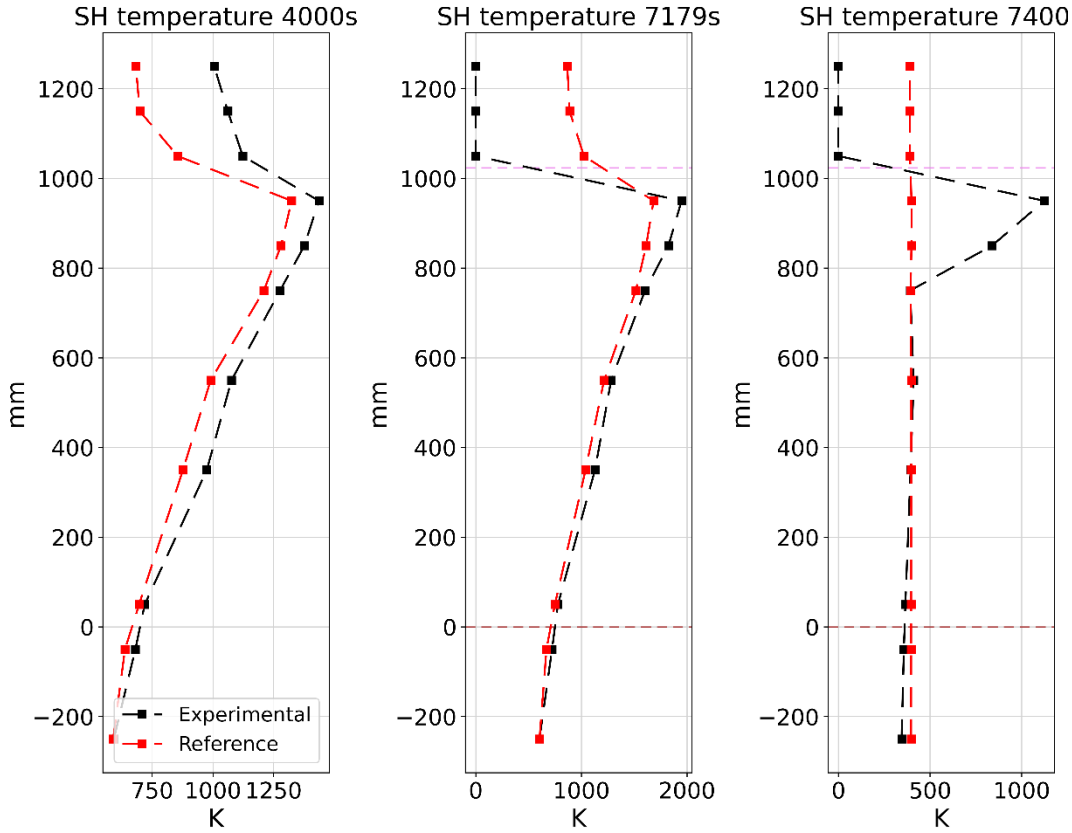

Figure 6.14: SH axial temperature comparison

As expected from previous dissertation, model calculates shroud temperature profile lower than the actual trend, in particular in the preoxidation period. During power ramping, there is certain agreement between the two, even if in the hot zone discrepancy is enhanced. Nevertheless, from a pure qualitative standpoint, model has proven its capability to predict power distribution and the main phenomenologies.

Again, the major divergence is outlined in the hot region at t = 7400 s. Bundle is wetted up to an elevation between 750 mm and 800 mm, and above it is cooled by just the argon from the upper head and the steam arising from the evaporation of the quenching water. Since the model does not predict this phase change, the peak in temperature profile cannot be evaluated and the result is a flat profile, meaning of an estimated complete bundle drowning.

6.2.10. Oxidation Profile

The estimated oxide thickness profile delivered in Figure 6.15 for the corner rod withdrawn from the system at t = 6620 s is in agreement with the metallographic analysis outcome. The limited overestimation on the midplane may be due to uncertainty in the experimental measurement or it may be traced back to Urbanich-Heidrich oxidation formalism, which tends to represent thicker oxide layer when surface temperature is less than 1800 K.

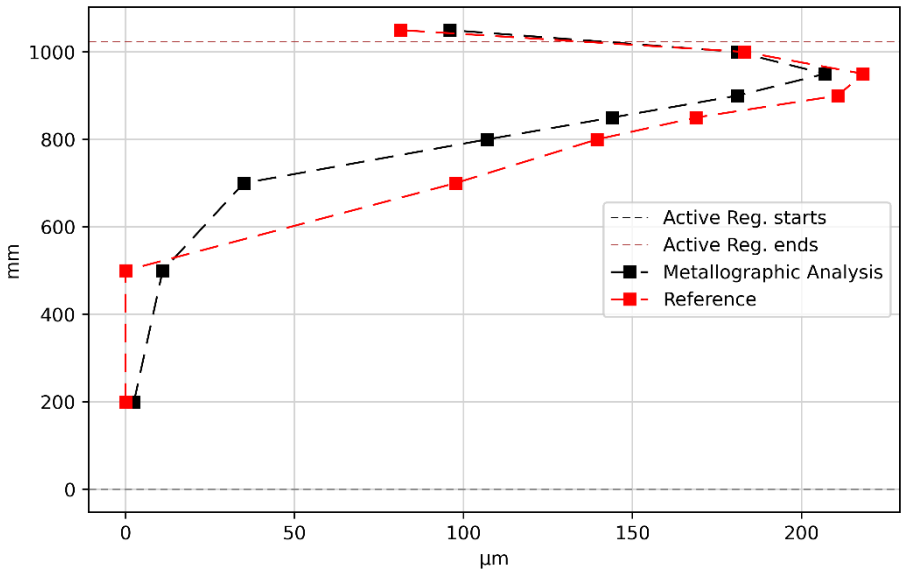

Figure 6.15: Corner rod oxide layer at 6620 s

MELCOR model calculates 7.26% of corner rods β-zircaloy consumed by steam corrosion in the hot zone, in view of a measured value equal to 6.9%.

For the post test analysis, experimentally derived values are almost everywhere larger than the model output. This aspect may be explained with the sudden heat up following fast water preinjection evaporation. Given the monotonous decrease of MELCOR modeled fuel rods, which is obviously more relevant in the hot zone, limited thickening on the ZrO_2 stratum is predicted between t = 6620 s (time of Corner Rod B withdrawn) and t = 9000 s.

Code input significantly underestimates the autocatalytic oxidation reaction on shroud because its temperature is always lower than in the experimental measurements.

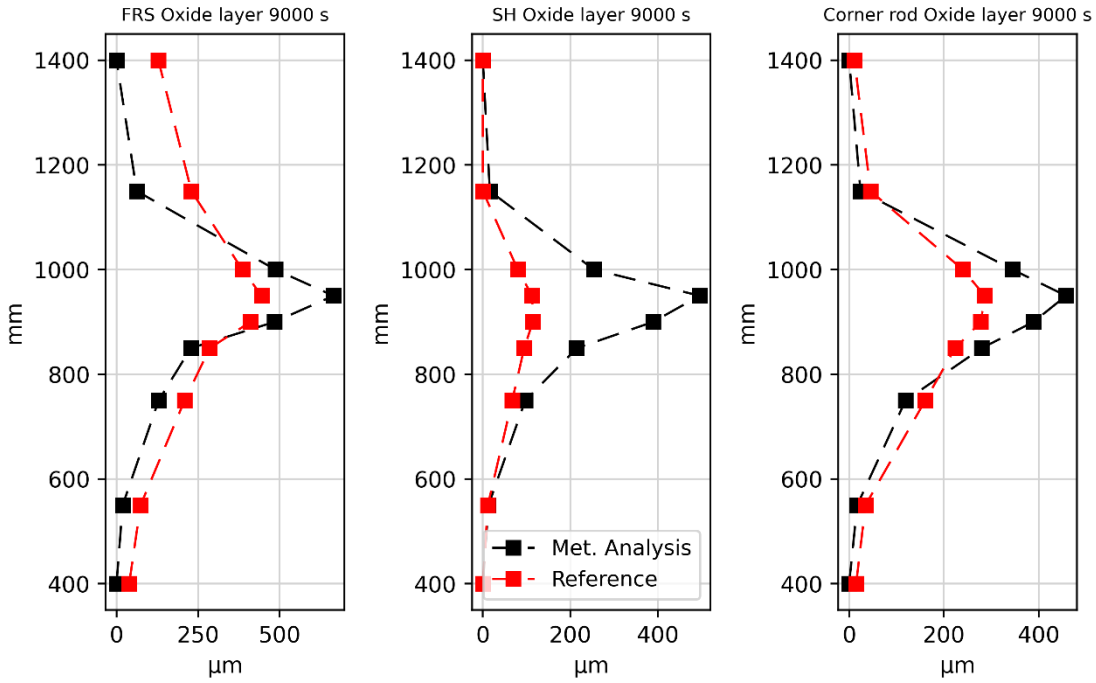

Figure 6.16: Posttest oxide layer thickness

6.2.11. Liquid Level

Figure 6.17 reports the comparison between the actual and predicted collapsed liquid level in the test bundle.

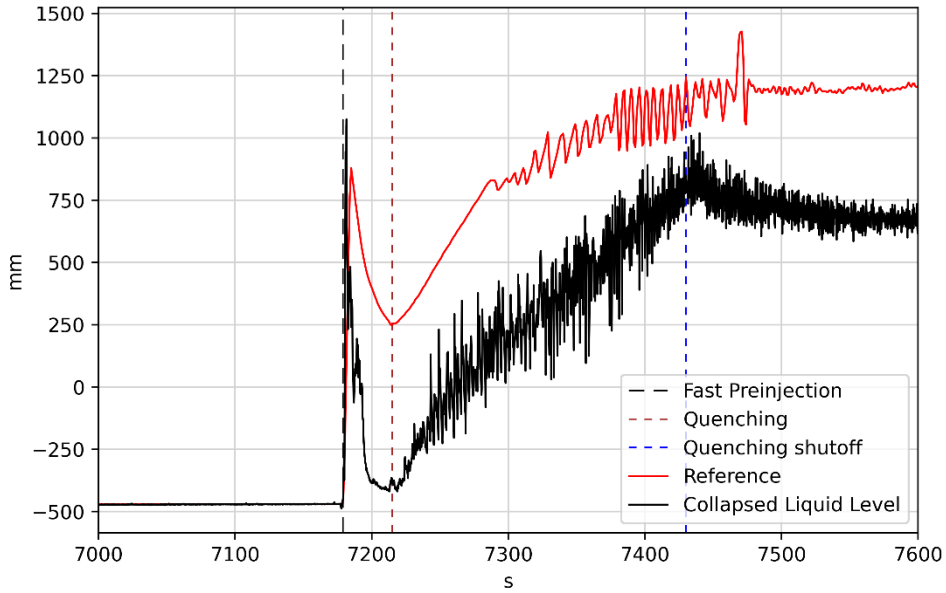

Figure 6.17: Collapsed liquid level comparison

The two peaks in correspondence of fast preinjection time are quite in accordance, but then re-evaporation is not foreseen in the simulation. It is estimated that the overprediction in water mass left in the test section in between the two injections is ~1.8 kg.

6.2.12. FFBTM General Analysis

Quantitative accuracy assessment of code output may be obtained through FFTBM Analysis by considering the amplitude, in frequency domain, of the experimental signal $F_{exp}(t)$ and the absolute error function $\Delta F = F_{calculated}(t) - F_{exp}(t)$ [26] [27]. The tool adopted to perform the FFTBM analysis is the JSI FFTBM Add-In 2007 developed at Jožef Stefan Institute (Slovenia) [28] [29] [30].

The outcome of FFBTM tool is a dimensionless number *AA* that roughly indicates the error in the calculation of the considered variable. Its value may be interpreted as follows [27]:

- AA ≤ 0.3: very good code prediction;
- 0.3 ≤ AA ≤ 0.5: good code prediction;
- 0.5 ≤ AA ≤ 0.7: poor code prediction;
- 0.7 ≤ AA: insufficient.

FOM considered into the FFTBM analysis are the cumulative hydrogen mass, FRS and shroud temperature at EL 950 mm and 1250 mm, FRS temperature at EL 50 mm and 550 mm and the collapsed liquid level. Furthermore, the whole transient is subdivided into three main Phenomenological Windows (PhW), allowing for a quantitative accuracy assessment of code capability under the different boundary conditions.

Results of the FFTBM analysis are displayed in Table 6.2. It should be noted that shadowed cells provide meaningless results since the measurement devices failed.

Variable	PhW [0 s, 6011 s]	PhW [6011 s, 7179 s]	PhW [7179 s, 9000 s
H2	0,15	0,20	0,23
FRS950	0,031	1,08	2,12
SH950	0,13	0,14	0,33
FRS1250	0,31	0,21	0,73
SH1250	0,57	0,89	1
FRS50	0,21	0,21	0,80
FRS550	0,03	0,02	0,49
LiqLev	0,14	0,07	0,94

Table 6.2: QUENCH-06 FFTBM Results

On the basis of these selected FOM, MELCOR *Reference* input delivers accurate results in agreement with experimental trend as concern preoxidation phenomenology, especially regarding the FRS cladding temperature. Major quantitative discrepancies arise while describing the hot bundle promptly cooled down by water and crossed by argon.

6.3. Sensitivity Analysis

The developed input architecture is tested against five additional Zircaloy-Steam oxidation correlations. Until power ramping, most noticeable difference in between the simulation regards the trend of the cumulative hydrogen production, while no major temperature distribution difference is highlighted. This outcome during preoxidation is expected since for T < 1800 K only the *Baker* correlation shows a reaction rate significantly higher than the others. On the other hand, power ramping phase introduces deviation in the results, depicting a more challenging bundle state when *Prater-Courtright* and *Baker* descriptions are adopted.

The following parameters are selected as FOM for the sensitivity analysis qualitative comparison:

- Hydrogen cumulative production;
- Temperature at EL 950 mm for inner ring FRS and Shroud;
- Oxide layer profile on the corner rod at t = 9000 s.

6.3.1. Hydrogen Production in sensitivity analysis

By referring to Figure 6.18, best performing correlation during preoxidation, when bundle temperature is usually lower than 1800 K, is the *Cathcart-Pawel*, while the *Leistikow* delivers a significant underestimation of the hydrogen cumulative mass produced through zircaloy oxidation. On the contrary, *Baker* in the low temperature regime overestimates the trend of hydrogen generation.

Approaching the power ramp phase, bundle becomes hot enough to induce MELCOR to select the high temperature regime for the oxidation correlations. As concern the *Volchek* formulation, it induces a steeper increment in hydrogen mass in respect of the *Urbanich-Heidrich*. For the *Prater-Courtright* simulation, unfortunately timestep drops sharply at t = 7030 s, making the calculation too burdensome, and hence it is not quantitative possible to evaluate the final hydrogen mass. On a qualitative standpoint, the enhanced reaction rate causes a relevant increase in the hydrogen production, greater than the one reported in experimental trend. Same aspects may be referred to *Baker* simulation, in which the overestimation affecting the preoxidation stage is added to the excessive production gradient in the power ramping, resulting in the highest estimated mass of the study.

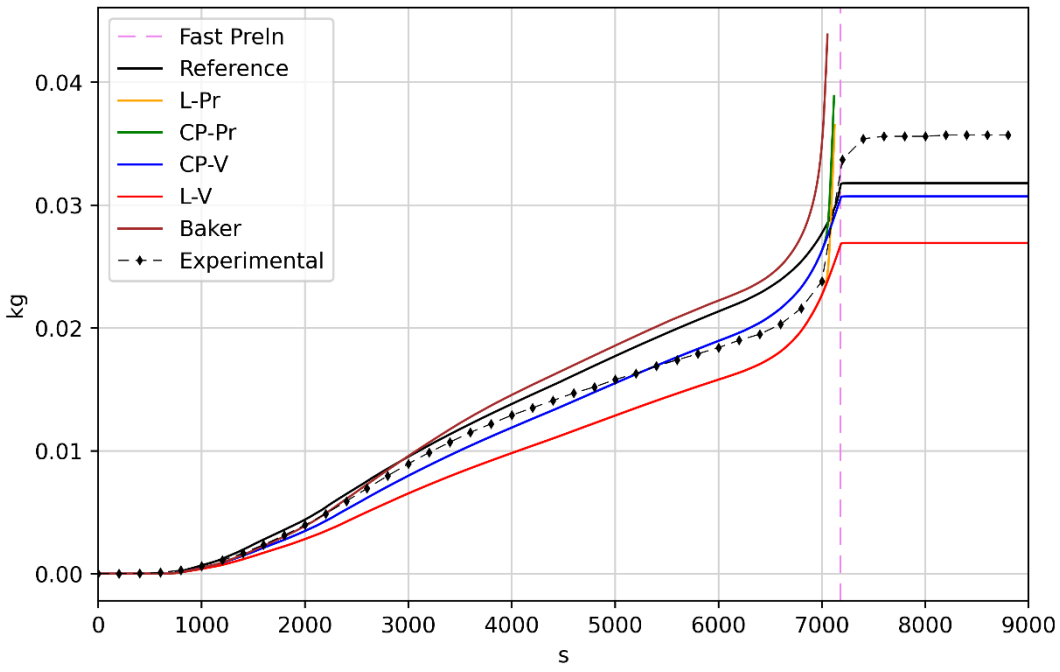

Figure 6.18: Hydrogen Cumulative Mass in SA

None of the completed simulations is able to predict the evaporation occurring in the post water fast preinjection (see Section 1036.2.3).

It is possible to conclude that, even if *Urbanich-Heidrich* correlation provides the final value closest to experimental 36 g of hydrogen detected by GAM-300, the best performing formulation during both preoxidation and early power ramping is the couple *Cathcart-Pawel-Volchek*.

6.3.2. Inner ring FRS Temperature at EL 950 mm in sensitivity analysis

Delivered trend for this FOM is shared by the different simulations for what concerns the preoxidation stage. Dispersion of estimated temperature in this phase is around ~6 K.

In Figure 6.19 estimated temperature behaviors for the inner ring FRS at EL 950 mm are plotted.

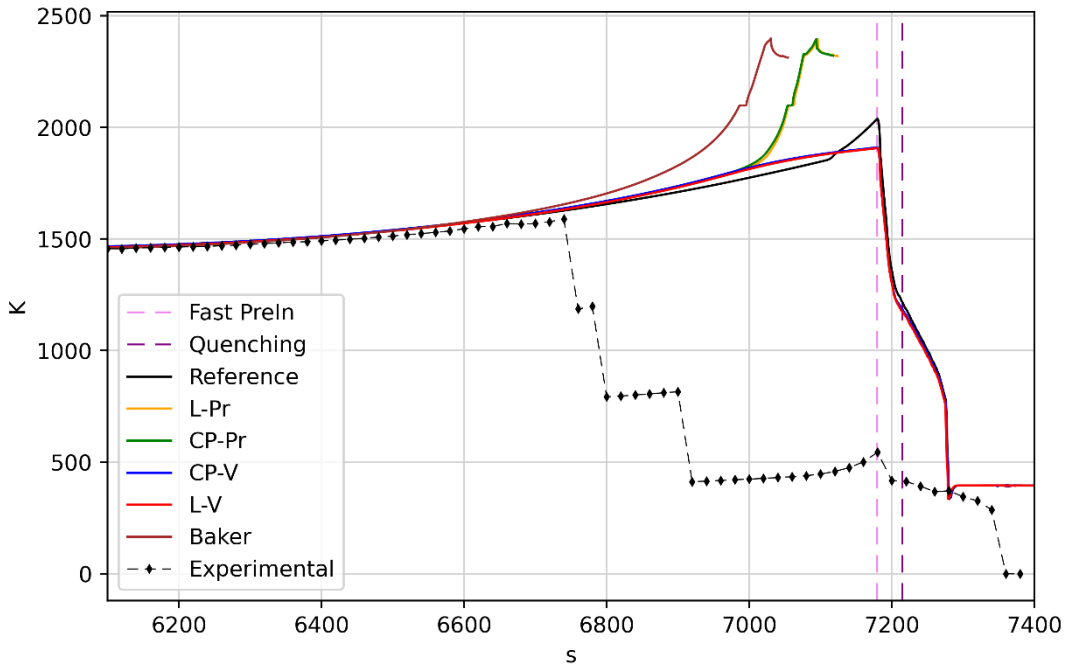

Figure 6.19: Inner ring FRS Temperature at EL 950 mm in SA

Cathcart-Pawel and *Leistikow* correlations adopted in the low temperature regime provide almost indistinguishable results, and for this reason CP-V and L-V temperature trends evolve following the same trend even in power ramping. The same concept can be applied to CP-Pr and L-Pr, except that their prevision deviates significantly at t = 7000s. Effect of Baker enhanced reaction rate even for surface

temperature lower than 1800 K is seen is Figure 6.19, with a trend departing from streamline in the early power ramping phase.

With a bundle maximum temperature expected to be ~2100 K, default *Urbanich-Heidrich* adopting simulation seems the most accurate in reconstruction, with CP-V and L-V delivering a slightly lower peak temperature.

6.3.3. Shroud Temperature at EL 950 mm in sensitivity analysis

As expected from Section 6.2, the adoption of the several Zircaloy-Steam correlations is not able to reduce the too pronounced temperature gradient between rod structures and shroud that affects the system during the quasi-stationary preoxidation stage.

For this FOM, CP-V and L-V results are in agreement with the Reference calculation outcome. As already mentioned, temperature trend for the other three simulation deviates significantly. By observing Figure 6.20 plotting temperature evolution predicted by Baker, CP-Pr and L-Pr simulations, it is possible to guess a shroud failure causing the onset of oxidic molten pool relocation and the melting of the intact shroud metal located below. It is obvious that, given the fine input nodalization, and the fact that the flowing mixture, heavily heated up, mixes with the argon of Bypass ACVs crossing shroud flaw and transmits power to HS representing thermal insulation system, the result is a complex phenomenology that enhances the computational efforts and reduces the time step.

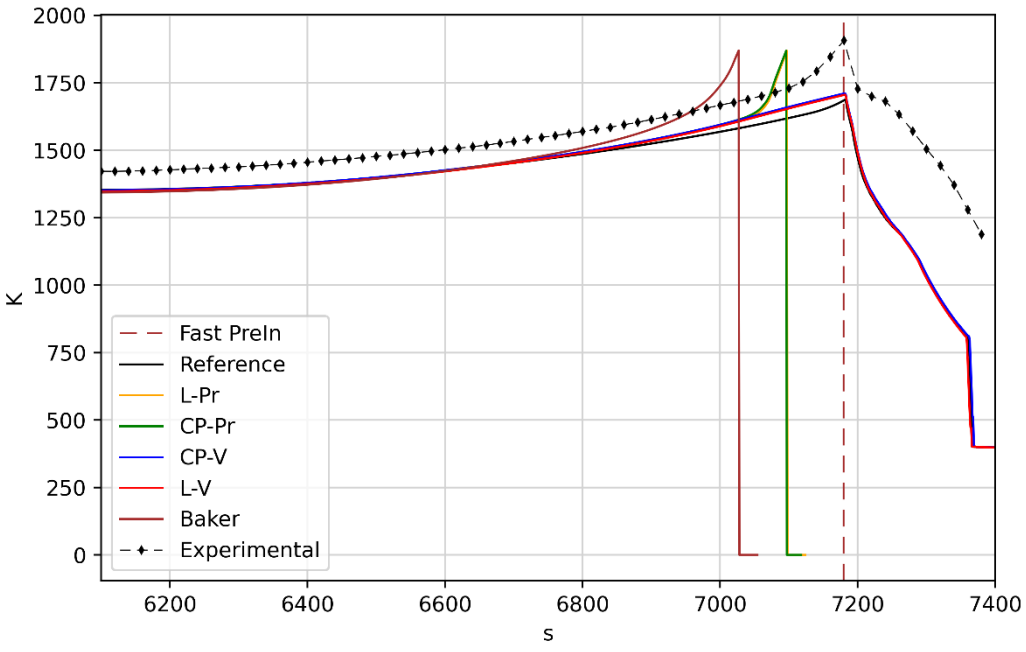

Figure 6.20: Shroud Temperature at EL 950 mm in SA

6.3.4. Corner rod oxide profile at t = 9000 s in sensitivity

Figure 6.21 contains the corner rod oxide layer comparison at t = 9000s between simulations outcomes and the experimental measurements obtained through the metallographic analysis.

Plotted trends of CP-Pr, L-V and Baker refers to the oxide thicknesses in the last calculated step. Nevertheless, predicted profile evaluated during power ramping for these inputs is significantly more pronounced than the actual oxide distribution at the end of test. In addition, L-Pr simulation provides an anomalous ZrO_2 stratum thickness at midplane of active region. That position in the bundle is occupied by the hollow instrumentation tube, characterized by a wall thickness of 0.5 mm. Hence, the result of zirconia layer 0.67 mm thick is not consistent with the real geometry.

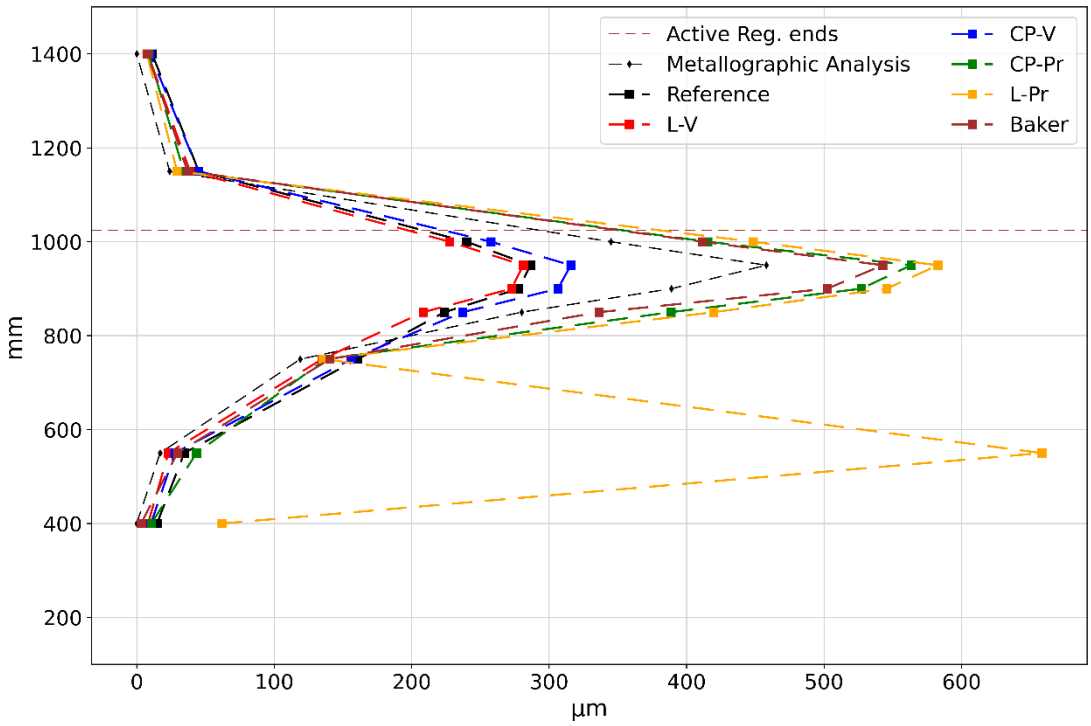

Figure 6.21: Corner rod oxide layer profile in SA

Among the successful calculations, CP-V delivers the profile closest to the experimental measurements.

As conclusive remark of sensitivity analysis conducted by modifying the Zircaloy-Steam corrosion correlation, the input deck adopting *Cathcart-Pawel* formulation in the low temperature regime, and the best-fitted *Volchek* for surface temperature higher than 1900 K is the only one with better capability in reconstruction in respect of the Reference, equipped with *Urbanich-Heidrich* formula. Nonetheless, major

issues, namely the steep radial temperature gradient and the lack in predicting post fast preinjection evaporation, seem to affect every input deck, and hence, as expected, these aspects are not referable to the implemented zircaloy oxidation correlation.

7 Conclusion and future developments

This thesis work is focused on the development of QUENCH-06 input for an independent user validation of MELCOR v2.2 code.

QUENCH-06 is a scaled down, separate effects test facility made of 20 electrically heated FRSs. Main investigated phenomena are:

- Preoxidation of FRS cladding and shroud in a steam-argon environment;
- Build-up of hydrogen source term;
- Bundle behavior during reflood/quenching.

Outcomes and experimental results of QUENCH-06 are used within this framework as validation dataset for **Core Heat up and Degradation models** embedded into MELCOR. MELCOR code is a fully integrated code for NPPs risk assessment developed by SNL on behalf of USNRC. Its architecture is composed by packages, each one devoted to a specific phenomenology, which are able to characterize both stationary conditions and transient sequences, including SA scenarios. In order to check both the accuracy of oxidation model implemented by default in MELCOR, and to assess the variation of the predicted trends against several zircaloy corrosion correlations, the author has set up multiple simulations adopting different Zircaloy-Steam oxidation formulations, outlined in Table 5.6, on the same Input architecture.

Reference model adopts the *Urbanich-Heidrich* correlation for Zircaloy-Steam oxidation. QUENCH-06 thermal-hydraulics is evaluated by means of 13 TCVs and 10 ACVs, while COR package is composed of 42 axial levels and 4 concentric rings embracing test section from the central rod until zircaloy shroud. Heat structures represent the thermal insulation system and they impose boundary conditions for the whole simulation.

Reference input deck is qualitatively and quantitatively judged to predict the overall trend of preoxidation and hydrogen build-up, but it suffers to describe post fast water preinjection evaporation and subsequent oxidation. FRS and unheated central rod surface temperatures are estimated accordingly to experimental measurements, but further studies are needed to assess the higher radial temperature gradient that lowers solid structure temperature in the outermost ring.

Future efforts will concentrate on equipping *Reference* settings with **COR-HTR** (Added COR Heat Transfer Path) and **COR-BCP** (Core Boundary Conduction Parameters) cards [13] implemented in MELCOR for the representation of non-nuclear facility layout. COR-HTR allows for an explicit definition of additional heat transfer paths between COR cells to calculate radiation and conduction. Its adoption is thought to increase the accuracy of the radial heat transfer towards the periphery of the bundle, resulting in a flatter temperature profile and more homogeneous oxide layer thickness on the different structures at the given elevation. COR-BCP specifies parameters for the calculation of conductive energy transfer from core outer ring to boundary heat structure. Through the activation of COR-BCP (coupled with sensitivity analyses for parameters tuning) the input should reconstruct radial losses across insulation system more precisely. Furthermore, it will be possible to include in the conductive energy content the radiative power that shroud transfers towards the cooling jacket in correspondence of the Argon_Ins ACV, introducing feedbacks that will lower FRSs surface temperature.

Regarding the calculation of QUENCH-06 case study adopting different zircaloy oxidation correlations, the most promising outcome is delivered by the *Cathcart-Pawel* formulation for T < 1800 K and *Volchek* for high temperature regime. Even if the main FOM, i.e., the final cumulative hydrogen production, is estimated by CP-V lower than the *Reference* calculation, its trend during preoxidation is closer to experimental measurement. Unfortunately, no input deck is able to solve the main issues affecting the *Reference* simulation, namely the higher radial temperature gradient at a given elevation from rods structure to shroud and the sudden surface heat up following the water fast preinjection evaporation.

Going forward with the improvement of this sensitivity analysis, author will change the nodalization schemes, making it coarser almost everywhere but maintaining the geometry between EL 800 mm and EL 1024 mm. By doing so, computational efforts should be reduced without losing major info in the hot zone, allowing most likely for the completion of Baker, CP-Pr and L-Pr.

Bibliography

[1] W. Hering, C. Homann e J.-S. Lamy, «Comparison Report on the Blinf Phase of the OECD International Standard Problem No 45 Exercise,» Forschungszentrum Karlsruhe GmbH, Karlsruhe (DEU), 2002.

[2] M. Stanojevic e M. Leskovar, «Simulation of the Quench-06 experiment with MELCOR 1.8.5,» *Proceeding of "Nuclear Energy in Central Europe 2001"*, pp. 341.1-314.8, 2001.

[3] IAEA International Atomic Energy Agency, «Fundamental Safety Principles,» IAEA, Vienna, AUT, 2006.

[4] IAEA International Atomic Energy Agency, «SSR-2/1 Safety of Nuclear Power Plant: Design,» IAEA, Vienna, AUT, 2016.

[5] IAEA International Atomic Energy Agency, «TEC-DOC 1971: Considerations on the Application of the IAEA Safety Requirements for the Design of Nuclear Power Plant,» IAEA, Vienna, AUT, 2016.

[6] IAEA International Atomic Energy Agency, «Status and Evaluation of Severe Accident Simulation Codes for Water Cooled Reactors,» IAEA, Vienna (AUT), 2019.

[7] J.-P. Van Dorsellaere, T. Albiol e J.-C. Micaelli, «Research on severe accidents in nuclear power plant,» in *Nuclear Power*, IntechOpen, 2010.

[8] International Atomic Energy Agency, IAEA Safety Glossary, Vienna (AUT), 2018.

[9] IAEA International Atomic Energy Agency, «Deterministic Safety Analysis for Nuclear Power Plants,» IAEA, Vienna, AUT, 2019.

[10] F. Mascari, H. Nakamura, K. Umminger, F. De Rosa e F. D'Auria, «Scaling Issues for the Experimental Characterization of Reactor Coolant Systems in Integral Test Facilities and Role of System COde as Extrapolation Tool,» NURETH-16, Chicago (USA), 2015.

[11] L. Sepold, W. Hering, C. Homann, A. Miassoedov, G. Schanz, U. Stegmaier, M. Steinbruck, H. Steiner e J. Stuckert, «Experimental and Computational Results of the QUENCH-06 test (OECD ISP-45),» Forschungszentrum Karlsruhe GmbH, Karlsruhe (DEU), 2004.

[12] A. Stefanova, J. Duspiva, F. Fichot e P. Groudev, «SARNET Benchmark on QUENCH-11 Final Report,» in *SARNET CORIUM P008*, Karlsruhe, 2008.

[13] L. L. Humphires, B. Beeny , F. Gelbard, D. Louie e J. Phillips, MELCOR Computer Code Manuals Vol.1: Primer and Users' GUide Version 2.2.9541 2017, Albuquerque (USA): Sandia National Laboratories, 2017.

[14] L. Humphries, B. Beeny, F. Gelbard, D. Louie e J. Phillips, MELCOR Computer Code Manuals Vol.2: Reference Manual version 2.2.9541 2017, Albuquerque (USA): Sandia National Laboratories, 2017.

[15] L. Humphries, L. Louie, V. Figueroa, M. Young, S. Weber, K. Ross, J. Phillips e R. Jun, MELCOR Computer Code Manuals Vol.3: MELCOR Assessment Problems Version 2.1.7347 2015, Albuquerque (USA): Sandia National Laboratories, 2015.

[16] B. M.G., *Physics of Nuclear Material Lecture 14 (PowerPoint Presentation),* Milan (ITA): Politecnico di Milano 1863, 2020.

[17] National Institue of Standards and Technology NIST, «NIST-JANAF Thermochemical Tables, NIST Standard Reference Database,» NIST, 1998. [Online]. Available: https://janaf.nist.gov/.

[18] Nuclear Regulatory Commision and Applied Programming Technology, Symbolic Nuclear Analysis Package (SNAP) User's Manual v3.1.9, Bloomsburg (USA): Applied Programming Technology, 2021.

[19] D. J., «Overview of MELCOR Activities in NRI Rez,» in *European MELCOR User Group Meetting*, Villigen (CHE), 2008.

[20] G. F., «QUENCH-06 ASTEC Model,» KIT, Karlsruhe (DEU), 2008.

[21] INOFLEX, «Compensatori di dilatazione metallici,» INOFLEX, Milan (ITA), 2019.

[22] PROSAIC Steel and Alloys, «ASTM A240 Grade 321 Stainless Steel Plates and Sheets,» PROSAIC, 2021. [Online]. Available:

https://www.prosaicsteel.com/astm_a240_321_stainless_steel_plates_sheets.html. [Consultato il giorno 2021].

[23] G. Schanz, B. Adroguer e A. Volchek, «Advanced treatment of zircaloy cladding high-temperature oxidation in severe accident code calculations. Part I. Experimental database and basic modeling,» *Nuclear Engineering and Design,* pp. 75-84, 2003.

[24] V. Urbanich e T. Heidrich, «High-temperature oxidation of ZIrcaloy-2 and Zircaloy-4 in steam,» *Journal of Nuclear Material 75,* pp. 251-261, 1977.

[25] A. Volchek, Y. Zvonarev e G. Schanz, «Advanced treatment of zircaloy cladding high-temperature oxidation in severe accident code calculations. Part II. best-fitted parabolic correlations,» *Nuclear Engineering and Design,* pp. 85-96, 2003.

[26] W. Ambrosini, R. Bovalini e F. D'Auria, «Evaluation of accuracy of thermalhydraulic code,» *Energia Nucleare,* vol. 7, pp. 5-16, 1990.

[27] F. Mascari, B. Woods, K. Welter e F. D'Auria, «Validation of the TRACE code againt small modular integral reactor natural circulation phenomena,» NURETH-18, Portland (USA), 2019.

[28] A. Prosek, JSI FFTBM Add-In 2007 User's Manual, IJS-DP-9752, 2007.

[29] A. Prosek, M. Leskovar e B. Mavko, «Quantitative assessment with improved fast Fourier transform based method by signal mirroring,» *Nucl. Eng. Des.,* vol. 238, p. 2668–2677, 2008.

[30] A. Prosek e M. Leskovar, «Use of FFTBM by signal mirroring for sensitivity study,» *Ann. Nucl. Energy,* vol. 76, p. 253–262, 2015.

List of Figures

List of Tables

List of symbols

Variable	Description	SI unit
R	resistance	Ω
T	temperature	K
$Ø$	diameter	m
$\dot{m}$	mass flow rate	kg/s
MM	molar mass	g/mol
C	species concentration	vol-%
M	mass	kg
v	velocity	m/s
x	length	m
z	height	m
Co	Courant number	-
Co_{max}	Courant acoustic limit	-
t	time	s
ρ	density	kg/m^3
A	area	m^2
$\partial(.)$	partial derivative	-
$\nabla \cdot$	gradient	m^{-1}

E	total energy	J
Q	heat	J
H	enthalpy	H
q	linear power	W/m
h	specific enthalpy	J/kg
$\boldsymbol{\Gamma}$	volumetric mass source density	kg/(m^{3}s)
HTC	heat transfer coefficent	W/(m^{2}K)
k	thermal conductivity	W/(mK)
C_p	specific heat	J/(kgK)
i	CV index	-
j	FL index	-
ϕ	phase index	-
m	material index	-
$d\text{-}th$	donor CV	-
$\alpha_{j\phi}$	volume fraction of ϕ in j	-
F	open fraction in FL	-
σ	direction coefficent	-
$\widetilde{K}$	form loss coefficent	-
g	gravity acceleration	m/s^2

f	Fanning friction factor	-
s	segment in FL	-
D_s	diameter of s	m
L_s	length of s	,
Pe	Peclet number	-
Bi	Biot number	-
L_D	diffusion length	m
Θ	dimensionless temperature	-
δ_s	surface thickness	m
K	reaction rate	$kg/(m^2 s^{0.5})$
W	mass of oxidized zircaloy per unit surface	kg/m^2
δ	oxide thickness	m
r_0	β-Zr initial thickness	

List of acronyms

Acronym	Name
ACR	Advanced CANDU Reactor
ACV	Additional Control Volume
AOO	Anticipated Operational Occurence
ATWS	Anticipated Transient Without SCRAM
CANDU	Canada Deuterium Uranioed
CCF	Common Cause Failure
CF	Control Function
CPA	Coolant Passage Area
CVCS	Chemical and Volume Control System
CVH	Control Volume Hydrodynamics
DBA	Design Basis Accident
DEC	Design Extension Condition
DID	Defense in Depth
EBS	Engineering Barrier System
ECCS	Emergency Core Control System
EL	Elevation
FCI	Fuel Cladding Interaction
FFBTM	Fast Fourier Based Transform Method

FL	Plow Path
HS	Heat Structure
LOCA	Loss Of Coolant Accident
LWR	Light Water Reactore
MCCI	Molten Core Concrete Interaction
NO	Normal Operation
NPP	Nuclear Power Plant
PBR	Pebble Bed Reactor
PHWR	Pressurized Heavy Water Reactor
PIE	Postulated Initiating Event
PMR	Prismatic Core Modular Reactor
P&ID	Pressure and Instrumentation Diagram
RHR	Residual Heat Removal
RPV	Reactor Pressure Vessel
SA	Severe Accident
SBO	Station Blackout
TCV	Test Control Volume
TF	Tabular Function

Acknowledgments

I would like to thank Prof. Luzzi for making possible the thesis with ENEA Bologna.

I would like to thank Eng. Mascari, Eng. Bersano and Eng. Agnello of ENEA for the support and explanations they gave me during the last months. I will not forget the afternoons spent on some impossible energy balance..

I would like to thank Eng. Gabrielli of KIT for his kindness in deploying info and data, and hints as well.

To my father, my mother, and my family. I cannot express in words how grateful I am for everything they did. This achievement is dedicated to them.

To Pietro, Carola, Tommaso, Klaudia, Nicolò, Jacopo, Colla, Francesca, Giovanni, Giacomo, Davide, Margherita, Chiara. My dearest friends.

To Pietra and to all the people I know since I was a kid, to which I am deeply bound.

To CUS Pavia Rugby, my teammates. Thank you for teaching me what it means *Siamo Questi.*

To Marta, her warm support has gone far beyond the drawings and the advises.

To everyone who has been there even when the rain started to pour,

Thanks.